

ELECTRICAL CHARACTERIZATION IN HETEROJUNCTION DEVICES
OF SEMICONDUCTING IRON DISILICIDE/SILICON AND
NANOCRYSTALLINE DIAMOND/SILICON



RAWIWAN CHALEAWPONG

A THESIS SUBMITTED IN PARTIAL FULFILLMENT OF THE REQUIREMENT FOR THE
DEGREE OF DOCTOR OF PHILOSOPHY IN APPLIED PHYSICS
DEPARTMENT OF PHYSICS SCHOOL OF SCIENCE
KING MONGKUT'S INSTITUTE OF TECHNOLOGY LADKRABANG
2021

KMITL-2021-SC-D-030-053

This material is reserved for educational use only, not allowed for commercial use.

Forbidden to modify the content, and cite the document when use.



COPYRIGHT 2021

SCHOOL OF SCIENCE

KING MONGKUT'S INSTITUTE OF TECHNOLOGY LADKRABANG

Forbidden to modify the content, and cite the document when use.

School of Science
King Mongkut's Institute of Technology Ladkrabang
Thesis Certification

Thesis Title Electrical Characterization in Heterojunction Devices of Semiconducting Iron Disilicide/Silicon and Nanocrystalline Diamond/Silicon




Student Name Miss Rawiwan Chaleawpong

Student ID 61605015

Degree Doctor of Philosophy (Applied Physics)

Department Physics

Thesis Advisor Asst.Prof.Dr. Nathaporn Promros

Thesis Committee	Signatures
Dr. Mati Horprathum Chairperson and Examiner	
Assoc. Prof. Dr. Pattareeya Damrongsak Examiner	
Asst. Prof. Dr. Pisan Sukwisutet Examiner	
Dr. Pichanan Teesetsopon Examiner	
Asst. Prof. Dr. Nathaporn Promros Examiner	

Examination Date 9th December 2021 **Time** 09.00 - 12.00 a.m.

Place Online Exam

Approved by School of Science



(Assoc. Prof. Dr. Sutee Chutipaijit)

Dean

Date 24th December 2021

Thesis Title	Electrical Characterization in Heterojunction Devices of Semiconducting Iron Disilicide/Silicon and Nanocrystalline Diamond/Silicon
Student Name	Miss Rawiwan Chaleawpong
Student ID	61605015
Degree	Doctor of Philosophy (Applied Physics)
Department	Physics
Year	2021
Thesis Advisor	Asst. Prof. Dr. Nathaporn Promros

Abstract

This work introduces two new materials of orthorhombic iron disilicide (β -FeSi₂) and ultrananocrystalline diamond (UNCD) for near-infrared and ultraviolet (UV) photodiode applications, respectively. To realize the new photodiodes, the significant electrical parameters should be provided. First, the p-silicon (Si)/n- β -FeSi₂ devices were manufactured through per facing-targets sputtering, and their existing interface state and series resistance (R_s) were studied using the interface state density (N_{ss}) and R_s values at various frequencies. Next, the study of existing interface state and R_s for p-UNCD/n-Si devices created by pulsed laser deposition were provided using the N_{ss} and R_s information at different frequencies. After that, the variations of carrier transport processes and device photodetection at different temperatures for p-UNCD/n-Si devices produced through coaxial arc plasma deposition (CAPD) were investigated from the diode parameters and UV detectivity at different temperatures, respectively. Lastly, the predications of equivalent circuit model and relaxation phenomenon of p-UNCD/n-Si devices manufactured via CAPD were carried out based on the impedance information at different voltages.

Keywords : Detectivity, Diode parameters, Interface density, p-Si/n- β -FeSi₂, p-UNCD/n-Si, Series resistance

Acknowledgement

This research project was accomplished with sufficient quality because of the guidance and support provided by advisor and committees. I am extremely grateful to my advisor, Asst. Prof. Dr. Nathaporn Promros, for giving me technical advice and assistance in preparing my research project. The expertise in several study fields of my advisor leads to the valuable research questions, guidance, and methodology, which brings me to sharpen my concept and produce a higher level of my research work.

Subsequently, I would like to greatly appreciate all members of thesis committees, Dr. Mati Horprathum, Assoc. Prof. Dr. Pattareeya Damrongsak, Asst. Prof. Dr. Pisan Sukwisute and Dr. Pichanan Teesetsopon for devoting time to this thesis examination. Further, I would like to express my gratitude to the thesis committees for reviewing and commenting on this thesis document.

Also, I would like to acknowledge Prof. Dr. Tsuyoshi Yoshitake for giving me the opportunity for internship and experiment at Yoshitake's Laboratory. I would particularly like to be thankful for the assistance and comment for manuscript preparation.

Moreover, I would like to thank all laboratory members at King Mongkut's Institute of Technology Ladkrabang, and Kyushu University for all kind supports for operating the experiment. I am incredibly thankful to Mr. Peerasil Charoenyuenyaoa and Mr. Nattakorn Borwornpornmetee for assistance in the experiment and the manuscript preparation.

Additionally, I would like to thank my parents for their counsel and sympathetic ear. Finally, I could not have completed this dissertation without my tolerance and research practice.

Miss Rawiwan Chaleawpong

Table of contents

	Page
Abstract.....	i
Acknowledgements.....	ii
Table of contents.....	iii
List of tables.....	vi
List of figures.....	vii
Chapter 1 Introduction.....	1
1.1 Research background.....	1
1.2 Research purposes.....	2
1.3 Research scopes.....	2
1.4 Research schedule.....	3
1.5 Benefits of the research.....	3
Chapter 2 Theory and literature reviews.....	4
2.1 Characteristics of β -FeSi ₂ material.....	4
2.2 Characteristics of UNCD.....	8
2.2.1 Characteristics of UNCD coated by PLD.....	9
2.2.2 Properties of UNCD created by CAPD	11
2.3 FTS technique.....	12
2.4 PLD technique.....	14
2.5 CAPD technique.....	14
2.6 Semiconductor.....	16
2.6.1 p-Type semiconducting material.....	16
2.6.2 n-Type semiconducting material.....	17
2.7 Heterojunction.....	17
2.7.1 Principle for photodiodes.....	19
2.8 Thermionic emission theory.....	19
2.9 Norde function.....	21
2.10 Detectivity.....	22
2.11 Nicollian-Brews and Hill-Coleman approaches.....	22
2.12 Impedance spectroscopy and equivalent circuit model.....	23
2.13 XRD.....	27
2.14 SEM.....	27
2.15 Raman spectroscopy.....	28
2.16 Significant parameters.....	29
2.16.1 Dark current.....	29
2.16.2 Photocurrent.....	30

Table of contents (cont.)

	Page
2.16.3 Ideality factor.....	30
2.16.4 Barrier height.....	30
2.16.5 Interface state density.....	31
2.16.6 Series resistance	32
2.16.7 Parallel resistance.....	32
2.16.8 Constant phase element.....	32
2.16.9 Activation energy.....	32
2.17 Literature reviews.....	33
2.17.1 Related works for p-Si/n- β -FeSi ₂ devices built by FTS.	33
2.17.2 Related works for p-UNCD/n-Si devices formed by PLD.....	35
2.17.3 Related works for p-UNCD/n-Si devices built by CAPD.....	36
Chapter 3 Experimental details.....	38
3.1 Manufacture of p-Si/n- β -FeSi ₂ heterojunctions via FTS.....	38
3.1.1 Synthesis of β -FeSi ₂ layer.....	38
3.1.2 Electrode creation for p-Si/n- β -FeSi ₂ junctions built by FTS	40
3.2 Creation of p-UNCD/n-Si heterojunctions by PLD.....	41
3.2.1 Creation of p-UNCD layer.....	41
3.2.2 Electrode creation for p-UNCD/n-Si junctions built by PLD...	43
3.3 Construction of p-UNCD/n-Si heterojunctions by CAPD.....	44
3.3.1 Manufacture of p-UNCD layer.....	44
3.3.2 Electrode creation for p-UNCD/n-Si junctions built via CAPD	45
3.4 Film characterizations.....	46
3.4.1 Raman spectroscopy.....	46
3.4.2 XRD examination.....	47
3.4.3 FESEM investigation.....	47
3.5 Electrical measurements.....	48
3.5.1 Electrical measurements for p-Si/n- β -FeSi ₂ devices formed by FTS.....	51
3.5.2 Electrical examinations for p-UNCD/n-Si devices created by PLD.....	51
3.5.2 Electrical inspections for p-UNCD/n-Si devices fabricated by CAPD.....	51
3.6 Assessment of significant parameters.....	52

Table of contents (cont.)

	Page
Chapter 4 Results and discussion	53
4.1 Results of the p-Si/n- β -FeSi ₂ devices formed via FTS.....	53
4.1.1 Structural properties.....	53
4.1.2 Surface morphology and cross section.....	54
4.1.3 Dark and irradiated <i>J-V</i> profiles at room temperature.....	55
4.1.4 C-V and <i>G/ω-V</i> profiles as a function of frequency.....	56
4.1.5 Computation and study of <i>R_s</i> and <i>N_{ss}</i> characteristics.....	57
4.2 Results of the p-UNCD/n-Si devices constructed via PLD.....	61
4.2.1 Raman patterns.....	61
4.2.2 Surface and cross-sectional images.....	61
4.2.3 Dark and irradiated <i>J-V</i> profiles at room temperature.....	62
4.2.4 C-V and <i>G/ω-V</i> investigations under various frequencies.....	63
4.2.5 Estimation and investigation of <i>R_s</i> and <i>N_{ss}</i> profiles.....	63
4.3 Results of the p-UNCD/n-Si devices manufactured via CAPD.....	66
4.3.1 Raman spectra.....	66
4.3.2 Surface image and cross-sectional observation.....	66
4.3.3 Dark <i>J-V</i> profiles and diode parameters at different temperatures.....	67
4.3.4 Dark and irradiated <i>J-V</i> profiles at different temperatures.....	73
4.3.5 Dynamic resistance and detectivity at different temperatures	74
4.3.6 Study on <i>Z'-Z''</i> results and equivalent circuit model for the heterojunction behavior at different voltages.....	75
Chapter 5 Conclusion and suggestions	77
5.1 Conclusion.....	77
5.1.1 Heterojunction devices of p-Si/n- β -FeSi ₂ formed by FTS.....	77
5.1.2 Heterojunction devices of p-UNCD/n-Si created by PLD.....	77
5.1.2 Heterojunction devices of p-UNCD/n-Si produced via CAPD	77
5.2 Suggestions.....	78
References.....	79
Author biography.....	90

List of tables

Table	Page
1.1 Research procedures.....	3
3.1 Condition for depositing the β -FeSi ₂ layer.....	39
3.2 Conditions of Ohmic contact creation for p-Si/n- β -FeSi ₂ heterojunctions....	40
3.3 Condition for depositing the p-UNCD layer by PLD.....	42
3.4 Condition of electrode creation for p-UNCD/n-Si junctions formed by PLD...	43
3.5 Condition for construction of the p-UNCD films by CAPD.....	45
4.1 Parameters of the p-Si/n- β -FeSi ₂ devices defined using C-V and G/ ω -V data at different frequencies.....	60
4.2 Parameter values assessed from the C-V and G/ ω -V curves at different frequencies of the p-UNCD/n-Si diodes formed by PLD.....	65
4.3 Significant diode parameters at different temperatures for the p-UNCD/n-Si devices created via CAPD.....	72

List of figures

Figure	Page
2.1 Equilibrium phase diagram of Fe-Si alloy system.....	5
2.2 Schematic illustration of orthorhombic β -FeSi ₂ crystal structure.....	5
2.3 Top view of lattice matching for β -FeSi ₂ to Si(111) in (a) FeSi ₂ (110)/Si(111) and (b) FeSi ₂ (101)/Si(111) heteroepitaxial relationships	6
2.4 Band structure of β -FeSi ₂ compound for energies near the bandgap.....	7
2.5 (a) Optical absorption profiles of β -FeSi ₂ compared with that of Si and (b) relationship of $(E \times \alpha)^2$ and $(E \times \alpha)^{1/2}$ as a function of photon energy for epitaxial β -FeSi ₂ layer coated on Si(111) wafer.....	7
2.6 SAED profile of the UNCD/a-C films coated by PLD in H ₂ pressure.....	9
2.7 (a) Dark-field and (b) high-resolution TEM photographs of the UNCD/a-C films coated by PLD under H ₂ ambience.....	9
2.8 (a) Absorption coefficient spectrum and (b) plots of $(\alpha h\nu)^{1/2}$ and $(\alpha h\nu)^2$ with the photon energy of the UNCD/a-C:H films coated using PLD.....	10
2.9 XRD line for (a) UNCD/a-C:H films produced via CAPD with the inserted image of Debye-Scherrer rings	11
2.10 (a) Optical absorption profile and (b) relationship of $(\alpha h\nu)^{1/2}$ and $(\alpha h\nu)^2$ as a function of photon energy for UNCD/a-C:H films coated by CAPD.....	12
2.11 Sputtering process.....	12
2.12 (a) FTS diagram and (b) sputtering mechanism in FTS system.....	13
2.13 Schematic configuration of PLD setup.....	14
2.14 Demonstration of (a) coaxial arc plasma gun with creation of an arc plasma and (b) schematic diagram of CAPD apparatus.....	15
2.15 Atom structure of (a) Si and (b) Ge.....	16
2.16 (a) Structure of Si added with B element to create p-type semiconductor and (b) band diagram of p-type semiconductor.....	17
2.17 (a) Structure of Si added Sb element to produce n-type semiconductor and (b) band diagram of n-type semiconductor	17
2.18 Three types of heterojunctions based on the bandgap alignment comprising (a) straddling, (b) staggered gaps and (c) broken gaps.....	18
2.19 Band diagram of heterojunction (straddling) at thermal equilibrium.....	18
2.20 (a) Photodiode cross section and (b) photodiode p-n junction state.....	19
2.21 $Z'-Z''$ spectra with the related equivalent circuit model of (a) R_p and C in parallel connection, (b) shunt circuit of R_p and C serially connected with R_s (c) parallel association of R_p and CPE serially combined with R_s	26

List of figures (cont.)

Figure	Page
2.22 Bragg reflection by a set of parallel planes with interplanar distance.....	27
2.23 Interaction of electron beam with specimen and signals from sample.....	28
2.24 Raman scattering.....	29
2.25 Characteristic curve of I - V for p-n heterojunction diode.....	30
2.26 Diagram of interface states under (a) dark and (b) irradiation.....	31
2.27 Interface state existing at the interface for heterojunction diode.....	31
2.28 Band diagram demonstration of the p-Si/n- β -FeSi ₂ heterojunctions constructed employing FTS.....	33
2.29 Dark and irradiated I - V profiles at 300 K of the p-Si/n- β -FeSi ₂ photodiodes built by FTS. The inset unveils the dynamic resistance plot.....	34
2.30 NIR response profile of the built p-Si/n- β -FeSi ₂ device at 0 V and 300 K. The inserted image is the quantum efficiency and responsivity in negative voltages under the irradiation at 1.31 μ m and 6 mW	35
2.31 (a) Energy band diagram of the p-UNCD/n-Si junctions formed by PLD (b) configuration schematic of the hetero-interface.....	36
2.32 Dark and irradiated I - V profiles at room temperature for the p-UNCD/n-Si devices fabricated via PLD.....	36
2.33 Schematic illustration of the energy band diagram of p-UNCD/n-Si heterojunction devices manufactured through CAPD technique.....	37
2.34 Dark and irradiated I - V curves at room temperature for the p-UNCD/n-Si photodiodes created by CAPD.....	37
3.1 FTS apparatus for film creation.....	38
3.2 Schematic configuration of FTS apparatus.....	39
3.3 RFMS system to construct the electrodes.....	40
3.4 (a) Configuration and (b) photograph of the built p-Si/n- β -FeSi ₂ heterojunctions with electrodes.....	41
3.5 PLD system.....	41
3.6 Illustration of the schematic diagram of a PLD system.....	42
3.7 (a) Device diagram and (b) image of the p-UNCD/n-Si devices created by PLD with electrodes.....	43
3.8 Illustration for CAPD setup.....	44
3.9 Schematic configuration of CAPD system.....	45
3.10 (a) Device demonstration and (b) image of the p-UNCD/n-Si heterojunction devices created by CAPD with electrodes.....	46

This material is reserved for educational use only, not allowed for commercial use.

Forbidden to modify the content, and cite the document when use.

List of figures (cont.)

Figure	Page
3.11 Raman spectrometer.....	46
3.12 Rigaku RINT 2000/PC X-ray diffractometer.....	47
3.13 (a) Carl Zeiss Auriga FESEM and (b) Hitachi S-4700 SEM.....	48
3.14 Diagram of electrical examination setup.....	48
3.15 Photograph of electrical examination setup.....	49
3.16 Temperature controller.....	49
3.17 Interior of the cabinet.....	49
3.18 Setting the sample inside the chamber.....	49
3.19 Keithley 2400 Series Source Measure Unit Instrument.....	50
3.20 Agilent E4980A Precision LCR Meter.....	50
3.21 Setup of laser for NIR radiation.....	50
3.22 Setup of lamp for UV radiation.....	50
4.1 XRD trace in the 2θ - θ scan of β -FeSi ₂ films manufactured on the Si substrates. The inserted line exhibits the XRD line examined in a 2θ scan...	54
4.2 Pole figure characteristic of β -440/404 peak for epitaxial β -FeSi ₂ films.....	54
4.3 FESEM photographs of (a) top and (b) cross-section views for the β -FeSi ₂ film coated on Si substrate.....	55
4.4 Dark and irradiated J - V curves of the p-Si/n- β -FeSi ₂ devices inspected at room temperature. The inserted image exhibits the photocurrent deducted from the dark current.....	56
4.5 (a) C - V and (b) G/ω - V profiles under various frequencies of p-Si/n- β -FeSi ₂ devices manufactured by FTS.....	57
4.6 R_s - V profiles at different frequencies for the p-Si/n- β -FeSi ₂ junctions.....	58
4.7 R_s - f relationship at zero bias for p-Si/n- β -FeSi ₂ heterojunctions.....	58
4.8 N_{ss} - f curve at room temperature for p-Si/n- β -FeSi ₂ heterojunctions.....	60
4.9 Raman lines for undoped and B-doped UNCD/a-C:H films created by PLD...	61
4.10 (a) Morphological and (b) cross-sectional images of the B-doped UNCD/a-C:H layer produced on Si wafer by PLD.....	62
4.11 Dark and irradiated J - V profiles at room temperature for the p-UNCD/n-Si devices constructed by PLD.....	62
4.12 (a) C - V and (b) G/ω - V curves at different frequencies for the p-UNCD/n-Si devices manufactured via PLD.....	63
4.13 R_s - V plots for the p-UNCD/n-Si devices manufactured by PLD at different frequencies between 40 kHz and 2 MHz.....	64

List of figures (cont.)

Figure	Page
4.14 N_{ss} profile at various frequencies for p-UNCD/n-Si devices formed by PLD...	65
4.15 Raman lines of the pure and B-doped UNCD/a-C:H films coated by CAPD...	66
4.16 Captured FESEM images in (a) top and (b) cross-sectional views of the B-doped UNCD/a-C:H films coated via CAPD.....	67
4.17 Dark J - V curves tested under various temperatures for the p-UNCD/n-Si devices constructed through CAPD.....	68
4.18 Variance of n (black plot) and ϕ_b (blue plot) in the temperature range between 150 K and 300 K.....	69
4.19 Arrhenius plot of J_0 against $1000/T$ for the p-UNCD/n-Si devices manufactured by CAPD.....	70
4.20 $F(V)$ - V profiles at 300 K and 150 K for the p-UNCD/n-Si devices constructed via CAPD.....	71
4.21 R_s variance plotted with temperature for the p-UNCD/n-Si devices constructed through CAPD.....	72
4.22 Dark and irradiated J - V characteristics at (a) 300 K and (b) 150 K for the p-UNCD/n-Si devices produced by CAPD.....	73
4.23 Dynamic resistance profiles plotted with voltage at 300 K and 150 K.....	74
4.24 Characteristics of (a) $Z'-f$ and (b) $Z''-f$ at different voltages for the p-UNCD/n-Si devices constructed through CAPD	75
4.25 $Z''-Z'$ spectra at different voltages of the p-UNCD/n-Si devices built by CAPD. The inset is a circuit model related to heterojunction behavior.....	76

Chapter 1

Introduction

1.1 Research background

Semiconducting materials have been widely applied for optoelectronic devices [1,2]. Photodiode is a kind of optoelectronic device that has excellent attractive to use in diverse applications like photodetectors [3], optical telecommunications [3], solar cells [4], cameras [5], and gas sensors [6]. Photodiodes responding to near-infrared (NIR) radiation are widely used in night vision cameras and fiber-optic communications [5,7]. Indium gallium arsenide (InGaAs) and InAs are semiconductors widely used in NIR detection, but their toxicity is an obstacle [8-10]. Photodiodes sensitive to ultraviolet (UV) light are widely applied for optical communications, including ozone and flame detections [11]. Silicon carbide (SiC) and gallium nitride (GaN) are the materials used to detect UV light in the commercial industry [12]. However, potential industrial application of SiC is impeded by relatively high cost and low productivity [13,14] while GaN owns productivity lower than that of SiC [15].

To develop new photodiodes with high device performance, significant electrical characteristics such as the interface state density (N_{ss}), series resistance (R_s), diode parameters, detectivity, impedance (Z'' - Z') profiles of the devices should be studied. N_{ss} reveals the existing interface states in the hetero-interface areas, and R_s is the current-limiting factor [16-18]. Both N_{ss} and R_s can degrade the device performance [16-18]. Diode parameters such as the ideality factor (n) can express the carrier transport mechanism [19-21]. The value of detectivity can reveal the ability for photodetection of devices [22,23]. Further, the Z'' - Z' characteristics can apply to anticipate the equivalent circuit model with the relaxation process of photodiodes [24,25].

Semiconducting iron disilicide (β -FeSi₂) owns the direct and indirect bandgaps, conforming to the communication wavelengths from 1300 nm to 1550 nm [26,27]. It consists of non-toxic and abundant Fe and Si elements that are low-cost [28]. Its optical absorption coefficient is up to 10^5 cm^{-1} at 1.2 eV [26,27]. It is also easy to coat by several physical vapor depositions [29-31]. The production of epitaxial β -FeSi₂ films requires a low deposition rate [32]. For this reason, facing-targets sputtering (FTS) is one of the suitable methods for epitaxial β -FeSi₂ growth due to its low sputtering rate and high film quality with a small stoichiometric ratio from target and film [26].

Ultrananocrystalline diamond (UNCD) is a carbon-based material, which is plentiful, low cost, non-harmful, and easy for film formation [33]. It owns the optical gap conforming to UV range and high optical absorption coefficient over 10^5 cm^{-1} from

This material is reserved for educational use only, not allowed for commercial use.

Forbidden to modify the content, and cite the document when use.

3 eV to 6 eV due to many grain boundaries [34,35]. Its conductivity can be changed by adding the boron atoms to engender the p-type conduction [36,37]. To create the UNCD crystallites, a supersaturated condition for nucleation of diamond is required, which can be realized by highly energetic carbon ion and species arrived at a substrate in a high density [38]. Pulsed laser deposition (PLD) and coaxial arc plasma deposition (CAPD) are used to create the UNCD films since they can rapidly produce a supersaturated condition for nucleation of diamond [38,39].

In the present work, two new materials of β -FeSi₂ and UNCD were introduced to replace the former materials responding to NIR and UV, respectively. First, the interface state and R_s of the p-Si/n- β -FeSi₂ devices built by FTS and the p-UNCD/n-Si devices created by PLD will be originally studied using N_{ss} and R_s values at various frequencies for being the way to enhance the device performance. Next, the diode parameters and UV detectivity at different temperatures of p-UNCD/n-Si devices constructed via CAPD will be first extracted to clarify the difference of carrier transport processes and device photodetection under low temperatures, respectively. Lastly, the Z'' - Z' spectra of p-UNCD/n-Si devices manufactured via CAPD will be investigated under various voltages at room temperature to anticipate the equivalent circuit model with the relaxation process. Based on these electrical studies, the development of new photodiodes with high performance should achieve for usability in the optoelectronic industry in the future.

1.2 Research purposes

- 1) To extract the N_{ss} and R_s values at different frequencies of the p-Si/n- β -FeSi₂ junctions built by FTS and the n-Si/p-UNCD devices created via PLD.
- 2) To examine the UV detection and diode parameters at different temperatures for the p-UNCD/n-Si devices created through CAPD.
- 3) To study the Z'' - Z' profiles at diverse voltages for p-UNCD/n-Si devices built via CAPD.

1.3 Research scopes

- 1) The N_{ss} and R_s of the p-Si/n- β -FeSi₂ devices built by FTS were appraised by the capacitance-voltage (C - V) and conductance-voltage (G - V) profiles measured under various frequencies from 5 kHz to 1 MHz at room temperature in a bias range of 5 V to -5 V in the dark.
- 2) The N_{ss} and R_s of the p-UNCD/n-Si devices created by PLD were estimated using the C - V and G - V data examined in a frequency range from 40 kHz to 2 MHz in the dark at room temperature under applied voltages from 5 V to -5 V.

- 3) The diode parameters and UV detection of the p-UNCD/n-Si devices built by CAPD were evaluated using dark and irradiated current density-voltage (J - V) data compiled in a temperature range of 300 K - 150 K under applied voltages between 3 V and -3 V.
- 4) The Z' - Z'' characteristics of the p-UNCD/n-Si devices constructed via CAPD were studied at different voltages from 0 V to 0.5 V at room temperature in the dark with applied frequencies from 20 Hz to 2 MHz.

1.4 Research schedule

Table 1.1 Research procedures

Procedure	Academic year		
	2018	2019	2020
Study the research articles relating to the research topic			
Study the fabrication process for p-Si/n- β -FeSi ₂ junctions through FTS and p-UNCD/n-Si junctions via PLD and CAPD			
Collect the C - V and G - V data of the p-Si/n- β -FeSi ₂ devices created by FTS and the p-UNCD/n-Si devices constructed by PLD at different frequencies for the N_{ss} and R_s extractions			
Measure the dark and irradiated J - V data of the p-UNCD/n-Si devices built by CAPD at low temperatures to assess the diode parameters and the UV detectivity values			
Inspect the Z' - Z'' profiles of the p-UNCD/n-Si junctions created by CAPD under various voltages at room temperature			
Characterize the experimental outcomes and parameters			
Provide the essential data for the preparation of the thesis			

1.5 Benefits of the research

- 1) Reveal the N_{ss} and R_s data at several frequencies for the p-Si/n- β -FeSi₂ devices built by FTS and the p-UNCD/n-Si devices formed by PLD and apply these data for developing the device performance in the future.
- 2) Explore the diode parameters and UV detectivity values at different temperatures of the p-UNCD/n-Si devices constructed by CAPD to study the difference of carrier transport mechanism and UV photodetection performance of the built junctions.
- 3) Earn the Z' - Z'' characteristics under various voltages of the p-UNCD/n-Si devices produced by CAPD to clarify the relaxation process with an equivalent circuit model.

This material is reserved for educational use only, not allowed for commercial use.

Forbidden to modify the content, and cite the document when use.

Chapter 2

Theory and literature reviews

This chapter reveals the information regarding the principles and related research works. It begins with the delineations of the β -FeSi₂ and UNCD properties. Then the principles of film creation techniques such as FTS, PLD and CAPD are exposed. After that, the author expounds on the theory and the method for estimating the significant parameters. Also, the principle for investigating X-ray diffraction (XRD), Raman spectroscopy, and field emission scanning electron microscopy (FESEM) is provided. Finally, the last section presents the literature reviews relative to the heterojunction devices of p-Si/n- β -FeSi₂ and p-UNCD/n-Si.

2.1 Characteristics of β -FeSi₂ material [40-42]

The iron silicide (Fe-Si) compounds are one kind of transition metal silicide material, which takes a vital role in the light-responsive and light-emitting devices. The standard binary phase diagram for the Fe-Si system is exhibited in Figure 2.1 [40]. Based on the Fe-Si phase diagram, Fe-Si compounds contain suicide (Fe₃Si), xifengite (Fe₅Si₃), iron monosilicide (FeSi), and FeSi₂ with silicon-rich phase. Among the Fe-Si system, the iron-rich phase Fe₃Si with a body-centered cubic DO₃ structure and the mesophase Fe₅Si₃ composite with hexagonal structure manifest ferromagnetic behavior. The FeSi compound reveals a nonmagnetic metallic feature. Within an atomic percent silicon range of 65 and 70, the silicon-rich FeSi₂ in the equilibrium phase exhibits two stable allotropic forms consisting of tetragonal iron disilicide (α -FeSi₂) and β -FeSi₂ with orthorhombic structure. The α -FeSi₂ phase presents metallic features and is stable at high temperatures. The β -FeSi₂ phase is stable at a low-temperature range and exhibits the semiconducting behaviors due to the appearance of stoichiometric composition. The stable point of β -FeSi₂ phase is lower than the temperature of 937 °C. The β -FeSi₂ material has been favorable as a probable candidate for novel Si-based devices in optoelectronic applications such as photodiodes, solar cells and light-emitting diode due to the semiconducting behavior [26,27]. The minerals employed to manufacture the β -FeSi₂ composites include Fe and Si. Both Fe and Si are non-noxious minerals and have a consummate presence on the earth's crust [41].

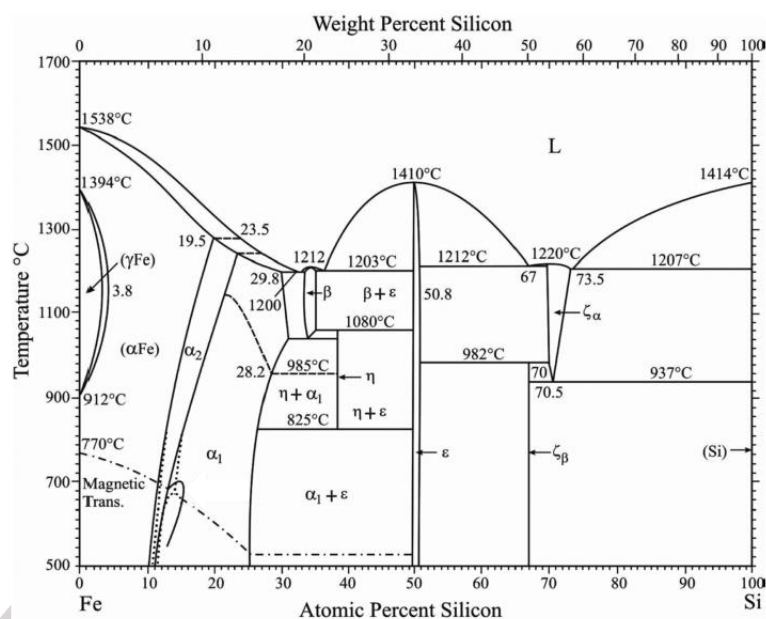


Figure 2.1 Equilibrium phase diagram of Fe-Si alloy system [40].

Figure 2.2 unveils the structure of orthorhombic β -FeSi₂ [43]. The lattice constants for *a*, *b*, and *c* of orthorhombic β -FeSi₂ are 9.863 Å, 7.791 Å, and 7.833 Å, respectively. The crystal structure of β -FeSi₂ is an orthorhombic system with the space group of *Cmca*. Each orthorhombic β -FeSi₂ crystal structure owns 48 atoms per unit cell in which can categorize as Fe of 16 atoms and Si of 32 atoms. Each unit cell owns two crystallographically inequivalent Fe sets and two inequivalent Si types. Each Fe site is occupied via 8 Fe atoms, and each Si type constitutes 16 atoms of Si.

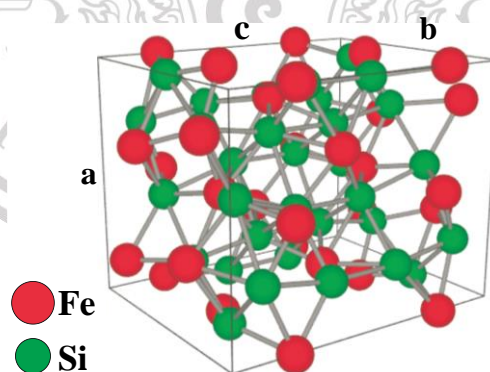


Figure 2.2 Schematic illustration of orthorhombic β -FeSi₂ crystal structure [43].

Although the dissimilarity in symmetry between orthorhombic β -FeSi₂ form and cubic Si structure with lattice parameter a of 5.5431 Å appears, the epitaxial construction of β -FeSi₂ layer onto the wafer substrate of Si(111) has been formerly attained via many approaches [29-31]. The values of lattice mismatch for the β -FeSi₂/Si interface are justified to be minimal around 2% to 5% [44].

Normally, the epitaxial β -FeSi₂ films on the Si(111) wafers create two sorts of heteroepitaxial relationships. The first relationship is FeSi₂(110)/Si(111) with FeSi₂ [001]||Si <110>, and the second kind is FeSi₂(101)/Si(111) with FeSi₂ [010]||Si<011>, which both kinds are exhibited in Figure 2.3 (a) and (b), respectively. Each heteroepitaxial relationships present three possible epitaxial variants. The symmetrical rotation with 120° of the atomic arrangement in Si(111) substrate surface brings about three epitaxial 120°-rotated variants while another one could be rotated with 180°.

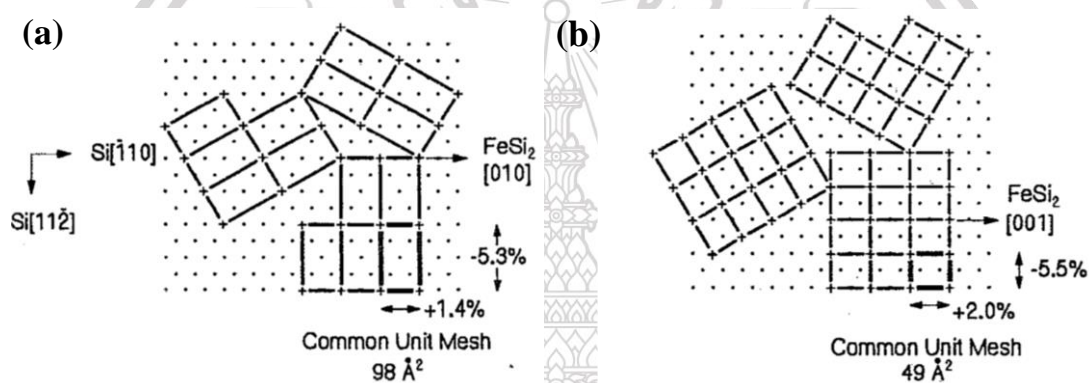


Figure 2.3 Top view of lattice matching for β -FeSi₂ to Si(111) in (a) FeSi₂(110)/Si(111) and (b) FeSi₂(101)/Si(111) heteroepitaxial relationships [44].

N. E. Christensen has exposed the electronic band structure of β -FeSi₂ estimated per a local-density approximation for energies close to the bandgap [45], as illustrated in Figure 2.4. The indirect bandgap acquired from local-density approximation is 0.80 eV. The direct bandgap obtained from the experiment is 0.85 eV. The gap nature of β -FeSi₂ presented in the band structure is indirect, although the direct bandgap is extremely close to the indirect one. According to an indirect bandgap, it can state that an absorption part should observe in a range of energy less than the transition energy of direct bandgap.

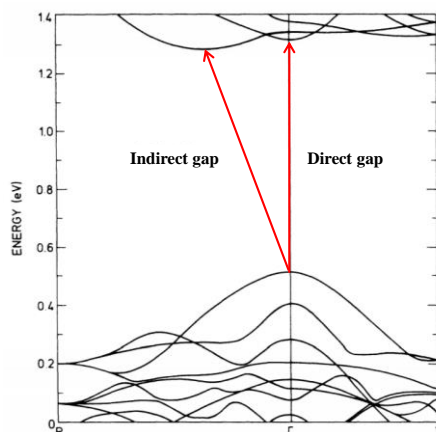


Figure 2.4 Band structure of β -FeSi₂ compound for energies near the bandgap [45].

T. Yoshitake et al. provided the optical absorption coefficient spectra of epitaxial β -FeSi₂ layer coated on Si(111) layer using FTS compared with that of Si wafer, as exposed in Figure 2.5 (a) [26]. The optical absorption coefficient value of β -FeSi₂ layer is over 10^5 cm^{-1} at photon energy of 1.2 eV. This value is higher than three orders of magnitude when compared to the optical absorption coefficient of Si. Also, the direct and indirect optical gaps were extracted using the optical absorption spectrum. As manifest in Figure 2.5 (b), the direct optical gap was defined to be 0.86 eV, and the determined indirect optical gap was 0.74 eV. These gaps fit into the transmission wavelengths of optical fiber communication systems about 1550 nm and 1300 nm. The wide usage of these transmission wavelengths in optical fiber transmission systems is due to small loss and dispersion attributes of Si-based optical fibers.

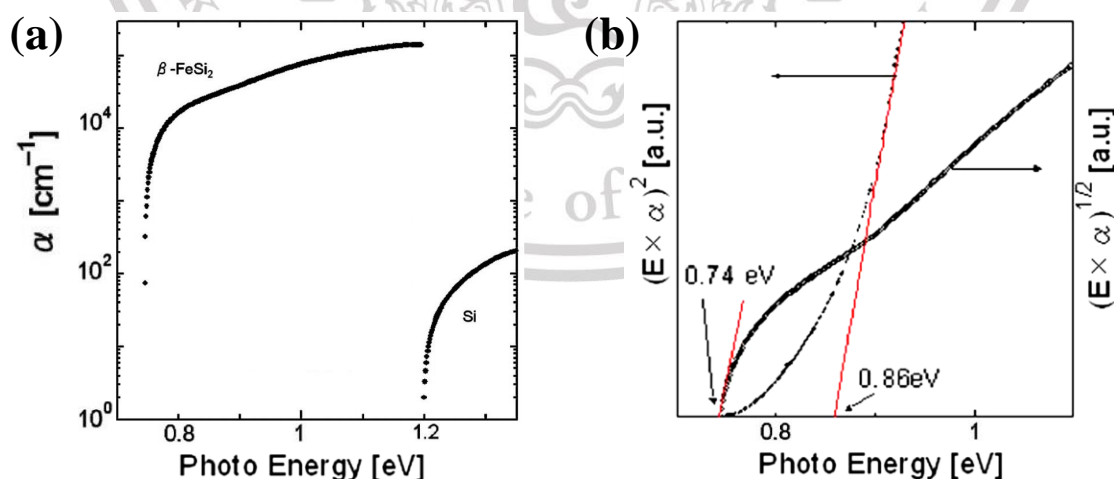


Figure 2.5 (a) Optical absorption profiles of β -FeSi₂ compared with that of Si and (b) relationship of $(E \times \alpha)^2$ and $(E \times \alpha)^{1/2}$ as a function of photon energy for epitaxial β -FeSi₂ layer coated on Si(111) wafer [26].

This material is reserved for educational use only, not allowed for commercial use.

Forbidden to modify the content, and cite the document when use.

2.2 Characteristics of UNCD [35-37,46]

Diamond films have excellent features such as excellent chemical stability, high thermal conductivity and excellent hardness. UNCD films are a particular patterned form of the diamond. They have lately caught great interest from many researchers due to their noticeable attributes. They contain a lot of UNCD grains with ultra-small grain sizes around 2 nm to 5 nm girdled about an amorphous carbon matrix. All UNCD grains are diamond owning a sp^3 character. They also consist of numerous grain boundaries that comprise a combination of amorphous carbon with the sp^2 character dominating, hydrocarbon, sp^2 and sp^3 . They can apply for high conductivity devices, micro-electromechanical systems, optoelectronic devices, field emission, and heterojunction.

The UNCD/a-C:H composite films own a unique structure, where many UNCD grains were girdled around an a-C:H matrix. The diameter size of UNCD grains has been quoted as smaller than 10 nm. Due to their remarkable and excellent features, they have appealed to profound scientific and technological attentiveness for competent and feasible usability in hard coatings, micro-electromechanical systems, and optoelectronic devices. Their surface feature is utterly smooth and pinhole-free, which is contrastive to polycrystalline diamond. The thermal stability of UNCD/a-C:H is preferable to the thermal stability value of untreated diamond-like carbon. UNCD/a-C:H films can be easily created onto foreign solid-state substrates when compared to the production of single- or polycrystalline diamond films. Based on the theoretical prediction, the specific feature occurring from many grain boundaries in the films might influence the electrical and optical characteristics. Their optical and electrical characteristics were considerably especial on account of the presence of abundant grain boundaries in the UNCD films. Grain boundary specifies the interfaces between UNCD grains, including the interfaces between UNCD grains and an a-C:H matrix. Former reports have uncovered that the UNCD/a-C:H films exposed high values of optical absorption coefficient over 10^5 cm^{-1} between the photon energies of 3 eV and 6 eV [35]. These high values were ascribable to grain boundaries. According to optical characteristics, UNCD/a-C:H material holds a plausible potential for application in photodetector devices. Although high-quality undoped UNCD possesses high electrical resistivity, the change of electrical conductivity can be attainable by doping. Previous report has unveiled that the conductivity of UNCD films has been mended by nitrogen incorporation into grain boundaries of UNCD films leading to n-type semiconductor behavior [46]. By boron incorporation, it can engender p-type conduction [36,37].

2.2.1 Characteristics of UNCD coated by PLD

Figure 2.6 discloses the selected area electron diffraction (SAED) profile of the UNCD/a-C films coated via PLD in hydrogen (H_2) pressure [35]. According to the SAED characteristic, the diffraction rings were observed. These diffraction rings were ascribable to diamond 111, 220, and 311, but these diffraction rings were not originated from graphite. The produced UNCD crystallites are non-oriented.

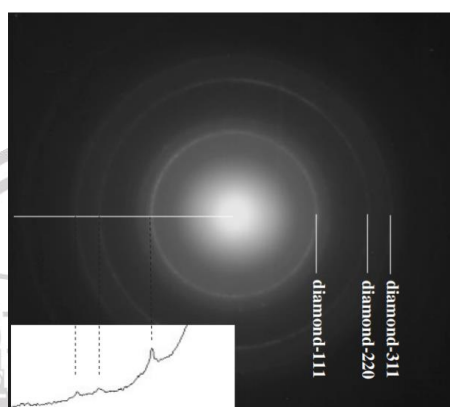


Figure 2.6 SAED profile of the UNCD/a-C films coated by PLD in H_2 pressure [35].

Figure 2.7 unveils the transmission electron microscopy (TEM) photographs of UNCD/a-C films built under H_2 pressure via PLD [35]. Figure 2.7 (a) reveals the TEM photograph under darkfield mode with the partial beam of the diamond-111 ring. The UNCD crystallite size and density distributions didn't rely on the depth of coated film. Figure 2.7 (b) discloses a typical high-resolution photograph of TEM. The periods of edge were around 0.21 nm, which originated from diamond-111. The diameter sizes of the UNCD crystallites were about 5 nm. Also, the matrix encompassing the UNCD crystallites seemed to be amorphous since the brightness and contrast of the image didn't rely on the variance in the tilt angle of the incident electron beam. Thus, the coated films contained the UNCD crystallites and the a-C matrix.

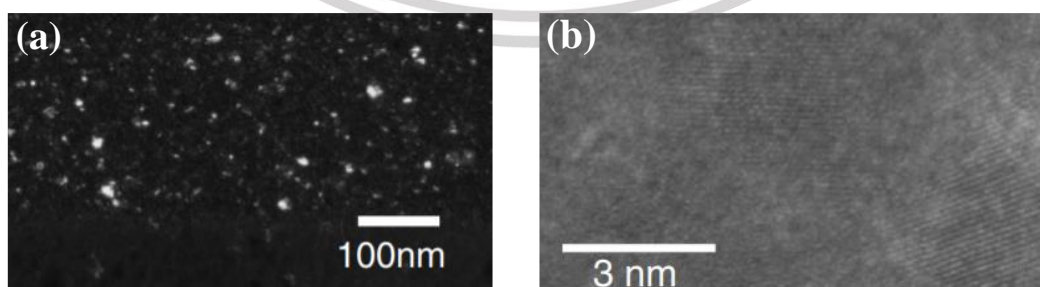


Figure 2.7 (a) Dark-field and (b) high-resolution TEM photographs of the UNCD/a-C films coated by PLD under H_2 ambience [35].

This material is reserved for educational use only, not allowed for commercial use.

Forbidden to modify the content, and cite the document when use.

T. Yoshitake et al. exposed the optical characteristics of UNCD/a-C:H films created via PLD [35]. Figure 2.8 (a) manifests the plot of optical absorption coefficient versus photon energy for the UNCD/a-C films prepared in H₂ ambience. The optical absorption coefficient trace was evaluated by the usage of the transmittance and reflectance characteristics. As indicated in Figure 2.8 (a), the absorption coefficient values were considerably high about 10⁶ cm⁻¹ in a range of photon energies between 3 eV to 6 eV. The large optical absorption coefficient values might originate in the grain boundaries. This value was superior to that of diamond over three orders of magnitude. Figure 2.8 (b) presents the $(\alpha h\nu)^{1/2}$ and $(\alpha h\nu)^2$ traces as a function of photon energy for the UNCD/a-C films coated utilizing PLD in H₂ pressure. The assessed indirect and direct bandgaps were 1.0 eV and 2.2 eV, respectively. The a-C matrix containing the mixed bonds of sp² and sp³ has an indirect optical bandgap between 0 eV and 5 eV relying on the proportion of sp² and sp³. The obtained indirect bandgap of 1.0 eV should stem from the a-C matrix in the film. The absorption at photon energy over 2.2 eV is due to direct absorption, which engenders a considerably high optical absorption coefficient for the UNCD/a-C films. This is specific to the UNCD/a-C composite films and the UNCD grain boundaries. The optical bandgap assessed from the $(\alpha h\nu)^{1/2}-h\nu$ profile was about 5.65 eV, which was slightly more than that of the diamond. Further, it has been presumed that the dangling bond termination by H₂ impinged on the occurrence of the electric states.

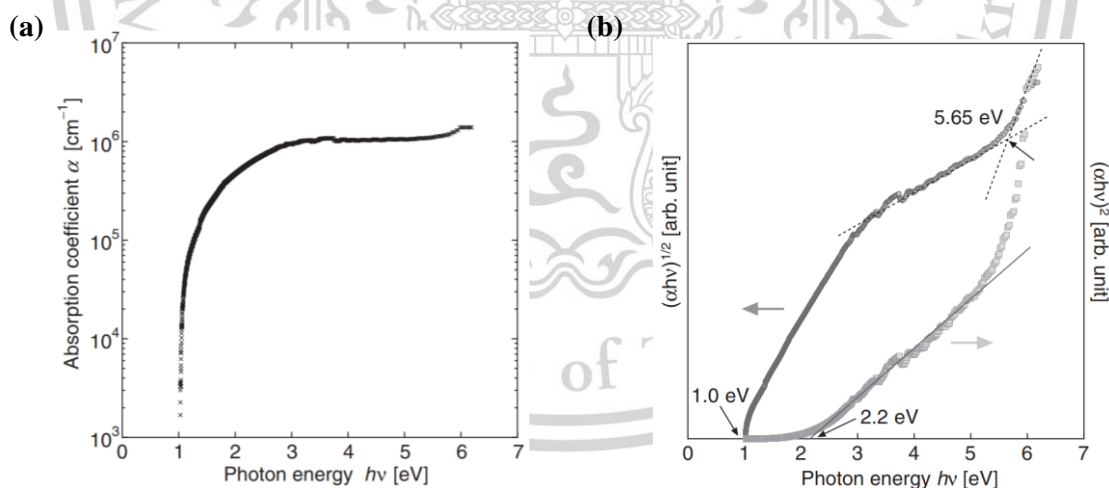


Figure 2.8 (a) Absorption coefficient spectrum and (b) plots of $(\alpha h\nu)^{1/2}$ and $(\alpha h\nu)^2$ with the photon energy of the UNCD/a-C:H films coated using PLD [35].

2.2.2 Properties of UNCD created by CAPD

T. Yoshitake et al. have successfully manufactured the UNCD/a-C:H films via CAPD [47]. Figure 2.9 exhibits XRD trace of UNCD/a-C:H films manufactured via CAPD. The XRD determination was managed using the Debye-Scherrer ring in the inserted graphic acquired from the imaging plate. Two observed diffraction rings were attributable to diamond-111 and diamond-220. These revealed a considerably wide peak indicating a very small crystallite size of UNCD. Based on Scherrer's equation, the diameter of UNCD crystallites was appraised to be 2 nm.

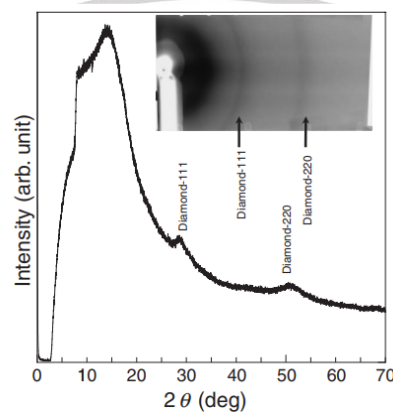


Figure 2.9 XRD line for (a) UNCD/a-C:H films produced via CAPD with the inserted image of Debye-Scherrer rings [47].

Figure 2.10 (a) exhibits the optical absorption profile of UNCD/a-C:H films produced via CAPD evaluated from the transmittance and reflectance data. The absorption coefficient value was found to be around $4 \times 10^5 \text{ cm}^{-1}$ in a photon energy range between 3.5 eV and 5 eV. This absorption coefficient was higher than that of diamond with two orders of magnitude. Figure 2.10 (b) exhibits the profiles of $(ah\nu)^{1/2}$ and $(ah\nu)^2$ plotted with photon energy for the UNCD/a-C:H films coated CAPD. Based on the $(ah\nu)^{1/2}-h\nu$ trace, the indirect bandgap was appraised to be 1.7 eV. The direct bandgap appraised through $(ah\nu)^2-h\nu$ curve was observed to be 2.9 eV. The a-C:H containing mixed bonds of sp^2 and sp^3 possessed bandgaps in a photon energy range of 0 – 3.0 eV, which these values relied on the portion of sp^3 to sp^2 bond. The indirect bandgap of 1.7 eV might originate in the a-C:H matrix in the produced films. The direct bandgap of 2.9 eV was specific attribute of the UNCD/a-C:H film. The absorption of the coated films at photon energies over 2.9 eV engenders a considerably high optical absorption coefficient. The high absorption values were presumed that occurred from the grain boundaries among UNCD crystallites due to the specific attribute of the UNCD/a-C:H films. Based on theory, it has been anticipated that the grain boundaries of UNCD crystallites created states in the bandgap of the diamond.

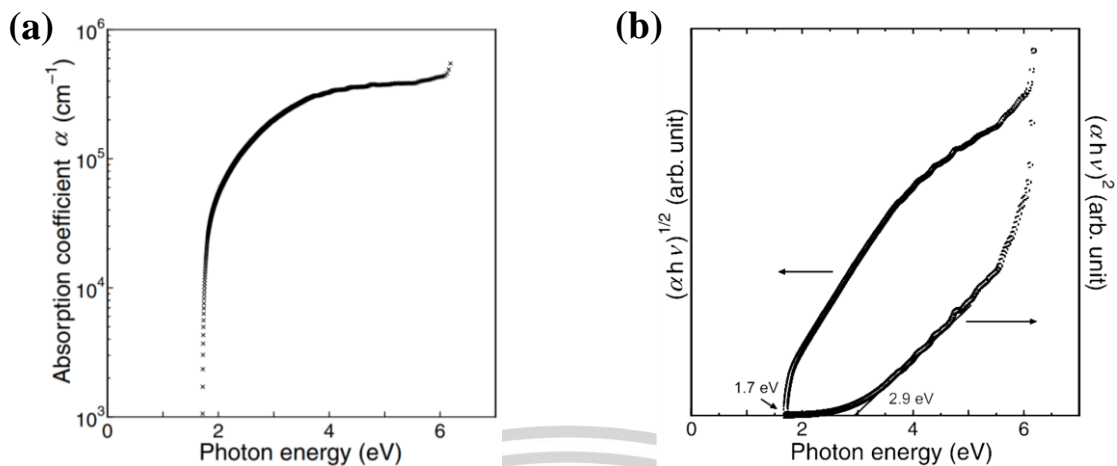


Figure 2.10 (a) Optical absorption profile and (b) relationship of $(\alpha h\nu)^{1/2}$ and $(\alpha h\nu)^2$ as a function of photon energy for UNCD/a-C:H films coated by CAPD [47].

2.3 FTS technique [48,49]

Sputtering is broadly employed for thin film deposition. Figure 2.11 illustrates the sputtering system inside a vacuum chamber. Sputtering relies on the created plasma after the collision of working gas and electron particles with high energies. The plasma can be confined via a magnetic field from a permanent magnet, which allows an intense sputtering discharge at low neutral gas densities. Sputtering phenomenon is created via a collision between incident bombarded particles such as accelerated gas ions and targets. The bombardment of particles holding energy over surface binding energy produces the release of atoms or molecules from a target surface. Then, the released particles arrive at the substrate surface, leading to a solid thin film.

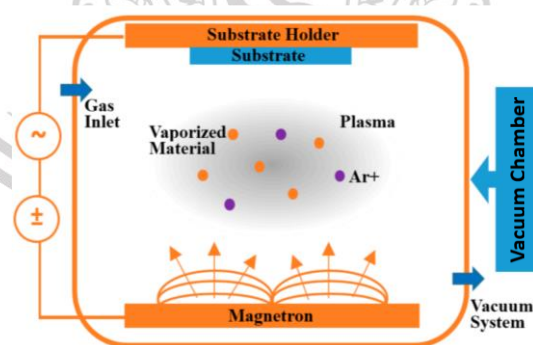


Figure 2.11 Sputtering process [48].

In traditional magnetron sputtering, the location of target and substrate is directly opposite and close. This substrate location is near the plasma area, which conduces to the bombardment of substrate with several high energetic particles such as accelerated gas ions and targets. This material is reserved for educational use only, not allowed for commercial use.

Forbidden to modify the content, and cite the document when use.

as secondary electrons, neutral argon atoms and negative ions. The bombardment by highly energetic particles leads to crystallographic deteriorations of the created films, defects at the grain boundaries, and thermal damage on the substrate surface.

Figure 2.12 (a) discloses the illustration of FTS system, which a couple of targets with identical size is positioned in opposite direction. The substrate site is perpendicular to the targets. The permanent magnetic arrangements are separately positioned with a designated length to provide a magnetic field expanding from one target to the other. A space between the target disks having a magnetic field expansion is called a discharge space. The magnetic field flux uniformly encloses the discharge space to confine the plasma. The film layer was formed onto a substrate, where is beside the discharge space in vacuum. The targets act as a cathode while the ground shields of the vacuum chamber behave as an anode. Both cathode and anode were connected to DC power supply, which is applied as a sputtering power. Sputtering gas injection into the vacuum chamber is confined via a gas regulator. The inert gas is normally applied as the sputtering gas due to non-wanted reactions with the target material or non-combination with any process gases. Especially, the inert gas creates superior sputtering and film production rates due to their high molecular weight. The plasma influences the sputtering of the targets, as unveiled in Figure 2.12 (b).

In collation with common sputtering, the electrons and ions striking on the substrate are abated. Further, thermal radiation from targets to substrate is minimal, engendering low increase in substrate temperatures. Thus, the films can create at low temperature. This technique provided the superior density of plasma and the few rises in substrate temperature in addition to less damageable effect on film. Also, the kinetic energy of the atoms and molecules colliding on the substrate surface is often several electron volts, which is greater than in other approaches.

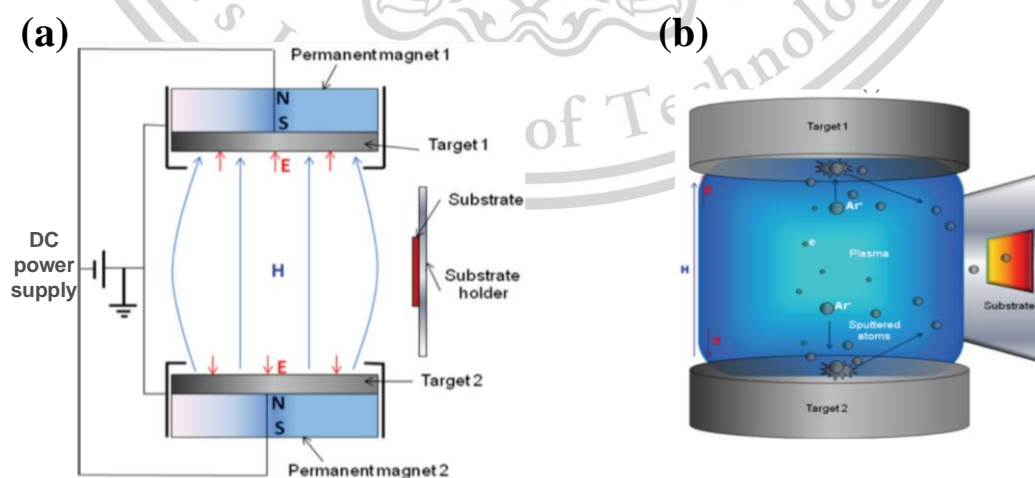


Figure 2.12 (a) FTS diagram and (b) sputtering mechanism in FTS system [49].

This material is reserved for educational use only, not allowed for commercial use.

Forbidden to modify the content, and cite the document when use.

2.4 PLD technique [39,50]

PLD is employed to manufacture a thin film in a vacuum system. Figure 2.13 reveals the schematic illustration of PLD system. For PLD technique, a high-power pulsed laser such as a KrF excimer laser is irradiated through a quartz window, and a high-power pulsed laser beam is focused onto a material target. A quartz lens is utilized to raise the energy density of the laser power on the target source. With an adequate high energy density of laser, a small number of the material is vaporized via each laser pulse generating a plasma plume. The ablation plume comprises the excited atoms, diatoms, ions, and other species. The vaporized material is driven out from the target in a highly forward-directed plume and compiled on substrate surfaces to create thin films. By PLD approach, a supersaturated condition with highly energetic ions and high density can be realized, leading to the formation of nanocrystallites.

PLD is broadly recognized as superior film manufacturing technique. This approach possesses the following merits: (i) stoichiometric transfer of material from the target; (ii) crystallinity improvement on account of the greatly energetic species; (iii) clean film coating owing to the absence of atmospheric gas; (iv) easy film synthesis, and (v) simplicity and flexibility in engineering design.

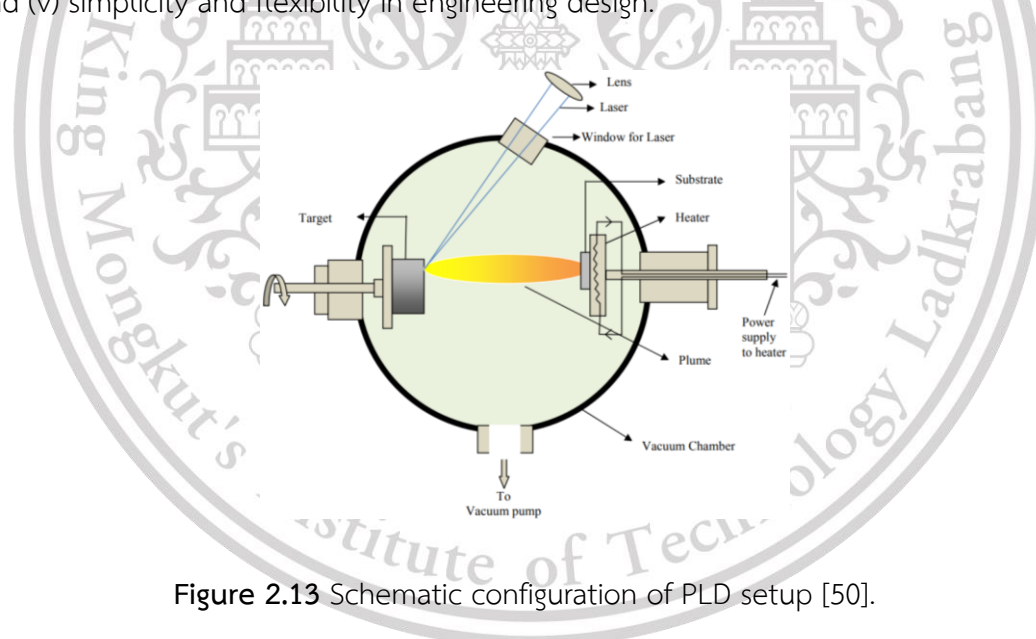


Figure 2.13 Schematic configuration of PLD setup [50].

2.5 CAPD technique [38,51]

CAPD is a dry process for coating nanoparticles on substrates. The CAPD approach is easy to create nanometer-sized particles on several substrate types. Figure 2.14 (a) reveals an illustration of a coaxial arc plasma gun with creating an arc plasma. As unveiled in Figure 2.14 (a), a target rod connected to a DC supply is served as the cathode while a metal cylinder connected to the ground is an anode. A trigger electrode is combined with a pulsed power supply. Furthermore, a capacitor for charge

This material is reserved for educational use only, not allowed for commercial use.

Forbidden to modify the content, and cite the document when use.

and discharge is connected between the cathode and the ground. Figure 2.14 (b) exposes a schematic representation of CAPD apparatus, in which the coaxial arc plasma gun was pointed at quartz facing plate. During the film synthesis, the chamber was evacuated using a combination of a rotary vane pump and a turbomolecular pump. To produce the plasma, CAPD system was applied with high voltage and capacitor capacitance. Consequently, the trigger electrode will be biased with a high voltage pulse. Thereby, a breakdown between the trigger electrode and cathode has been triggered. This breakdown ignites pulsed arc discharges on the surface of target rod and also induces a high energy density. In consequence, the cathodic target surface is instantly vaporized and ionized. The highly energetic ions formed from the target rod were deposited on the substrate to produce various thin films and nanoparticles.

In comparison with traditional cathodic arc discharge, the coaxial arc plasma gun holds the following remarkable attributes. An anodic cylinder can bunch ions ejected from a cathodic graphite rod located inside the cylinder. According to its structure, a supersaturated condition with highly energetic ions can be realized, which engenders the formation of nanocrystallites.

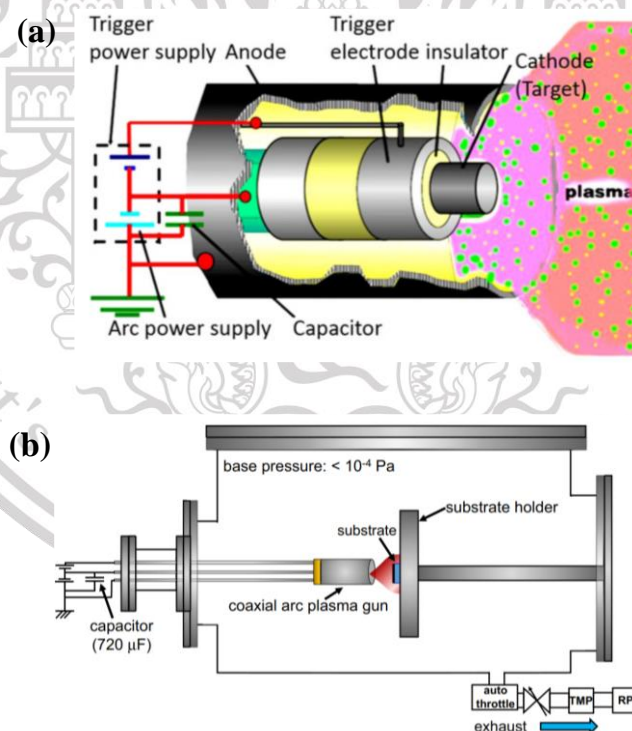


Figure 2.14 Demonstration of (a) coaxial arc plasma gun with creation of an arc plasma [51] and (b) schematic diagram of CAPD apparatus [38].

2.6 Semiconductor [52]

A semiconductor is a material that holds an electrical conductivity between a conductor and an insulator, which depends on the surrounding temperature, the concentration of doping atom or the incident light. The semiconductor is proper for application in electronic and optoelectronic devices such as solar cells, p-n diodes, including transistors. The semiconductor can be separated as intrinsic semiconductors and extrinsic semiconductors. An intrinsic semiconductor is semiconductor material without doping, which the carrier population of holes in the valence band is equivalent to the electron populations in the conduction band such as Si and germanium (Ge). The structures of an atom of Si and Ge are depicted in Figure 2.15 (a) and (b), respectively. Following its feature, the electric charge of the intrinsic semiconductor atom is unprejudiced. On the other hand, the extrinsic semiconductor is semiconductor material, which is comprised of elements more than two types. Types of extrinsic semiconductors can be divided into p-type and n-type semiconducting materials.

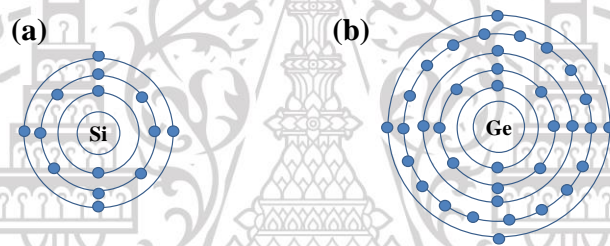


Figure 2.15 Atom structure of (a) Si and (b) Ge.

2.6.1 p-Type semiconducting material

A p-type material is a semiconductor that the atom in the lattice of semiconductor is supplanted via an element with three valence electrons and influence the change of the electron-hole equilibrium. The elements that have three valence electrons such as boron (B) and aluminum (Al). Replacement of element with three valence electrons in the semiconductor lattice leads to one excess hole, as indicated in Figure 2.16 (a). The excess holes are called the acceptor impurities because there will take the free electrons. The semiconductor of p-type possesses a larger number of the concentration of hole, which contributes to the positive charge. Besides, p-type semiconducting material has the Fermi level less than the Fermi level of intrinsic close to nearly the valence band, as demonstrated in Figure 2.16 (b).

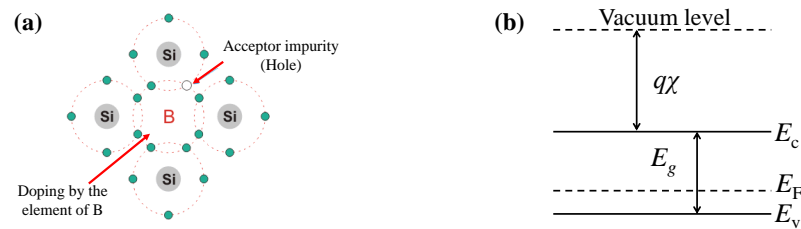


Figure 2.16 (a) Structure of Si added with B element to create p-type semiconductor and (b) band diagram of p-type semiconductor [52].

2.6.2 n-Type semiconducting material

In n-type semiconducting material, the semiconductor lattice of atom is substituted by an element with five valence electrons, such as nitrogen (N) and antimony (Sb). Substitution of the lattice by five valence electrons while the lattice can only catch four electrons, contributes to one excess electron, as shown in Figure 2.17 (a). The excess electron will donate an electron when there is driven by high energy. It is called as donor impurity. n-Type semiconductor has a larger electron concentration, which conduces to a negative charge. It has higher Fermi level than purity semiconductor close to the conduction band, as depicted in Figure 2.17 (b).



Figure 2.17 (a) Structure of Si added Sb element to produce n-type semiconductor and (b) band diagram of n-type semiconductor [52].

2.7 Heterojunction [52,53]

A heterojunction is an interface formed between two semiconductors of different energy bandgaps and electron affinities while the lattice constants should be similar. The different structures of two semiconducting materials conduce to the formation of an electric field around the junction. The band diagram of energy bandgaps for heterojunction diode is discontinued, and band bending is not smooth compared to those of homojunction. These are due to the difference in electron affinities, work functions, etc. These cause interface states or band discontinuities that form the recombination centers. The heterostructure diodes can be divided into three types, as demonstrated in Figure 2.18.

This material is reserved for educational use only, not allowed for commercial use.

Forbidden to modify the content, and cite the document when use.

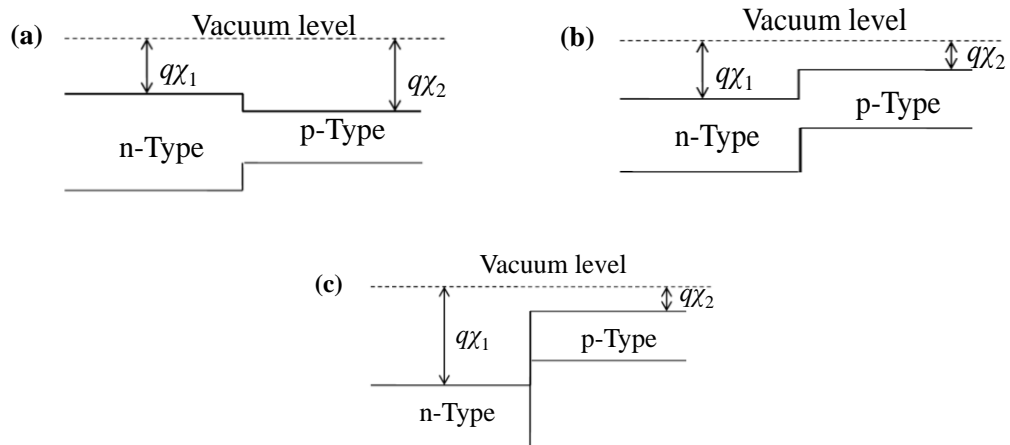


Figure 2.18 Three types of heterojunctions based on the bandgap alignment comprising (a) straddling, (b) staggered gaps and (c) broken gaps [53].

The transport models of heterojunction are developed from that of homojunction. Figure 2.19 exhibits a spike in the band edges arising from the different bandgaps ($E_{g1,2}$), electron affinities ($\chi_{1,2}$) and work function ($\phi_{1,2}$) of two semiconductors. The conduction and valence bands are discontinued. The band offset of conduction band based on Anderson's rule can be assessed by the given equation:

$$\Delta E_c = q\chi_2 - q\chi_1 \quad (2.1)$$

Also, the band offset of valance band can be computed by the given relation:

$$\Delta E_v = (E_{g1} - E_{g2}) - \Delta E_c = \Delta E_g - \Delta E_c \quad (2.2)$$

Band offsets of heterojunction create an extra barrier in junction, which raises the recombination of photocarriers. To minimize the band offset in heterojunction, ΔE_c should be minimized by choosing closer electron affinity and bandgap.

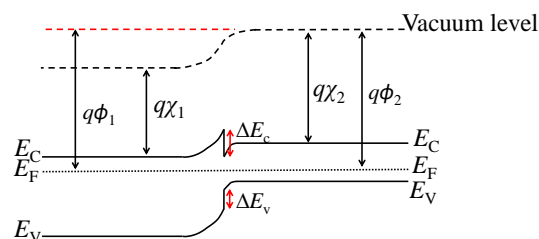


Figure 2.19 Band diagram of heterojunction (straddling) at thermal equilibrium [53].
This material is reserved for educational use only, not allowed for commercial use.

2.7.1 Principle for photodiodes [53,54]

A photodiode is a semiconductor light detector that generates a voltage or current when light falls on the junction. The photodetector is the device composed of p-n junction, which can change the photon energy into electrical current. The photodetector can be operated in negative bias range. Figure 2.20 demonstrates the characteristic of p-n junction photodiode excited with the photon energy. The sufficient energy of photon over the energy bandgap impinges on the semiconductor material contributing to the production of electron-hole pairs. The hole from the n-semiconductor material will be pushed by the electric field towards the p-semiconductor, and the electron from p-semiconductor side will be pushed by the same electric field value to n-semiconductor. This result reveals the increase of drift electric current.

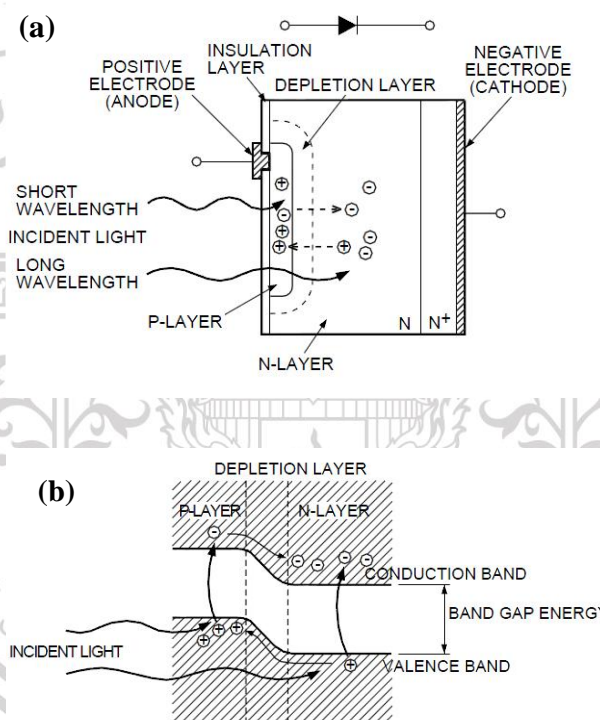


Figure 2.20 (a) Photodiode cross section and (b) photodiode p-n junction state [54].

2.8 Thermionic emission theory

Thermionic emission (TE) is the emission of electrons due to temperature. The electrons in the valence band are responsible for conducting the electric current. If the temperature is risen, the electrons in the valence band will be driven to a higher energy band. The current flow in the intermediate range without the consideration of R_s and shunt resistance can be expressed via the following equation [53,55,56]:

This material is reserved for educational use only, not allowed for commercial use.

Forbidden to modify the content, and cite the document when use.

$$I = I_0 \left(\exp \left(\frac{qV}{nkT} \right) - 1 \right) \quad (2.3)$$

where, I , I_0 , q , V , n , k , and T are the current, saturation current, charge of an electron, voltage across a diode, Boltzmann's constant and temperature, respectively.

The current density (J) can be written as follows:

$$J = J_0 \left(\exp \left(\frac{qV}{nkT} \right) - 1 \right) \quad (2.4)$$

where J and J_0 are the current density and saturation current density, respectively.

When the forward bias is over $3kT/q$, the -1 term can be ignored due to the term of $J \gg J_0$. Therefore, Eq. 2.4 can be written as follows:

$$\ln(J) = \ln(J_0) + \frac{qV}{nkT} \quad (2.5)$$

Therefore, the n value can be evaluated through the slope of the linear part of $\ln J$ - V characteristic in the initial of forward bias according to the following equation:

$$n = \left(\frac{q}{kT} \right) \left(\frac{dV}{d(\ln J)} \right) = \left(\frac{q}{kT} \right) \left(\frac{1}{\text{slope}} \right) \quad (2.6)$$

The J_0 value can extract from the intercept of the straight line of $\ln J$ - V plot at 0 V. J_0 is used for estimation of the barrier height (ϕ_b) by the following relation [55,57]:

$$J_0 = A^* T^2 \exp \left(\frac{-q\phi_b}{kT} \right) \quad (2.7)$$

where A^* and ϕ_b are Richardson's constant and the value of barrier height, respectively.

E_a value can be estimated by the following relation [17]:

$$J_0 \propto \exp \left(\frac{\Delta E_a}{kT} \right) \quad (2.8)$$

2.9 Norde function [58,59]

Based on the equation of ideal Schottky diode, if the existence of series resistance to diode displays in the base material, the linear line from plotting of $\ln I-V$ will be governed by the bias voltage in a range of $kT/q \ll V \ll IR$. If the series resistance is high, the range of bias voltage for giving a reliable value of I_0 will be very minute. It confines us for selecting the range of bias voltage at the minimal value of voltage. This results in that the recombination mechanism in the heterostructure diode should be a vital part of the entire current, leading to the value of I_0 value low authentic. For consideration in the case of a diode with a series resistance, the problem with a series resistance was eluded by the usage of relationship developed by Norde and others as indicated in the following equation [58,59]:

$$F(V) = \frac{V}{\gamma} - \left(\frac{kT}{q} \right) \ln \left(\frac{J}{T^2 A^*} \right) \quad (2.9)$$

where V , k , T , q , J , A^* and γ are the bias voltage, Boltzmann's constant, temperature, charge of electron, current density, Richardson's constant and first integer higher than the value of n , respectively. In this case, the n value was acquired from TE theory.

The ϕ_b and R_s values can be estimated through the minimum point of the $F(V)$ - V plot. The equation for calculating the value of ϕ_b is expressed as follows [58,59]:

$$\phi_b = F(V_0) + \frac{V_0}{\gamma} - \frac{kT}{q} \quad (2.10)$$

where $F(V_0)$ conveys the minimum point of $F(V)$ and V_0 specifies the voltage that corresponded to the value of $F(V)$ at the minimum point. The formula for the estimation of R_s is explained as follows [58,59]:

$$R_s = \frac{kT}{qAJ_{min}} (\gamma - n) \quad (2.11)$$

where J_{min} is the current density, which corresponded to the minimum point of $F(V)$.

2.10 Detectivity [60]

The photo detectivity is specified as the inverse of the noise-equivalent power. The larger detectivities are proper for detecting a small signal. In the normal case, the noise performance of the heterojunction devices can be specified using the Johnson noise function that will take place in low background radiation circumstance. The Johnson noise limited detectivity (D^*) value for the heterojunction devices at the zero bias can elucidate based on the following relation [60]:

$$D^* = R_\lambda \left(\frac{R_0 A}{4kT} \right)^{1/2} \quad (2.12)$$

where R_λ and R_0 convey the photocurrent responsivity and the dynamic resistance at the zero bias, respectively. Further, A presents the device area, k demonstrates Boltzmann's constant, and T means the operating temperature in degrees Kelvin.

Dynamic resistance refers to the change in current in response to a change in voltage. Dynamic resistance has been determined from the dark current-voltage (I - V) characteristic. For the determination, it is often assumed that the R_s value is minimal, and the shunt resistance is very large.

2.11 Nicollian-Brews and Hill-Coleman approaches

The admittance (Y_{ma}) in terms of measured capacitance (C_{ma}) and conductance (G_{ma}) can be specified through the following relation [61]:

$$Y_{ma} = j\omega C_{ma} + G_{ma} \quad (2.13)$$

Here R_s presents the real part of the impedance ($Z_{ma} = 1/Y_{ma}$). In this case, the R_s value can be extracted using the C_{ma} and G_{ma} values in strong accumulation at high frequencies [61,62].

The value of R_s parameter affects the heterojunction performance. For this reason, the R_s value needs to be kept as low as possible. The Nicollian-Brews approach is a suitable method for appraisalment of the R_s value, which can be expressed utilizing the following equation [62,63]:

$$R_s = \frac{G_{ma}}{(C_{ma}\omega)^2 + (G_{ma})^2} \quad (2.14)$$

where G_{ma} and C_{ma} are the conductance and capacitance values acquired in the strong accumulation region, respectively. ω denotes the angular frequency,

This material is reserved for educational use only, not allowed for commercial use.

Forbidden to modify the content, and cite the document when use.

The capacitance value of the insulator layer (C_{ox}) is specified via the employment of the relation indicated below:

$$C_{ma} = \frac{C_{ox}}{1 + \omega^2 R_s^2 C_{ox}^2} \quad (2.15)$$

The appraisalment of C_{ox} value can be manipulated using the C - V - f and G/ω - V - f information in the strong accumulation regime via the following formula:

$$C_{ox} = \left(\frac{(G_{ma})^2}{(C_{ma} \omega)^2} + 1 \right) C_{ma} \quad (2.16)$$

The N_{ss} appearance in the heterojunction devices was the chief reason for the degeneration of performance in the device. A mathematical approach presented by Hill-Coleman can be applied to appraise the N_{ss} value. Through Hill-Coleman approach, the N_{ss} value as a function of frequency can be indicated as [64]:

$$N_{ss} = \frac{(G_m/\omega)_{max}}{\left(\left((G_m/\omega)_{max} / C_{ox} \right)^2 + \left(1 - (C_m / C_{ox}) \right)^2 \right)} \left(\frac{2}{qA} \right) \quad (2.17)$$

where $(G_m/\omega)_{max}$ demonstrates the maximum G_m/ω value, and C_m depicts the capacitance relating to the value of $(G_m/\omega)_{max}$ [65].

2.12 Impedance spectroscopy and equivalent circuit model [24,25,66,67]

The fundamental of impedance spectroscopy is an examination of system response by system perturbation with a minute amplitude of the AC signal with frequency excitation in a broad range. Per the response of the system to the sinusoidal disturbance, the observable number and dimensions of the arcs in the Z' - Z'' curve can be employed to perceive the behavior of electrical phenomena taking place within the device. This approach is particularly appropriate for exploration and perception regarding the electrical attributes in the photovoltaic cell, optoelectronic, solid-state multilayered, and heterojunction devices. Commonly, for optoelectronic, solid-state multilayered, and heterojunction devices, impedance spectroscopy can be utilized to clarify the electrical attributes concerning the charge carrier portage, the charge behaviors at the interfaces, carrier relaxation phenomenon, inclusive of accumulation and recombination process.

Based on an ideal resistance, the current flow through the resistor and voltage across the resistor based on Ohm's rule can be described by the following equation:

$$V = IR \quad (2.18)$$

where V , I and R are the voltage across the resistor, current and resistance, respectively.

The electrical impedance is in the form of vector diagrams and complex representations, which is more complicated than the common concept of resistance attributable to the phase difference. The Z' - Z'' examination is managed with a small amplitude of the AC signal with frequency excitation in a broad range. The resultant impedance ($Z(\omega, t)$) of the system can be calculated by the following relation:

$$Z(\omega) = \frac{V(\omega, t)}{I(\omega, t)} \quad (2.19)$$

where $V(\omega, t)$ is a small amplitude of voltage that is biased in the range of frequency ($f = \omega/2\pi$), and $I(\omega, t)$ is the corresponding current.

In the term of the complex number, a small amplitude of voltage can be expressed by the following function:

$$V(\omega, t) = V_0 \exp(j\omega t) \quad (2.20)$$

Also, the corresponding AC current is given as follows:

$$I(\omega, t) = I_0 \exp(j\omega t - j\theta) \quad (2.21)$$

where θ is denoted that is the phase difference of $V(\omega, t)$ and $I(\omega, t)$, and j is $(-1)^{1/2}$. When Eq. 2.19 is substituted by Eq. 2.20 and Eq. 2.21, it can be described as follows:

$$Z(j\omega) = \frac{V_0}{I_0} \exp(j\theta) = Z_0 \exp(j\theta) \quad (2.22)$$

By Euler's relation and substitution of Z_0 by $|Z|$, Eq. 2.22 can be written below:

$$Z(j\omega) = |Z| (j \sin \theta + \cos \theta) \quad (2.23)$$

Commonly, the impedance function can be explained by the following relation:

$$Z(\omega) = Z' - jZ'' \quad (2.24)$$

where Z' is term of real part of impedance ($Z' = j |Z| \cos\theta$) and Z'' is term of imaginary part of impedance ($Z'' = j |Z| \sin\theta$).

When the voltage biased across a resistor with resistance (R) is $V(\omega, t) = V_0 \sin(\omega t)$ and the current flow through the resistor is $I(\omega, t) = I_0 \sin(\omega t)$, the impedance for a resistor can be explained by the given equation:

$$Z_R(\omega) = \frac{V(\omega, t)}{I(\omega, t)} = R \quad (2.25)$$

This case appears when the voltage bias and current are in phase. In the event of capacitor possessing capacitance (C), the current that flows by the applied sinusoidal voltage across the capacitor is $I(\omega, t) = \omega C V_0 \sin(\omega t)$. Consequently, the impedance for a capacitor can be expressed as given relation:

$$Z_C(\omega) = \frac{V(\omega, t)}{I(\omega, t)} = \frac{1}{\omega C} \quad (2.26)$$

And the complex impedance of capacitor can be written as follows:

$$Z_C(\omega) = \frac{1}{j\omega C} \quad (2.27)$$

Furthermore, CPE is one of the basic components widely applied to model the system. CPE is perceived as the imperfect behavior of capacitors that occurred from the non-ideal behavior of materials such as porous interfaces. The impedance characteristic of CPE can be explained by the following equation:

$$Z_{CPE}(\omega) = \frac{1}{(j\omega)^{\alpha} CPE} \quad (2.28)$$

Typically, the number of half-circle arcs relies on the materials and material layers, in addition to the interfaces. The Z'' - Z' characteristics can interpret an equivalent circuit model related to the heterojunction behavior. The components in the equivalent circuit model may include resistors, capacitors, or inductors, which hinge on the device response to the biased AC signal. In the easy case, a shunt arrangement of parallel resistance (R_p) and capacitance can provide one symmetric semicircle where the starting position is the origin (0,0) point, as indicated in Figure 2.21 (a). The R_p value may be superintended by the process of charge carriage between the interfaces of junctions, where was specified via the resistance of charge carriage [61,66].

The capacitance of a semiconductor device with a p-n junction can be classified as chemical capacitance and depletion capacitance. When the beginning point of arc shifted to higher Z' , the devices should be modeled with an equivalent circuit having the parallel association of R_p and capacitance connected with series resistance (R_s), as illustrated in Figure 2.21 (b). The R_s value is attributable to the resistance from Ohmic contact, inclusive of electrodes and the neutral regions [18,68]. For the uncomplicated instance, the Z'' - Z' curve gives a single asymmetric half-circle that the center of a semicircular arc is kept under the Z' coordinate with moving to the superior Z' values of the beginning site. This feature relates to the circuit model comprising the shunt arrangement of the parallel resistance (R_p) and constant phase element (CPE) serially combined with R_s [67-69], as demonstrated in Figure 2.21 (c). The CPE parameter conveys the imperfection of capacitor emanating from non-ideal conduct of materials, including an adjustable parameter to compensate for non-homogeneity in the blocking interfaces on account of porous interfaces or surface states [18,68]. The electrical impedance corresponding to the equivalent circuit model in Figure 2.21 (c) can be expressed through the following relation:

$$Z(\omega) = R_s + \frac{R_p}{1 + R_p (j\omega)^s \text{CPE}} \quad (2.29)$$

where ω exhibits angular frequency. In this case, CPE specifies the magnitude of the constant phase element, and s is a deviation of the magnitude of CPE from the ideal dependent capacitor. The magnitude of deviation was in a range between 0 and 1. If the deviation value is equal to 1, CPE can be considered as an ideal capacitor.

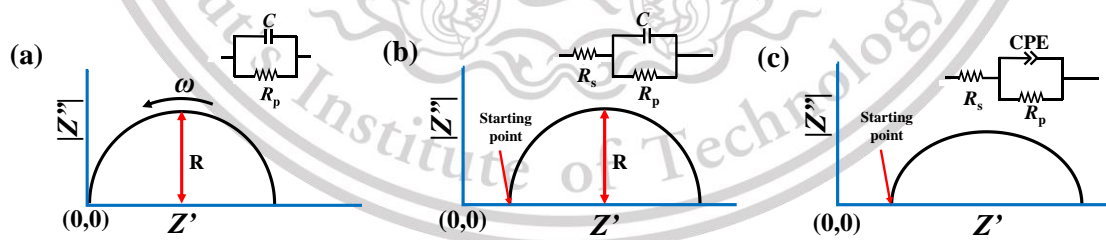


Figure 2.21 Z' - Z'' spectra with the related equivalent circuit model of (a) R_p and C in parallel connection, (b) shunt circuit of R_p and C serially connected with R_s (c) parallel association of R_p and CPE serially combined with R_s [67].

2.13 XRD [70]

XRD is a usual approach for examining the crystal structures and atomic spacing. XRD is based on constructive interference of monochromatic X-rays and a crystalline sample. These X-rays are produced by a cathode ray tube. Then the X-rays are filtered to create the monochromatic radiation and directly focused on the specimen. The interaction of the incident rays on the specimen creates the constructive interference with a diffracted ray relying on Bragg's Law ($n\lambda = 2d\sin\theta$). This relation associates with the electromagnetic radiation wavelength to the diffraction angle and the lattice spacing in a crystalline sample. Then, these diffracted X-rays are inspected and counted. From 2θ scanning, all possible diffraction directions of the lattice should be detected on account of the random material orientation. Conversion of the diffraction peaks to d-spacings allows identification of the mineral because each element possesses a specific d-spacing set. Typically, this approach is achieved by comparing d-spacings with standard reference patterns.

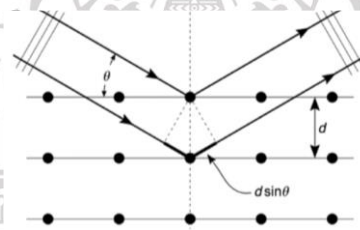


Figure 2.22 Bragg reflection by a set of parallel planes with interplanar distance [70].

2.14 SEM [71]

In SEM examination, a focused beam of high-energy electrons is used to generate various signals at the solid specimen surface. The signals from electron-sample interactions expose the features such as morphology, chemical composition, crystalline structure and material orientation coated on the substrate. A 2-dimensional image is produced the spatial exhibition of the surface features. The examination by SEM can apply to characterize the selected locations on the surface of a specimen. This technique is useful in qualitatively or semi-quantitatively determining chemical compositions (Energy-dispersive X-ray spectroscopy), crystalline structure, and crystal orientations (Electron backscatter diffraction).

For SEM technique, the electrons are accelerated with considerable kinetic energy. The kinetic energy is dissipated as various signals generated by electron-sample interactions when the incident electrons are decelerated in the solid specimen. Figure 2.23 reveals the interaction of electron beam with specimen and signal emitted from the specimen. These signals consist of secondary electrons, backscattered electrons, This material is reserved for educational use only, not allowed for commercial use.

diffracted backscattered electrons, photons, visible light (cathodoluminescence), and heat. Secondary electrons and backscattered electrons are generally employed to produce the image of the specimen. The secondary electrons are chiefly significant for demonstrating the morphology and topography of surface samples. The backscattered electrons are chiefly significant for revealing the contrasts in composition in multiphase samples. The diffracted backscattered electrons are utilized to determine crystal structures and orientations of minerals. The photons, which are characteristic X-rays, are employed to characterize the elemental and continuum X-rays. SEM analysis is a non-destructive technique.

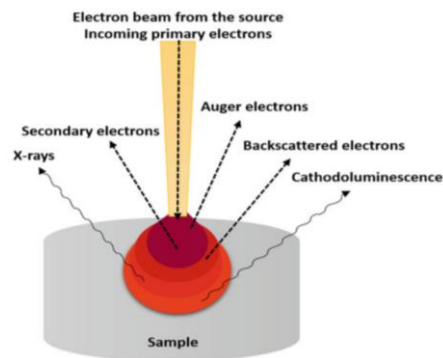


Figure 2.23 Interaction of electron beam with specimen and signals from sample [71].

2.15 Raman spectroscopy [72]

Raman examination is an approach where scattered light is employed to examine the vibrational energy modes of a specimen. Raman examination is on the basis of Raman scattering, which discloses the vibrational, rotational and other low-frequency modes of molecules. Raman examination can use to explore the chemical and structural information, including the element identification based on their Raman characteristic. The specific Raman characteristic can be specified as a fingerprint. This method extracts the information by inspecting Raman scattering from the specimen. The sample is exposed to an intense monochromatic beam in the frequency range of visible, NIR or near-UV light during measurement. The electromagnetic radiation, interacting with a substance, can be transmitted, absorbed, or scattered.

A molecule in an initial state (a rotational, vibrational or rotational-vibrational state) is excited by an incident photon to a higher level (virtual state), as shown in Figure 2.24. Subsequently, the molecule will return to another lower state and emit a photon. ν_0 demonstrates the ground state while ν_1 and ν_2 depict the excited states. In the event of the final state identical to the initial state, the emitted frequency of photon will be equal to the emitted frequency of the incident photon, which this

This material is reserved for educational use only, not allowed for commercial use.

Forbidden to modify the content, and cite the document when use.

phenomenon is mentioned as Rayleigh scattering. In the case of the final state over or below the initial state, the frequency of emitted photon will be shifted to lower or higher values, which this case can be referred as Stokes Raman or anti-Stokes Raman scattering, respectively. Anti-Stokes Raman scattering can take place in molecules at an excited state. The intensity of Stokes Raman scattering is over the intensity of anti-Stokes Raman scattering according to the Boltzmann distribution.

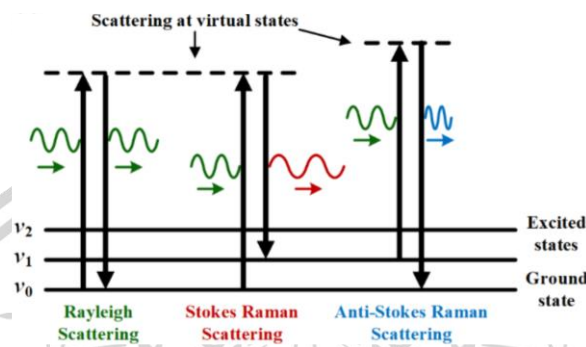


Figure 2.24 Raman scattering [72].

2.16 Significant parameters

2.16.1 Dark current [73,74]

In electronic engineering, dark current is the small current that flows through devices such as photodiodes when no photons enter the device. It is referred to as reverse bias leakage current in non-optical devices and all diodes. Physically, the dark current components are the recombination current in the neutral regions. The recombination current occurs in the space charge zone and the recombination current at the interface states between the two materials of heterojunction.

The p-n diode is a passive device, which allows current to flow in one direction. Figure 2.25 exhibits a typical I - V characteristic for a p-n diode. Red dashed line indicates the breakdown voltage, which the highlighted zone with blue color is the breakdown zone of a diode. This zone cannot be elucidated by the diode function (Eq. 2.3). At 0 V, the diode system is in an equilibrium state leading to non-created current. When voltage across the diode is over 0 V, it is called forward bias. The current of diode in the forward bias region is determined using Eq. 2.3. On the other hand, the heterojunction diode, which is biased with a voltage below zero bias and higher than break down voltage, allows a small current in reverse bias. When the bias voltage is over breakdown point, an abundant reverse current is produced, which rises from the Zener and avalanche breakdown. The turn-on voltage is the required forward voltage of diode before the diode begins to create the current in the forward direction. As manifest in Figure 2.25, the value of turn-on voltage is around 0.7 V.

This material is reserved for educational use only, not allowed for commercial use.

Forbidden to modify the content, and cite the document when use.

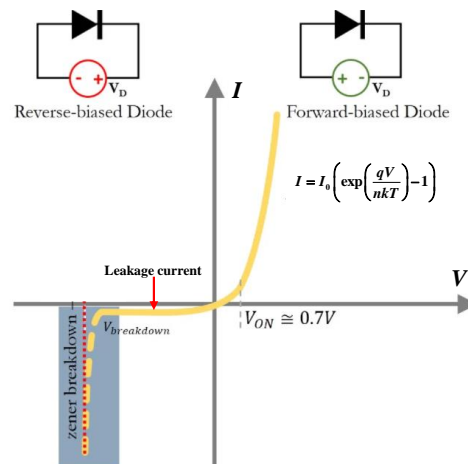


Figure 2.25 Characteristic curve of I - V for p-n heterojunction diode [74].

2.16.2 Photocurrent [75]

Photocurrent is the electric current through a photosensitive device, such as a photodiode, when photons are entering the device. This current should be more than the dark current when the photodiode is operating. The photocurrent may originate in the photoelectric, photoemissive, or photovoltaic effect. The photocurrent may be enhanced by internal gain caused by interaction among ions and photons under the influence of applied fields.

2.16.3 Ideality factor [19-21]

The parameter of n can indicate the possible mechanism for carrier transportation across a junction. The denotation of n values can be described by three transportation mechanisms such as diffusion, generation-recombination, and tunneling. If the value of n is equal to one, the transportation mechanism of the carrier across the junction is particularly governed by the process of thermal diffusion. If the value of n is higher than one and nearly two, generation-recombination will be the remarkable transportation mechanism that controls the flow of carrier within the junction. In addition, if the n value is higher than two, the tunneling process will notably dominate the transportation mechanism of the carrier.

2.16.4 Barrier height [19-21]

Based on metal-semiconductor device, ϕ_b at a steady state relies on the association of the metal and semiconductor. ϕ_b is a barrier of the potential energy for charges induced at a heterojunction. The barrier, which owns the rectifying action characteristics, is proper for application in the heterojunction diodes. ϕ_b is a significant diode parameter explaining the barrier height in the junction interface for the diodes.

2.16.5 Interface state density [76,77]

An interface state is an allowed energy level at the interface [76]. The localized interface states may serve as recombination or trap states relying on their position in the bandgap [77]. Any states between the quasi-Fermi levels for electrons and holes are a recombination center. A trap acts both as an electron trap and a hole trap, depending on its state of occupancy. When the trap is empty, it is ready to receive an electron, and thus it is operating as an electron trap. When the trap contains an electron, it is ready to receive a hole, and hence is a hole trap. Under light irradiation, the diagram of recombination centers and traps is shown in Figure 2.26 (b). The localized interface states above the Fermi level in the n-type material and under the Fermi level in the n-type material will then act as electron traps and hole traps, respectively.

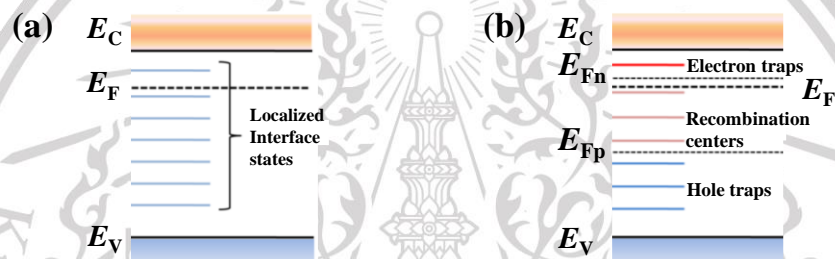


Figure 2.26 Diagram of interface states under (a) dark and (b) irradiation [77].

For the heterojunction diodes, the interface states within the junction behave as the recombination centers and raise the leakage currents, including trap centers [78]. Consequently, the density of interface state should be minimal as possible. Figure 2.27 depicts the presence of interface states in the heterostructure diodes.

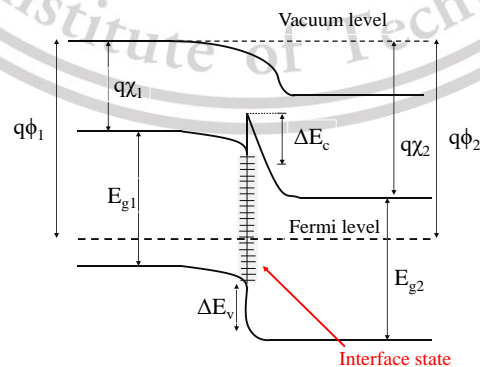


Figure 2.27 Interface state existing at the interface for heterojunction diode [78].

2.16.6 Series resistance [19-21]

Generally, R_s is the current-limiting factor, which should be the lowest possible value. R_s can occur from the different causes such as the contact between the probe wire and the electrodes, the back contact, a dirt film or particles between the back contact and base, the resistance of the neutral bulk in semiconductor and non-homogenous films due to the incorporated elements.

2.16.7 Parallel resistance [67,69]

R_p is associated with the interface charge transport process, defined by the charge transfer resistance. R_p can occur from the different causes, which the transportation of charge across the heterogeneous between the layers of interface, might be dependent on surface roughness.

2.16.8 Constant phase element [67,69]

CPE conveys the non-ideality, including an adjustable parameter to recompense for non-homogeneity in the blocking interfaces because of the surface states, surface roughness, defects or grain boundaries. The standard deviation (s) of CPE from the ideal capacitor is between -1 and 1. For $s = 1$, CPE can be deemed a capacitance. For $s = 0$, it is a reciprocal of resistance. For $s = -1$, CPE means an inductance. For the experimental results, CPE can be assumed to be a capacitance when the s value is in a range from 0.9 to 1.

2.16.9 Activation energy [75]

In physics, activation energy (E_a) is the energy in excess over the ground state, which must be added to an atomic or molecular system to allow a particular process to take place. In chemistry, E_a is defined as the minimum energy required to start a chemical reaction.

2.17 Literature reviews

2.17.1 Related works for p-Si/n- β -FeSi₂ devices built by FTS

Figure 2.28 uncovers the energy band diagram for the p-Si/n- β -FeSi₂ devices produced by FTS [78]. The Si material holds an energy bandgap of 1.12 eV and an electron affinity of 4.05 eV. For the β -FeSi₂ created via FTS, its energy bandgap was about 0.85 eV, and the threshold energy of the incident photon conforming to the ionization potential was 4.71 eV. Thus, the electron affinity of β -FeSi₂ layer was 3.86 eV. In equilibrium, the Fermi level of β -FeSi₂ was neighboring to the conduction band since its carrier densities were high between 10^{17} and 10^{18} cm⁻³, and its donor level was situated beneath the conduction band with a minor value of 20 meV. The expansion of depletion regime was entered into the Si layer. Its built-in potential (qV_{bi}) related to the utmost limit of the open-circuit voltage, which was about 1.02 eV. This qV_{bi} value is adequate to collect the photocarriers efficiently. Further, the spike is noticeable in the valence band due to the discontinuity of energy band alignment, which affects the photo-created holes in the β -FeSi₂ layer. For this reason, the transferred holes to Si layer can rise through the interface states, which might result in tunneling. Another significant obstacle is the lattice mismatch between the dissimilar semiconductors, which brings about the interface states at the junction interface. As a result, they engender the recombination hubs and the rise in tunneling current.

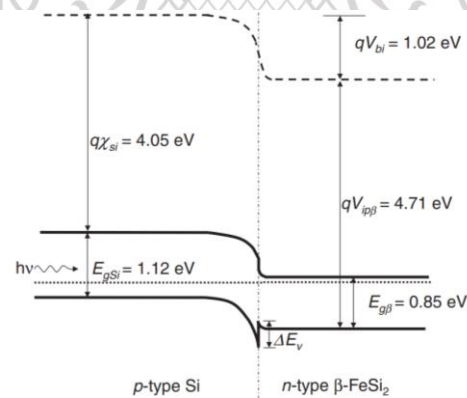


Figure 2.28 Band diagram demonstration of the p-Si/n- β -FeSi₂ heterojunctions constructed employing FTS [78].

M. Shaban et al. explored the NIR photodetection at room temperature of p-Si/n- β -FeSi₂ devices created via FTS [79]. The NIR irradiation was operated by a laser with 1.31- μ m wavelength and 6-mW power. Figure 2.29 disclosed the dark and irradiated I - V curves of the created devices. The formed devices exposed an effective rectifying action corresponding to the common p-n behavior. The forward current was around two orders of magnitude beyond the reverse current. The leakage currents in

This material is reserved for educational use only, not allowed for commercial use.

the dark at -1 V and -5 V were 5 μA and 20 μA , respectively. The leakage current was attributable to the propagated Fe atoms from the $\beta\text{-FeSi}_2$ layer to Si layer. The propagated Fe atoms engender the hubs of leakage current and trap centers for the photocarriers, including the interface defects. The photocurrents at 0 V and -5 V were about 20 μA and 70 μA , respectively. Also, the current responsivity was around 3.3 mA W^{-1} at 0 V. Nonetheless, their NIR response was weakfish, which might stem from the interface states at the interface. This vital issue engenders the hubs for leakage current and trapping the photocarriers. Based on the inset of Figure 2.29, the dynamic resistance at 0 V was $3.10 \times 10^6 \Omega$ at room temperature. Due to the Johnson noise at 0 V, the detectivity can be appraised using the dynamic resistance and current responsivity at 0 V. At room temperature, the NIR detectivity of the device was $1.5 \times 10^9 \text{ cm Hz}^{1/2} \text{ W}$. Especially, this detectivity value can allegorize with the detectivity of presenting photodetectors such as InAsSb/InAsSbP and InAs/GaAs photodiodes.

Also, M. Shaban et al. revealed the photoresponse and quantum efficiency with a responsivity of the p-Si/n- $\beta\text{-FeSi}_2$ photodiodes created by FTS [79]. The photoresponse trace plotted photon energy of the p-Si/n- $\beta\text{-FeSi}_2$ photodiodes examined under the NIR illumination at 300 K and zero bias voltage is exhibited in Figure 2.30. The wavelength of the device photoresponse was about 1.5 μm , preferable to the Si cutoff wavelength, which this value tallied with the bandgap value of $\beta\text{-FeSi}_2$ composite. The included illustration of Figure 2.30 revealed the external quantum efficiency of the heterojunction devices in the negative voltage range under the 1.31- μm irradiation with 6 mW. The efficiency value was observed at about 0.32% at 0 V, and it rose to 1.07% when the devices were biased to -5 V.

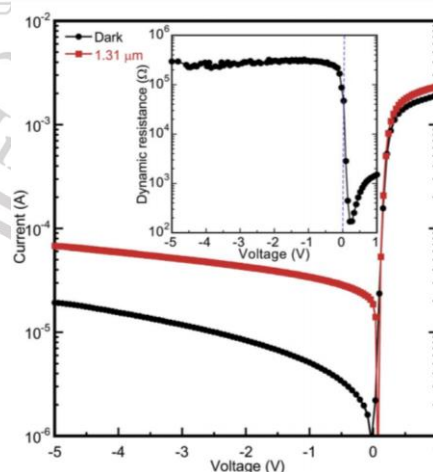


Figure 2.29 Dark and irradiated I - V profiles at 300 K of the p-Si/n- $\beta\text{-FeSi}_2$ photodiodes built by FTS. The inset unveils the dynamic resistance plot [79].

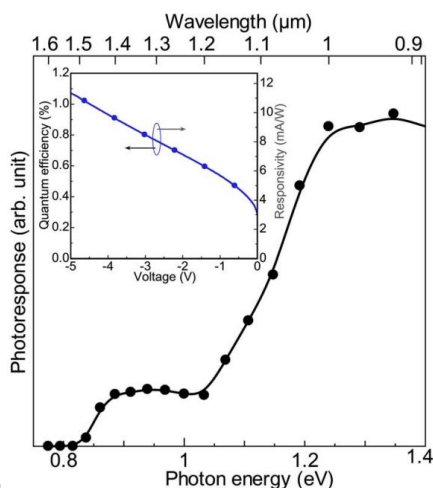


Figure 2.30 NIR response profile of the built p-Si/n- β -FeSi₂ device at 0 V and 300 K. The inserted image is the quantum efficiency and responsivity in negative voltages under the irradiation at 1.31 μ m and 6 mW [79].

2.17.2 Related works for p-UNCD/n-Si devices formed by PLD

S. Ohmagari et al. created the p-UNCD/n-Si devices by PLD [80]. The ionization potential of p-UNCD was 5.2 eV. The ionization potential value of an a-C:H matrix was 4.5–5.5 eV. The energy bandgap of a-C:H was about 1.0 eV. The electron affinity and the energy bandgap of Si are 4.05 eV and 1.12 eV, respectively. The built-in potential of the devices was about 0.55 eV. The energy band diagram of the p-UNCD/n-Si devices built by PLD is exhibited in Figure 2.31 (a). The discontinuity of valence level was -0.03 eV while the discontinuity of conduction band was -0.15 eV. Both minor values are beneficial to the carrier diffusion and the photocurrent collection. The partial numbers of UNCD grains might be amalgamated at the interface, as exposed in Figure 2.31 (b). The transport ways of electrons under positive bias were two. The blue arrow is the way from the n-Si to an a-C:H matrix while the red arrow is the way from the n-Si to the accumulated UNCD grains. The accumulation of UNCD grains in the UNCD/a-C:H films at the interface may act as the hubs for trapping carriers. This acts as a recombination center leading to large leakage currents.

T. Hanada et al. revealed the UV photodetection of the p-UNCD/n-Si devices formed by PLD [81]. Figure 2.32 exhibited the dark and irradiated I - V profiles at room temperature. The irradiation condition was performed by monochromatic light with a 254-nm wavelength. The devices provided good rectification like the ordinary p-n junctions. A rectification ratio was four orders of magnitude at ± 5 V. However, the leakage current at room temperature was somewhat large. The devices disclosed the minor photocurrent with a large leakage current, which might occur from the interface states at the hetero-interface region of the device.

This material is reserved for educational use only, not allowed for commercial use.

Forbidden to modify the content, and cite the document when use.

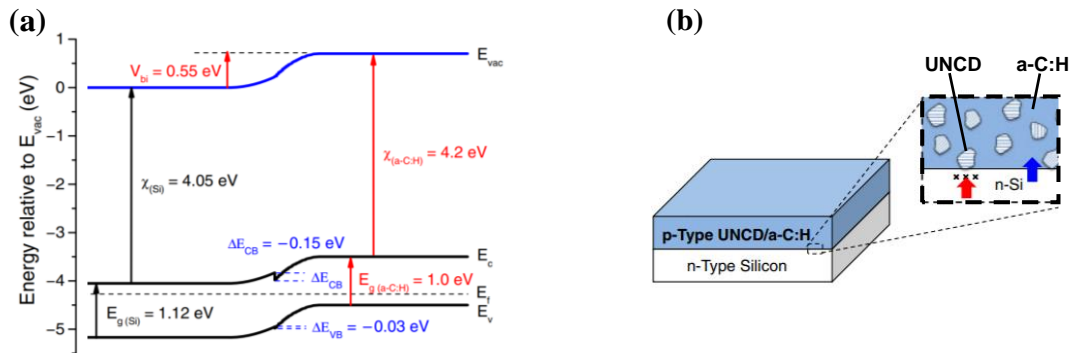


Figure 2.31 (a) Energy band diagram of the p-UNCD/n-Si junctions formed by PLD (b) configuration schematic of the hetero-interface [80].

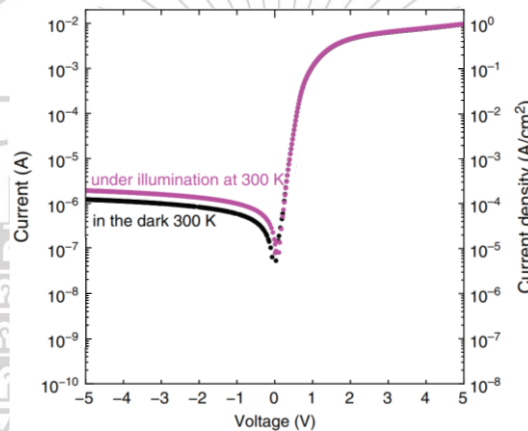


Figure 2.32 Dark and irradiated I - V profiles at room temperature for the p-UNCD/n-Si devices fabricated via PLD [81].

2.17.3 Related works for p-UNCD/n-Si devices built by CAPD

Y. Katamune et al. formed the photodiodes comprising n-Si wafers and 5 at.% B-incorporated UNCD/a-C:H films by CAPD [82]. The carrier concentration of the B-incorporated UNCD/a-C:H films was between $9 \times 10^{15} \text{ cm}^{-3}$ and $1.5 \times 10^{16} \text{ cm}^{-3}$ while the n-Si wafers held a carrier concentration about $5 \times 10^{15} \text{ cm}^{-3}$. The electrical conductivity of the created films was around $6 \times 10^{-2} \text{ S cm}^{-1}$. Figure 2.33 revealed the energy band configuration of p-UNCD/n-Si devices created by CAPD. The threshold energy of incident photon tallying with the ionization potential for the UNCD/a-C:H films created by CAPD was 5.22 eV. The energy bandgap of coated films was about 1.7 eV ascribable to the a-C:H matrix. Based on the energy band schematic, the transportation of carriers was occurred in the a-C:H matrix. The built-in voltage of the created devices was about 0.88 eV. The discontinuity of the conduction band is not appeared. Thus, it is advantageous for the transportation of photocarriers in the UNCD/a-C:H side to the Si layer. Also, the discontinuity of valence band is insignificant.

This material is reserved for educational use only, not allowed for commercial use.

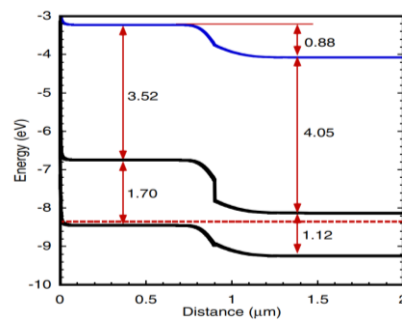


Figure 2.33 Schematic illustration of the energy band diagram of p-UNCD/n-Si heterojunction devices manufactured through CAPD technique [82].

Y. Katamune et al. also revealed the UV detection at room temperature of the p-UNCD/n-Si devices formed by CAPD [82]. Figure 2.34 uncovers the I - V profiles of the devices tested under the darkness and irradiation by a monochromatic lamp with 254-nm wavelength and 2-mW power. The devices exhibited an appropriate rectifying action like the ordinary p-n diodes with large leakage current under the negative bias. Under the irradiation with UV light, the heterojunction photodiodes manifested the photo-created carriers and signal/noise ratio, which was clearly better than that of GaN photodiodes. The production of photocarriers might occur at the UNCD grains contained in the UNCD/ a-C:H films. These carriers occurred by light irradiation were portaged through the a-C:H matrix. According to the high photon energy of UV light, the productive creation of photocarriers occurring in the UNCD grains might dominate over that in the Si layer and a-C:H matrix. Howsoever, the photocurrents were weakfish, which might be due to the interface states occurring at the interface. This crucial issue could prevent the generation of photocarriers by trapping the carriers.

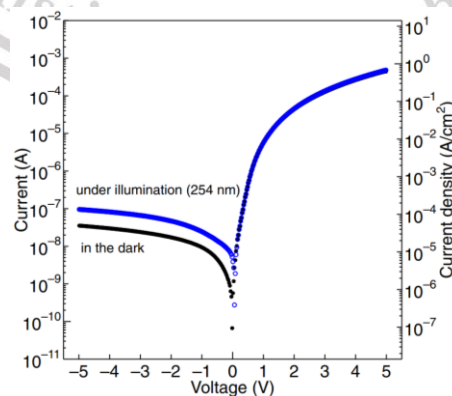


Figure 2.34 Dark and irradiated I - V curves at room temperature for the p-UNCD/n-Si photodiodes created by CAPD. [82].

Chapter 3

Experimental details

This chapter delineates the construction of the p-Si/n- β -FeSi₂ devices by FTS and p-UNCD/n-Si devices by PLD and CAPD for electrical characterization. Then, the β -FeSi₂ films formed by FTS and UNCD films constructed by PLD and CAPD were investigated. After that, the electrical measurements for the p-Si/n- β -FeSi₂ devices and p-UNCD/n-Si devices created by PLD and CAPD were expounded. The last section clarifies the extraction processes of significant parameters.

3.1 Manufacture of p-Si/n- β -FeSi₂ heterojunctions via FTS

3.1.1 Synthesis of β -FeSi₂ layer

The manufacture of heterojunctions comprising the p-Si wafer and n- β -FeSi₂ films was carried out using the FTS apparatus, which is exposed in Figure 3.1. The sputtering process for the β -FeSi₂ film coating was accomplished through the usage of a couple of FeSi₂ alloy targets having 4N purity. The Si(111) wafer with p-type conduction, 260- μ m thickness and 10-20 Ω cm resistivity was utilized as a substrate.



Figure 3.1 FTS apparatus for film creation.

For the substrate cleaning, the acetone and methanol with 99.5% purity were applied to clean up any organic residues and oils. Then, the deionized (DI) water was used to remove the remaining solvents. Each rinsing step was managed for five minutes using an ultrasonicator. After that, hydrofluoric (HF) acid diluted with a concentration of 1% was utilized to clear the natural oxide on the Si wafer surface. After removal of the oxide layer, DI water was used for cleaning the excess HF.

After completing the cleaning process, nitrogen gas (5N purity) was blown throughout the Si wafer substrate to eliminate humidity. Then, the Si wafer was instantaneously transferred to the FTS chamber with a schematic configuration, as

demonstrated in Figure 3.2. The Si substrate was attached to a holder with a distance of 7.5 cm away from the FeSi₂ targets. A combined system of a rotary pump and a turbomolecular pump was utilized to evacuate the air inside the FTS chamber. Through evacuation, interior pressure was reduced to 10⁻⁵ Pa. Argon (Ar) gas (6N purity) injection was regulated to acquire the operating pressure at 1.33 × 10⁻¹ Pa. A steady flow of Ar gas was fixed at 15 sccm using an Ar mass flow. The backside of the Si wafer was heated to 600 °C via a heater regulated using a temperature controller, and the 600 °C substrate temperature was fixed until the film creation was completed. The sputtering voltage was applied with 1 kV from DC power generator while the generated current was about 1.5 mA. The sputtering time was around 24 hours, and the β-FeSi₂ film thickness was around 300 nm. Table 3.1 presents the condition for the creation of the β-FeSi₂ layer on the Si wafer substrate.

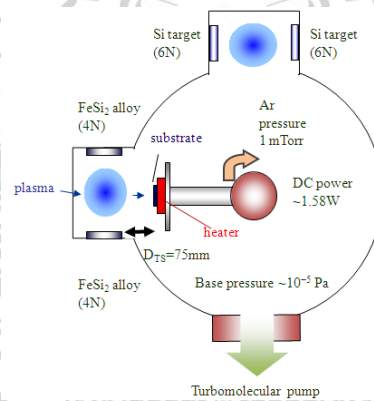


Figure 3.2 Schematic configuration of FTS apparatus.

Table 3.1 Condition for depositing the β-FeSi₂ layer.

Process variable	Condition
Sputtering target	FeSi ₂ (purity: 4N)
Substrate	p-type Si(111)
Substrate thickness	260 μm
Space between holder and target	7.5 cm
Initial pressure	3 × 10 ⁻⁵ Pa
Ar gas flow rate	15 sccm
Operating pressure	1.33 × 10 ⁻¹ Pa
Substrate temperature	600 °C
Discharge voltage	1 kV
Discharge current	1.5 mA
Sputtering rate	0.15 nm/min
Film thickness	300 nm

This material is reserved for educational use only, not allowed for commercial use.

Forbidden to modify the content, and cite the document when use.

3.1.2 Electrode creation for p-Si/n- β -FeSi₂ junctions built by FTS

The native oxide layer was purged before the electrode fabrication by diluted HF acid with 1% concentration. Then, the remaining HF solvent was instantly rinsed with DI water. Afterward, radio-frequency magnetron sputtering (RFMS) that the system was superintended via an RF power generator was employed for coating the front and back Ohmic electrodes at room temperature. The equipment of RFMS is manifested in Figure 3.3. The creation of the electrodes was carried out under the conditions shown in Table 3.2. The formation of a front metallic electrode on the Si surface was carried out using a palladium (Pd) target having 4N purity. The pattern of front Pd electrode was finger shape. Employing an aluminum (Al) target with 4N purity, the back metallic electrode was fabricated on the whole β -FeSi₂ surface. The schematic diagram and the photograph of created p-Si/n- β -FeSi₂ heterojunctions with electrodes are presented in Figure 3.4 (a) and (b), respectively. The area of the fabricated heterojunction was approximately 0.1 cm².

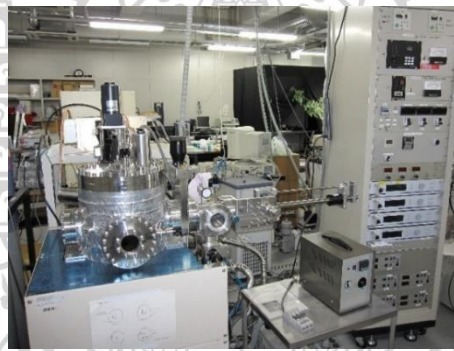


Figure 3.3 RFMS system to construct the electrodes.

Table 3.2 Conditions of Ohmic contact creation for p-Si/n- β -FeSi₂ heterojunctions.

Electrode	Al	Pd
Sputtering target	Al (purity: 4N)	Pd (purity: 4N)
Substrate	β -FeSi ₂ side	Si side
Initial pressure	1×10^{-5} Pa	1×10^{-5} Pa
Ar gas flow rate	10 sccm	10 sccm
Operating pressure	2.66×10^{-1} Pa	1.33×10^{-1} Pa
Substrate temperature	Room temperature	Room temperature
Sputtering power	200 W	200 W
Sputtering rate	4.2 nm/min	8.3 nm/min
Thickness of film	500 nm	500 nm

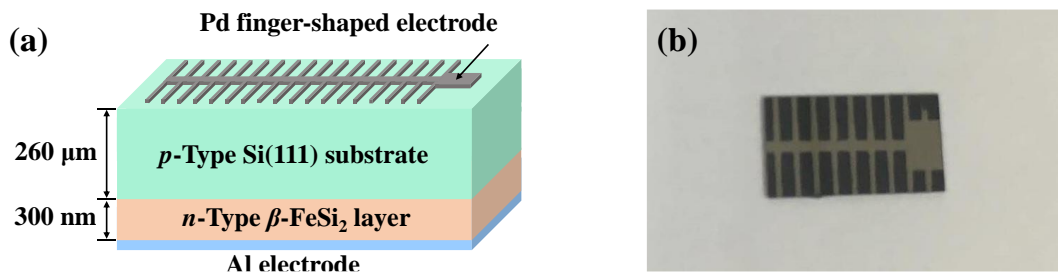


Figure 3.4 (a) Configuration and (b) photograph of the built p-Si/n-β-FeSi₂ heterojunctions with electrodes.

3.2 Creation of p-UNCD/n-Si heterojunctions by PLD

3.2.1 Creation of p-UNCD layer

The synthesis of pure UNCD and p-UNCD films was managed using PLD. Figure 3.5 reveals the PLD apparatus used for the film construction. The p-UNCD films were produced using the graphite target rod comprising 0.1 at.% boron element. The radiation source of PLD apparatus was an ArF excimer laser having a wavelength of 193 nm. The substrate for producing the film layer was Si wafer with thickness of 260 μm and resistivity of 1-5 Ω cm, which holds the n-type conduction.

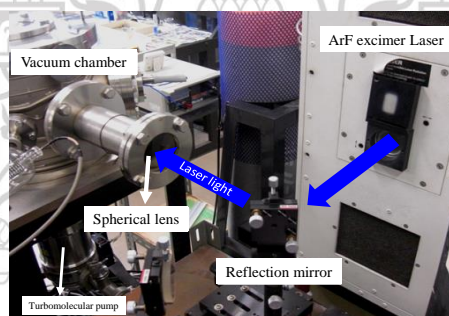


Figure 3.5 PLD system.

The surface of Si wafer was cleaned to eradicate the dust, oils and residues by acetone, methanol, and DI water, respectively. For each step, the period for cleaning was performed for 5 minutes in an ultrasonic cleaner. Next step, the Si wafer substrate was dipped in a solution of hydrofluoric acid to eradicate the native oxide on the surface layer. Ultimately, the Si wafer was blown by N₂ gas.

After the cleaning process, the Si wafer substrate was mounted on a substrate holder inside the PLD chamber, as shown in Figure 3.6. The condition for p-UNCD film construction was indicated in Table 3.3. The substrate holder has a space of 15 mm from the target. Before coating p-UNCD layer, the evacuation was conducted through the combination system of a turbomolecular pump and a rotary pump to

acquire the initial pressure less than 10^{-4} Pa. Subsequently, H_2 gas was introduced to the PLD chamber at a constant flow rate of 5 sccm, which the operating pressure was kept at 53.3 Pa. The temperature of the substrate was heated to 550 °C and maintained at 550 °C until the film production was completed. To create the p-UNCD layer, an ArF excimer laser with 193-nm wavelength was energized with 100 mJ. The focus point of laser beam was indicated on a surface of target, which the target holder can be rotated. The laser fluence was 5 J cm^{-2} while the irradiance was $7.5 \times 10^7 \text{ W cm}^{-2}$ with the irradiation area of 2 mm^2 . The repetition rate for the laser pulses was maintained at 50 Hz. The pure UNCD films were constructed by the same condition for p-UNCD film creation where the target was replaced by a pure graphite target.

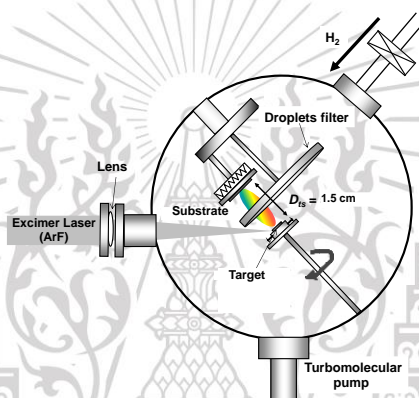


Figure 3.6 Illustration of the schematic diagram of a PLD system.

Table 3.3 Condition for depositing the p-UNCD layer by PLD.

Process variable	Condition
Target	Graphite target with 0.1 at% boron
Source	ArF excimer laser
Substrate	n-type Si(100)
Substrate thickness	260 μm
Distance between target and substrate	1.5 cm
Initial pressure	$< 10^{-4}$ Pa
H_2 gas flow rate	5 sccm
Operating pressure	53.3 Pa
Substrate temperature	550 °C
Energy of laser pulses	100 mJ
Repletion frequency of laser pulses	50 Hz
Film thickness	230 nm

3.2.2 Electrode creation for p-UNCD/n-Si junctions built by PLD

The production of both Al and Pd electrodes was executed using the condition in Table 3.4. By using the RFMS apparatus, the electrodes of front Pd and back Al were constructed at room temperature after the creation of the p-UNCD layer on the Si wafer. By the Pd target with a purity of 4N, the Pd electrode was built on the surface of the constructed film. The electrode of Al was formed on the entire surface of Si substrate by using Al target with a purity of 4N. The schematic illustration of the constructed diode comprising p-UNCD film and n-Si substrate with the Al and Pd electrodes is manifested in Figure 3.7 (a). The taken photograph of the manufactured p-UNCD/n-Si device is depicted in Figure 3.7 (b). The area of the created p-UNCD/n-Si heterojunctions was around $7.85 \times 10^{-3} \text{ cm}^2$.

Table 3.4 Condition of electrode creation for p-UNCD/n-Si junctions formed by PLD.

Process variable	Al electrode	Pd electrode
Sputtering target	Al (purity: 4N)	Pd (purity: 4N)
Substrate	Si side	UNCD side
Initial pressure	$1 \times 10^{-5} \text{ Pa}$	$1 \times 10^{-5} \text{ Pa}$
Ar gas flow rate	10 sccm	10 sccm
Operating pressure	$2.66 \times 10^{-1} \text{ Pa}$	$1.33 \times 10^{-1} \text{ Pa}$
Substrate temperature	Room temperature	Room temperature
Sputtering power	200 W	200 W
Sputtering rate	4.2 nm/min	8.3 nm/min
Thickness of film	500 nm	500 nm

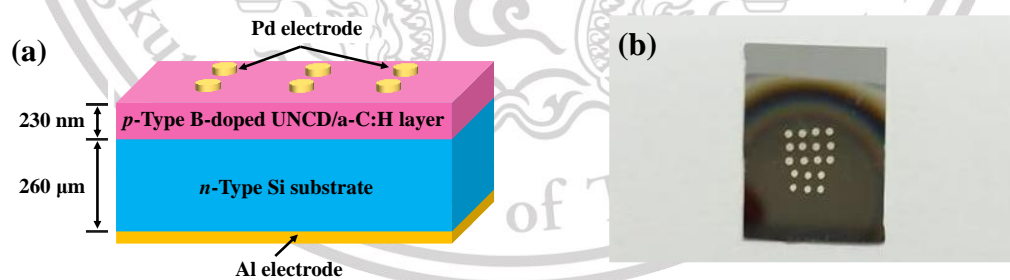


Figure 3.7 (a) Device diagram and (b) image of the p-UNCD/n-Si devices created by PLD with electrodes.

3.3 Construction of p-UNCD/n-Si heterojunctions by CAPD

3.3.1 Manufacture of p-UNCD layer

Pure UNCD films were produced using a graphite target with 4N purity using CAPD, as demonstrated in Figure 3.8. The p-UNCD films were coated using a graphite target incorporated with a 5 at.% of boron (3N purity). The n-Si wafers with a thickness of 260 μm and resistivity of 1 $\Omega\text{ cm}$ were employed as the substrates for coating the pure UNCD and p-UNCD films.



Figure 3.8 Illustration for CAPD setup.

Any contaminants on the Si substrate were eliminated utilizing acetone, methanol, and DI water, respectively. The substrates were placed in a beaker and cleansed in an ultrasonic vibrator for five minutes in each washing step. Then, the substrates were instantly dried by N_2 gas with 5N purity.

After that, the Si wafers were attached to a substrate holder in the CAPD chamber. Figure 3.9 manifests the schematic configuration of CAPD apparatus. Table 3.5 reveals the condition for coating the p-UNCD films. Before coating the film, the CAPD chamber was evacuated to an initial pressure of 10^{-4} Pa using the turbomolecular and rotary pumps with a mechanical pump. Then, H_2 gas (3N purity) was filled into the chamber. Working pressure was kept at 53 Pa. By using a temperature controller, the substrate temperature was regulated at 500 $^\circ\text{C}$. The capacitance value of capacitor, which was joined with the arc gun, was 1800 μF . To manufacture the films, the arc gun was biased at 100 V, and the pulse repetition rate of discharge was maintained at 5 Hz via an arc gun controller. The pure UNCD films were constructed using the same condition for p-UNCD film manufacture where the target was replaced by a pure graphite target. The rates for coating the pure and p-UNCD films were 0.75 to 1 nm/pulse and 1.33 nm/pulse, respectively. Thus, the pulse number for coating the pure and p-UNCD films was moderately adjusted to acquire the same thickness.

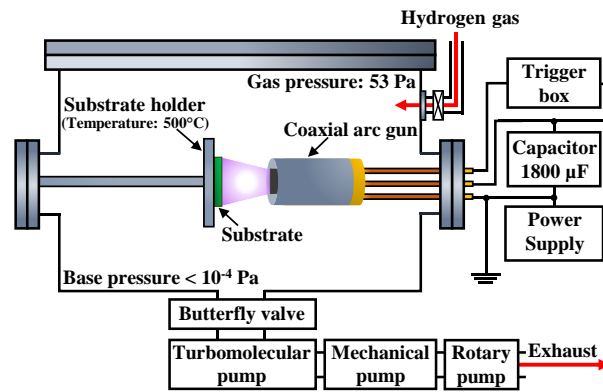


Figure 3.9 Schematic configuration of CAPD system.

Table 3.5 Condition for construction of the p-UNCD films by CAPD.

Process variable	Condition
Target	Graphite target with 5 at% boron
Substrate	n-type Si(100)
Substrate thickness	260 μm
Distance between target and substrate	1.5 cm
Initial pressure	$< 10^{-4}$ Pa
H ₂ gas flow rate	5 sccm
Operating pressure	53 Pa
Substrate temperature	500 °C
Capacitance of capacitor	1800 μF
Voltage	100 V
Repetition rate of the pulsed discharge	5 Hz
Film thickness	750 nm

3.3.2 Electrode creation for p-UNCD/n-Si junctions built via CAPD

The front and back metallic electrodes of the p-UNCD/n-Si heterojunction diodes were manufactured at room temperature using RFMS. The RFMS apparatus has three sources, which are joined with an RF power supply. Before the electrode construction, the initial pressure around 2×10^{-4} Pa was achieved using a rotary pump connected with a diffusion pump. The front electrode was manufactured on the p-UNCD layer using Pd and Au targets. The Pd and Au electrodes were coated using round-shaped hole mask with 1-mm diameter. The back electrode was constructed on the whole Si surface using Ti target. The diagram and the photograph of the p-UNCD/n-Si heterojunction diodes with electrodes are exposed in Figure 3.10 (a) and (b) respectively. The device area of the p-UNCD/n-Si diodes was 7.85×10^{-3} cm².

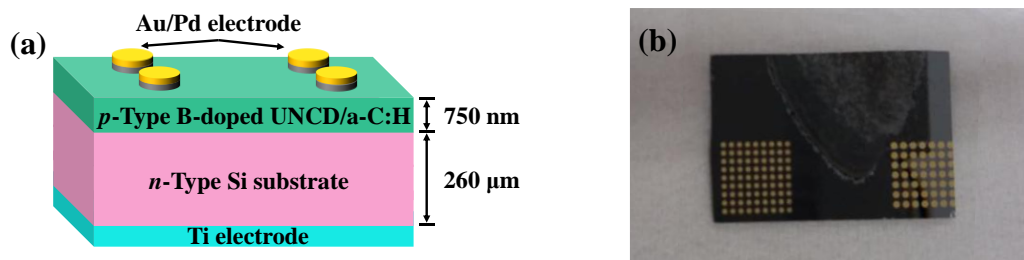


Figure 3.10 (a) Device demonstration and (b) image of the p-UNCD/n-Si heterojunction devices created by CAPD with electrodes.

3.4 Film characterizations

The investigation of β -FeSi₂ films was manipulated using XRD, FESEM surface and cross-sectional analysis. The pure and p-UNCD films created by PLD were investigated by Raman spectroscopy, and the p-UNCD films were also characterized using FESEM surface and cross-sectional observation. The pure and p-UNCD films produced by CAPD were examined by Raman spectroscopy while the p-UNCD films were investigated by FESEM surface and cross-section image.

3.4.1 Raman spectroscopy

Figure 3.11 presents a SENTERRA II dispersive Raman spectrometer at Synchrotron light research institute. Raman spectroscopy was applied to analyze the bonding characteristics of all constructed UNCD films. The Raman investigation was conducted using a 532-nm green laser source. The incident energy was maintained at roughly 25 mW. The laser beam was focused on the sample with a spot size below 1 μ m. The Raman signal was detected by a charge-coupled device, which is a highly sensitive detector.

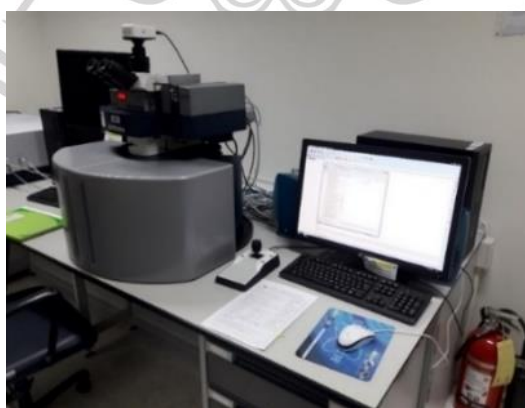


Figure 3.11 Raman spectrometer.

3.4.2 XRD examination

Figure 3.12 displays Rigaku RINT 2000/PC X-ray diffractometer at Kyushu University in Japan. The crystal structure for the created β -FeSi₂ films was examined via the X-ray diffractometer with CuK α radiation source at a wavelength of 1.542 Å. XRD profile was cautiously inspected with two scanning modes of 2θ - θ and 2θ . With 2θ - θ scanning mode, the data was collected between 20° and 70°, where a scanning step was operated at 0.02°. For 2θ scanning mode, the XRD collection was managed with an incidence angle of 4° in a range of 20° to 70° with a scanning step of 0.02°.



Figure 3.12 Rigaku RINT 2000/PC X-ray diffractometer.

3.4.3 FESEM investigation

FESEM technique was utilized to provide the surface morphology and cross section of all manufactured β -FeSi₂ and p-UNCD films. Figure 3.13 (a) exhibits an Auriga FESEM (Carl Zeiss Co., Ltd.) equipment for surface inspection, which was operated at Suranaree University of Technology. The surface investigation for the coated β -FeSi₂ films was manipulated with a magnification of 100,000 times and an acceleration voltage of 3,000 V. For the p-UNCD films coated by PLD, the surface image was captured with the 200,000x magnification and 2,000 V acceleration voltage. For the p-UNCD films created by CAPD, the surface morphology was inspected with 100,000x magnification and 3,000 V acceleration voltage.

Figure 3.13 (b) unveils an S-4700 FESEM (Hitachi High-Technologies Corporation), which was used for examining the cross-section view. This examination was operated at Thai Microelectronics Center. The cross-sectional image of the β -FeSi₂ layer on the Si wafer layer was explored with an acceleration voltage of 5,000 V and a magnification of 100,000 times. For the p-UNCD layer coated by PLD, the cross section was examined at an operating voltage of 5,000 V with 50,000x magnification. For the p-UNCD layer coated on Si wafer via CAPD, the cross-sectional features were investigated at an operating voltage of 5,000 V with a 30,000x magnification.

This material is reserved for educational use only, not allowed for commercial use.

Forbidden to modify the content, and cite the document when use.

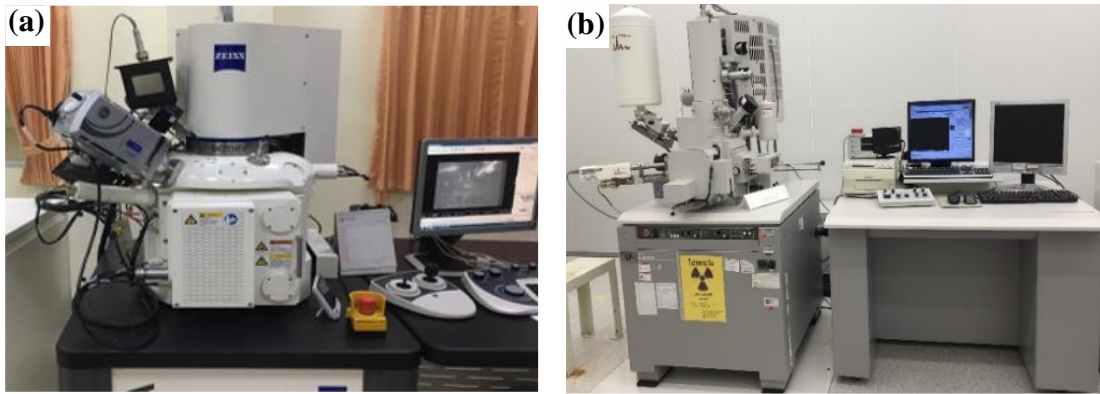


Figure 3.13 (a) Carl Zeiss Auriga FESEM and (b) Hitachi S-4700 SEM.

3.5 Electrical measurements

Figure 3.14 illustrates the diagram of equipment for electrical examinations. All electrical measurements such as I - V , C - V , G - V and Z'' - Z' were executed at Kyushu University in Japan. Figure 3.15 shows the photograph of equipment for electrical measurements. For the dark condition, the cabinet cover was closed to prevent the noise from surrounding light. The temperature was regulated by a 335 Cryogenic Temperature Controller, which is exposed in Figure 3.16. The reduction of temperature was operated by adding liquid N_2 into liquid N_2 container, as indicated in Figure 3.17. To measure the electrical characteristics, the sample was set inside the chamber, as demonstrated in Figure 3.18. The I - V examination was executed using a Keithley 2400 Series Source Measure Unit Instrument, as revealed in Figure 3.19. The C - V , G - V and Z'' - Z' characteristics were inspected utilizing an Agilent E4980A Precision LCR Meter, as indicated in Figure 3.20. The NIR radiation for p-Si/n- β -FeSi₂ devices was executed using an 1.31- μ m laser light (Neoark, TC20), as exhibited in Figure 3.21. The UV radiation for p-UNCD/n-Si devices was operated by an AS ONE Handy UV Lamp (SLUV-6) with a 254-nm wavelength, as exposed in Figure 3.22.

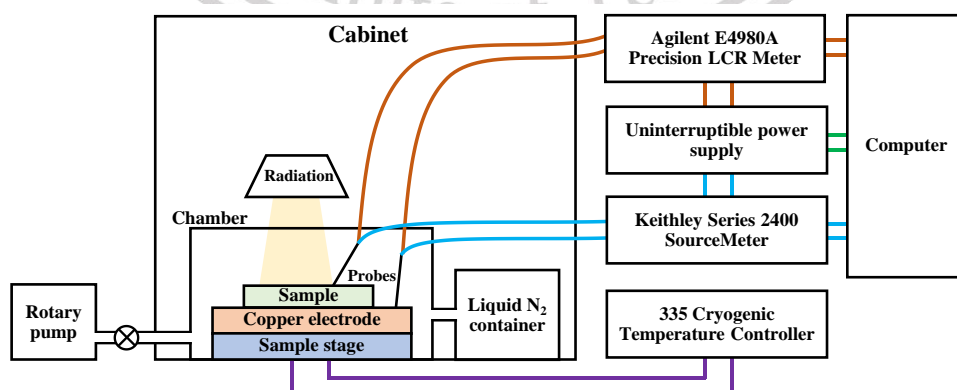


Figure 3.14 Diagram of electrical examination setup.

This material is reserved for personal use only. It is not to be used for commercial use.

Forbidden to modify the content, and cite the document when use.



Figure 3.15 Photograph of electrical examination setup.



Figure 3.16 Temperature controller.

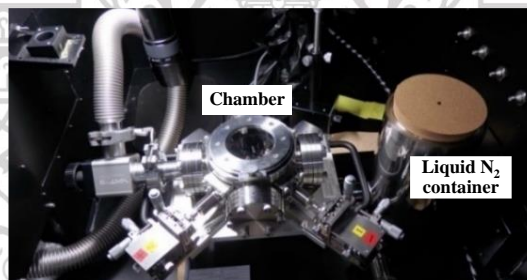


Figure 3.17 Interior of the cabinet.

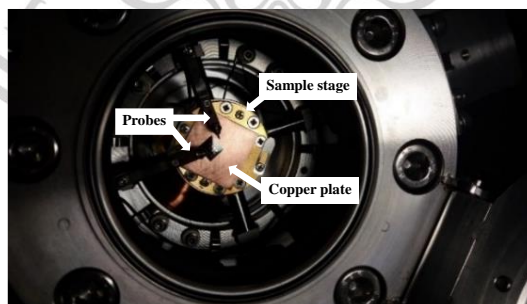


Figure 3.18 Setting the sample inside the chamber.



Figure 3.19 Keithley 2400 Series Source Measure Unit Instrument.



Figure 3.20 Agilent E4980A Precision LCR Meter.

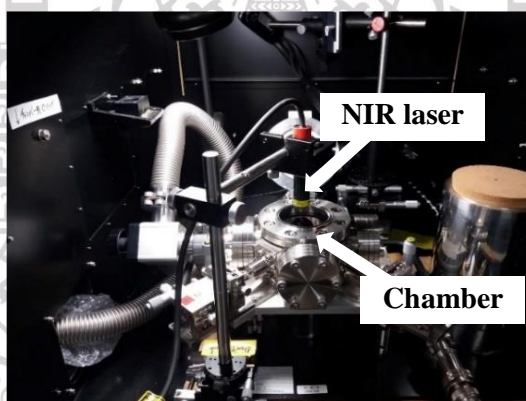


Figure 3.21 Setup of laser for NIR radiation.

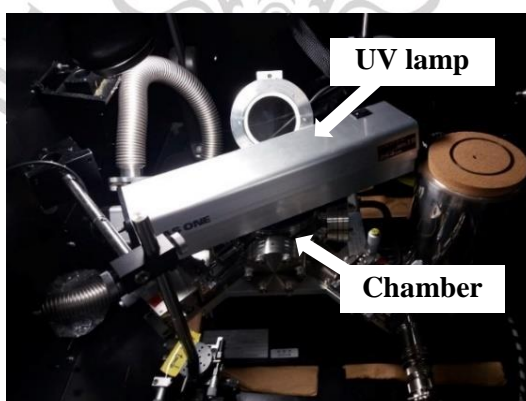


Figure 3.22 Setup of lamp for UV radiation.

This material is reserved for educational use only, not allowed for commercial use.

Forbidden to modify the content, and cite the document when use.

3.5.1 Electrical measurements for p-Si/n- β -FeSi₂ devices formed by FTS

The I - V measurement was performed under darkness and NIR irradiation at room temperature. The dark and irradiated I - V curves were examined to confirm the rectifying behavior and the NIR response at room temperature. Both dark and irradiated I - V data were biased in a voltage range between -3 V and 1 V. The dark I - V curve was recorded under the darkness. The NIR response was inspected under the irradiation of a 6-mW, 1.31- μ m laser light (Neoark, TC20).

The G - V and C - V inspections were manipulated as a function of frequency between 5 kHz and 1 MHz under biased voltages from -5 V to 5 V at room temperature.

3.5.2 Electrical examinations for p-UNCD/n-Si devices created by PLD

The I - V measurement was operated under dark and irradiation conditions with UV light at room temperature. The dark and irradiated I - V curves were investigated to verify the rectifying behavior and the UV response at room temperature. The irradiation condition was managed using a UV light with a 254-nm wavelength. The UV light was illuminated by an AS ONE Handy UV Lamp (SLUV-6) with a spectral radiant intensity of 2020 μ W cm⁻². The applied voltage range was between -5 V and 5 V.

The G - V and C - V examinations were carried out at room temperature under various frequencies between 40 kHz and 2 MHz. The voltage range for G - V and C - V examinations was between -5 V and 5 V.

3.5.2 Electrical inspections for p-UNCD/n-Si devices fabricated by CAPD

The dark and irradiated I - V curves were investigated to verify the rectifying behavior and the UV response at different temperatures in a range of 150 K - 300 K. A voltage range for I - V collection was between -3 V and 3 V. The UV response was conducted under UV irradiation of AS ONE Handy UV Lamp (SLUV-6) with a 254-nm wavelength and a spectral radiant intensity of 2020 μ W cm⁻². Low-temperature condition was executed by liquid N₂, and the temperature was controlled using a 335 Cryogenic Temperature Controller.

The impedance spectroscopy of p-UNCD/n-Si devices formed by CAPD was examined at different voltages ranging from 0 V to 0.5 V. The Z' - Z'' data for the manufactured p-UNCD/n-Si devices was collected at room temperature in the dark with an applied frequency range between 20 Hz and 2 MHz.

3.6 Assessment of significant parameters

Parameter estimation for the p-Si/n- β -FeSi₂ devices was listed as follows:

- 1) The R_s and N_{ss} values were estimated using Nicollian-Brews and Hill-Coleman approaches based on the measured C-V and G-V data at different frequencies.

Parameter extraction of the p-UNCD/n-Si devices built by PLD was listed below:

- 1) The R_s and N_{ss} estimations for the p-UNCD/n-Si devices built by PLD were managed by Nicollian-Brews and Hill-Coleman approaches using the measured C-V and G-V characteristics under various frequencies.

List of parameters for the p-UNCD/n-Si devices built by CAPD was shown below:

- 1) The diode parameters such as η , ϕ_b and E_a were computed with TE theory by the usage of dark I-V curves at different temperatures.
- 2) The diode parameters such as ϕ_b and R_s were estimated based on Norde method using the dark I-V characteristics under various temperatures.
- 3) The dynamic resistance and the UV detectivity were assessed based on the dark and irradiated I-V data under various temperatures.
- 4) The equivalent circuit model corresponding to the heterojunction behavior was anticipated.

Chapter 4

Results and discussion

The results and discussion in this chapter were classified by 3 topics as follows:

1. Results of the p-Si/n- β -FeSi₂ devices formed via FTS consisting of XRD pattern, surface image, cross section, dark and irradiated J - V at room temperature, C - V and G - V profiles under various frequencies, and estimation of N_{ss} and R_s values.
2. Results of p-UNCD/n-Si devices built via PLD comprising Raman spectra, surface morphology, cross section, dark and irradiated J - V at room temperature, C - V and G - V profiles at different frequencies, and extraction of N_{ss} and R_s .
3. Results of p-UNCD/n-Si devices manufactured by CAPD consisting of Raman lines, surface photograph, cross-sectional image, the dark J - V curves and significant diode parameters under various temperatures, dark and irradiated J - V profiles at different temperatures, the UV detection at different temperatures, and the Z'' - Z' profiles under various voltages at room temperature.

4.1 Results of the p-Si/n- β -FeSi₂ devices formed via FTS

4.1.1 Structural properties

Figure 4.1 demonstrates the XRD trace in the 2θ - θ scanning mode of the β -FeSi₂ films coated on Si(111) wafer substrates. From the occurrence in the 2θ - θ XRD spectrum, two diffraction peaks of the (202),(220), and (404),(440) atomic planes of β -FeSi₂ appear to be intense at 29.15 degrees and weak at 61.43 degrees, respectively. The ensuing zeniths refer to the significant peaks for confirmation of the manufacturing of the epitaxial β -FeSi₂ films on Si wafers in (111) orientation [79]. In addition, another peak situated at 28.46 degrees is indicative of the (111) orientation of Si wafer substrates [79].

The inserted image in Figure 4.1 discloses the XRD trace in the 2θ scan with an incidence angle of 4°. This inserted image exhibits no peaks, which revealed no β phase diffraction peaks in 2θ -scan. This outcome exposes that the epitaxial β -FeSi₂ films coated on Si(111) wafers didn't exhibit the polycrystalline structure [79,83]. If the XRD trace in 2θ -scan demonstrates the β phase diffraction peaks, the manufactured β -FeSi₂ films contained the polycrystalline structure [84].

Figure 4.2 exposes the pole figure of the β -440/404 peak for the β -FeSi₂ films. This outcome demonstrates the existence of three types of epitaxial variants rotated at an angle of 120° with respect to each other.

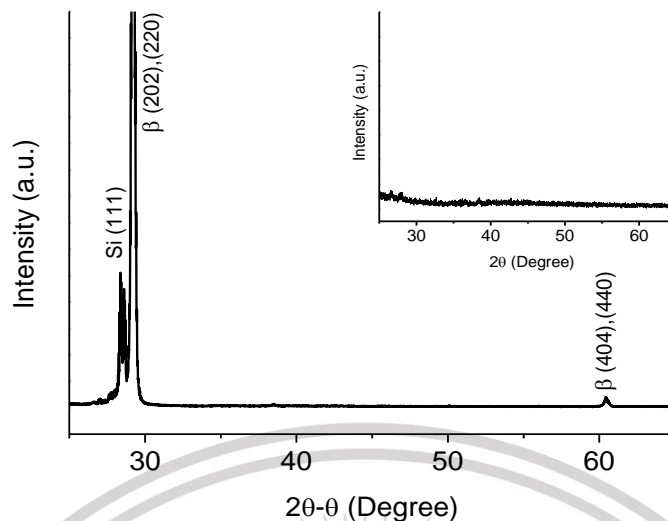


Figure 4.1 XRD trace in the 2θ - θ scan of β -FeSi₂ films manufactured on the Si substrates. The inserted line exhibits the XRD line examined in a 2θ scan.



Figure 4.2 Pole figure characteristic of β -440/404 peak for epitaxial β -FeSi₂ films.

4.1.2 Surface morphology and cross section

FESEM measurement was employed to provide morphological and cross-sectional views of the coated β -FeSi₂ films. In Figure 4.3 (a), the surface of the coated β -FeSi₂ films is presented with 100 kx of magnification. From observation, the surface of the β -FeSi₂ films appears to have numerous grain boundaries with some porosity at the edges of the boundary. The occurrence of grain boundaries over the surface of the coated β -FeSi₂ films might cause behavior as a trap zone when the charge carriers are excited by light radiation [79]. As a result, performance for detecting NIR light of the coated β -FeSi₂ films could be diminished from the occurrence of grain boundaries above the surface [79]. From the evaluation in Figure 4.3 (b), the appraised thickness for the β -FeSi₂ films was around 300 nm. Besides, the observation of a linear shape line between the β -FeSi₂ films and Si wafer without deformation of the junction was visible.

This material is reserved for educational use only, not allowed for commercial use.

Forbidden to modify the content, and cite the document when use.

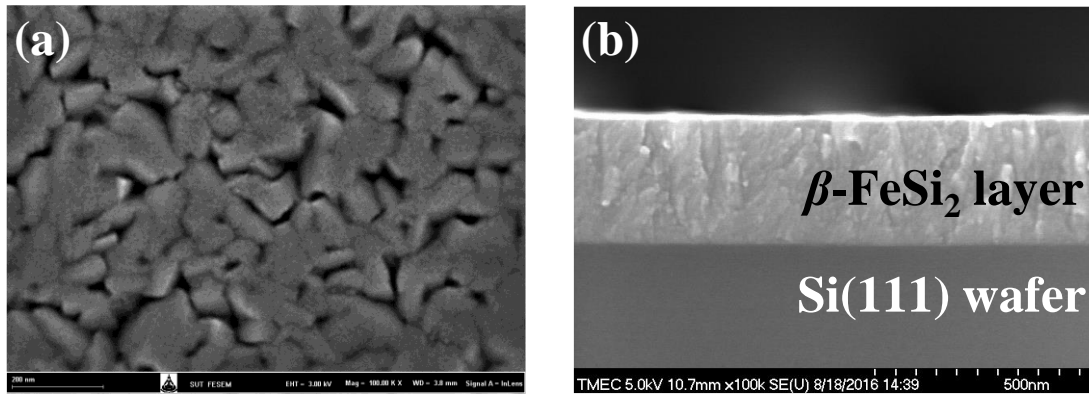


Figure 4.3 FESEM photographs of (a) top and (b) cross-section views for the β -FeSi₂ film coated on Si substrate.

4.1.3 Dark and irradiated J - V profiles at room temperature

Figure 4.4 exhibits a semi-log plot of the J - V curve for the p-Si/n- β -FeSi₂ devices inspected under the condition of darkness and irradiation with a 1.31- μ m laser at a power of 6 mW. A voltage range for biasing the heterojunction devices was between -3 V and 1 V. The device area is around 0.1 cm². From the measured dark J - V curve, the manufactured heterojunctions disclosed a good rectification proportion corresponding to the ordinary behavior of the p-n junction. The rectifying action ratio between the biased voltages of -3 V and 1 V was up to two orders of magnitude. The built p-Si/n- β -FeSi₂ devices expose the leakage current at -1 V of around 10⁻⁶ A, which was higher than that of photodiodes comprising InAs around two orders of magnitude [85]. Further, the response to NIR irradiation of the created p-Si/n- β -FeSi₂ devices was relatively small. These outcomes might originate in the diffusion of Fe atoms from the β -FeSi₂ film layer to the Si layer during the film construction, including the interface states appearing at the hetero-interface area [16,17,86]. These causes would perform as the leakage current origin in addition to the center of trapping the carriers created via light [16,17,86]. The inserted graph in Figure 4.4 exposes the photocurrent characteristics plotted with voltage, which the photocurrent was deducted from the dark current. The value of subtracted current was 2.0 \times 10⁻⁵ A cm⁻² at 0 V. After the voltage was biased to -3 V, the subtracted current rose to the highest value of 3.9 \times 10⁻⁵ A cm⁻².

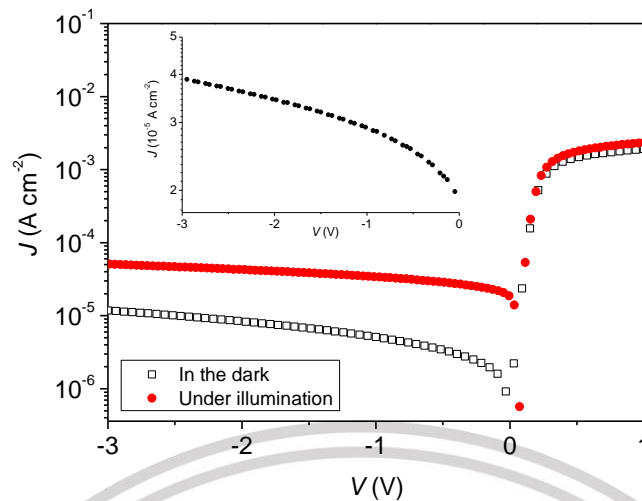


Figure 4.4 Dark and irradiated J - V curves of the p-Si/n- β -FeSi₂ devices inspected at room temperature. The inserted image exhibits the photocurrent deduced from the dark current.

4.1.4 C - V and G/ω - V profiles as a function of frequency

The experimental C - V and G/ω - V results of p-Si/n- β -FeSi₂ diodes inspected at room temperature under various frequencies are exposed in Figure 4.5 (a) and (b), respectively. A biased frequency range was between 5 kHz and 1 MHz. Based on the C - V - f and G/ω - V - f profiles, three regimes comprising inversion, depletion, and accumulation were noticed in the voltage bias range between -5 V and 5 V [87]. As the rise in bias voltage, the C value is augmented until it reaches into an accumulation regime [88,89]. In this case, the strong accumulation at higher bias voltage is about 5 V [89,90]. As indicated in Figure 4.5, the C and G/ω values can be changed by both voltage and frequency, which the change of the C and G/ω can be especially found in the depletion and accumulation regimes. Nevertheless, the trend of C and G/ω in the inversion regime was invariant [87]. With the rise in positive bias, the C value augments until it enters to an accumulation steady state. The increase of C value can be observable in lower frequencies. The C value at low frequencies relies on the total of the interface and space charge C values, which the contribution of the interface C value to the device C values will subside as rising frequency [87]. Each C - V profile provides a peak, which might originate in the molecular restructuring and reordering of N_{ss} and R_s [89]. The peak intensities of the C - V and G/ω - V curves subside with the increment in frequency. This exposes that the interface states can follow an AC signal [91]. Furthermore, the peak situations of C - V and G/ω - V profiles move to higher bias values when the frequency was increased to higher values.

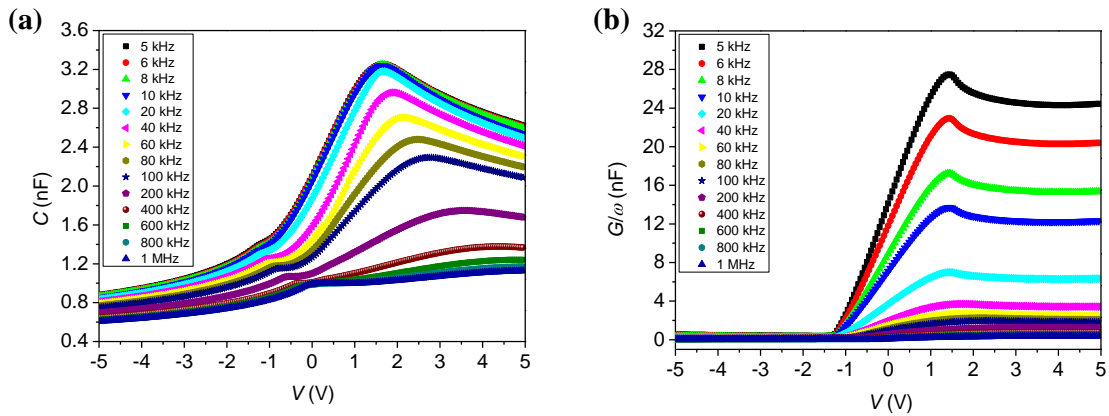


Figure 4.5 (a) C - V and (b) G/ω - V profiles under various frequencies of p-Si/n- β -FeSi₂ devices manufactured by FTS.

4.1.5 Computation and study of R_s and N_{ss} characteristics

For the R_s determination, the devices were biased into a strong accumulation regime with adequate frequency for collecting the C - V and G/ω - V data. The evaluation of R_s was manipulated by Nicollian-Brews approach, which was indicated below:

$$R_s = \frac{G_{ma}}{(C_{ma} \omega)^2 + (G_{ma})^2}$$

Where ω denotes the angular frequency while G_{ma} and C_{ma} are the conductance and the capacitance acquired in the strong accumulation region, respectively.

The appraised R_s of p-Si/n- β -FeSi₂ heterojunction devices was plotted with voltage under various frequencies ranging from 5 kHz to 1 MHz, as exhibited in Figure 4.6. The R_s values are invariant in the regimes of inversion and accumulation. In the range of frequency ≤ 100 kHz, the R_s variation unveils a peak in the depletion region, which was in a voltage range between -1 V and 1 V. However, the R_s variation at frequencies over 100 kHz was rarely appeared. Also, the R_s peak magnitude was observed to be subsided with the rise in frequency. This outcome exposes that the effect of interface states was remarkable only at lower frequencies [88,91]. The shift of apex position to higher forward bias values occurred when the frequency was augmented to higher values. This result might originate in a special density distribution of N_{ss} at the heterojunction between p-Si and n- β -FeSi₂ in addition to reordering and restructuring under applied bias influence at various frequencies [88,91]. The change of R_s value to applied voltage was almost invisible at frequencies over 100 kHz. This result reveals that the interface charges possess adequate energy for the getaway from the trap levels [65]. Furthermore, the charges at the interface states could not follow the AC signal at high frequencies [61].

This material is reserved for educational use only, not allowed for commercial use.

Forbidden to modify the content, and cite the document when use.

The R_s - f profile at 0 V for the p-Si/n- β -FeSi₂ devices created by FTS is exhibited in Figure 4.7. At zero bias, the R_s value was 2.21 k Ω at 5 kHz, and it declined to be 13.66 Ω at 1 MHz. R_s appearing in the p-Si/n- β -FeSi₂ heterojunction devices might occur from the diffused Fe atoms onto the Si side during the manufacturing process, which would engender the formation of deep trap levels in the depletion zone and also create the leakage current [17,82]. Furthermore, the deep-trap levels that trapped the photo-created carriers beget the obstacle of light detection [17,82].

Moreover, the R_s values at 0 V of p-Si/n- β -FeSi₂ devices created by FTS were around 174 Ω cm² at 20 kHz and decreased to 1.37 Ω cm² at 1 MHz, which this trend of R_s values was consistent with those from p-Si/n- β -FeSi₂ devices created by RFMS. The R_s values at 0 V of p-Si/n- β -FeSi₂ devices produced by RFMS were around 77.79 Ω cm² and 14.16 Ω cm² at 20 kHz and 1 MHz, respectively [92].

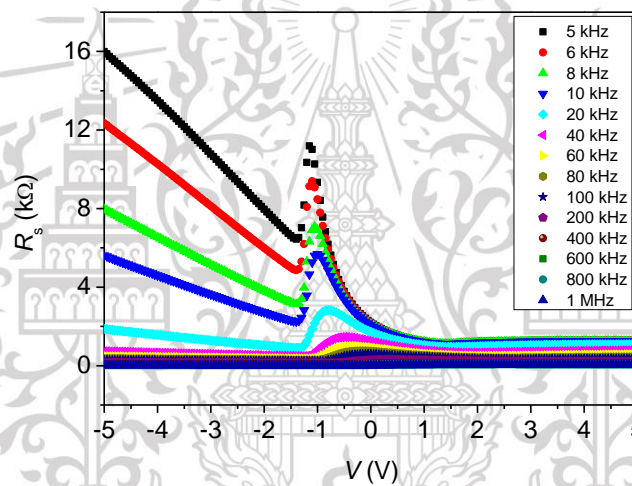


Figure 4.6 R_s - V profiles at different frequencies for the p-Si/n- β -FeSi₂ devices.

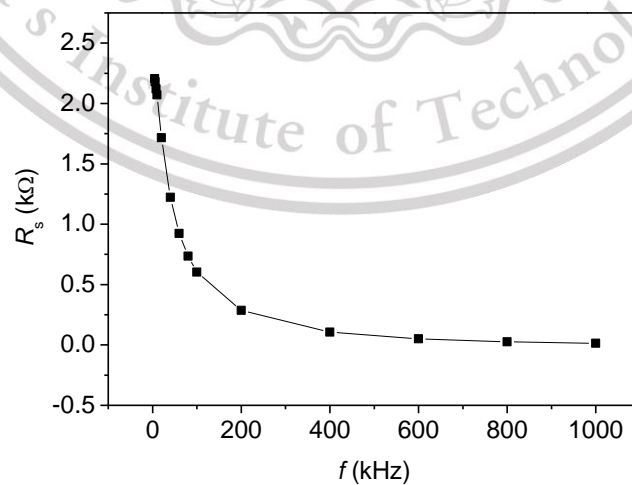


Figure 4.7 R_s - f relationship at zero bias for p-Si/n- β -FeSi₂ heterojunctions.

This material is reserved for educational use only, not allowed for commercial use.

Forbidden to modify the content, and cite the document when use.

The existing N_{ss} in the devices is a chief reason that deteriorates the performance of the device. The extraction of N_{ss} was managed using the measured $C-V$ and $G/\omega-V$ data by the Hill-Coleman method, which is specified below:

$$N_{ss} = \left(\frac{(G_m/\omega)_{\max}}{\left(\left((G_m/\omega)_{\max}/C_{ox} \right)^2 + \left(1 - (C_m/C_{ox}) \right)^2 \right)} \right) \left(\frac{2}{qA} \right)$$

where $(G_m/\omega)_{\max}$ demonstrates the maximum G_m/ω value, and C_m depicts the capacitance relating to the value of $(G_m/\omega)_{\max}$. A specifies the device area, which the p-Si/n- β -FeSi₂ heterojunctions have the device area around 0.1 cm². C_{ox} for the p-Si/n- β -FeSi₂ heterojunction devices was assumed that was a thin intrinsic layer of β -FeSi₂ existing between p-Si and n- β -FeSi₂. The appraisal of C_{ox} value can be manipulated using the $C-V$ and $G/\omega-V$ information in the strong accumulation regime via the relationship, which is identified below:

$$C_{ox} = \left(\frac{(G_{ma})^2}{(C_{ma}\omega)^2} + 1 \right) C_{ma}$$

Figure 4.8 discloses the N_{ss} - f variation for the p-Si/n- β -FeSi₂ heterojunctions at different frequencies under room temperature. The acquired N_{ss} rose exponentially as the subsidence of frequency. In low frequencies (≤ 100 kHz), the N_{ss} value relied on frequency, engendering the increased C value in the p-Si/n- β -FeSi₂ heterojunction devices. At high frequencies over 100 kHz, the resultant N_{ss} not relied on the frequency. The high capacitances at low frequencies might originate from the excessive C value occurring from N_{ss} , which was in an equilibrium state with the semiconductor and can follow the AC signal [65,93,94]. In contrast, the interface states in equilibrium with the semiconductor do not contribute to the C value at high frequencies. Also, the charge at the interface states cannot follow the AC signal [65,93,94]. The appraised parameters for p-Si/n- β -FeSi₂ heterojunctions created by FTS are demonstrated in Table 4.1. The appraised N_{ss} values were estimated to be 4.68×10^{11} eV⁻¹ cm⁻² at 1 MHz and 3.48×10^{12} eV⁻¹ cm⁻² at 5 kHz. The obtained N_{ss} values were consistent with those of p-Si/n- β -FeSi₂ heterojunctions produced by evaporation with post-annealing, which owned the N_{ss} values in a range of 10^{10} eV⁻¹ cm⁻² to 10^{12} eV⁻¹ cm⁻² [95]. The N_{ss} outcome discloses that interface states appeared at the hetero-interface area of the manufactured p-Si/n- β -FeSi₂ heterojunction device. The existing N_{ss} serves as the leakage current sources and the hubs for trapping the carriers created by light. This result engenders the degradation of the device performance [17,96].

This material is reserved for educational use only, not allowed for commercial use.

surface photograph of β -FeSi₂ films, the high-density gaps of crystalline domains were observed. Thus, the error of N_{ss} estimation could originate in the existence of gaps, which can engender the non-contact zone between β -FeSi₂ layer and Al electrode. Due to the non-contact zone, the real contact zone might be less than the nominal geometric zone [97]. Thus, the N_{ss} value assessed by the nominal geometric area of 0.1 cm² might be slightly less than that computed by the real contact area.

Table 4.1 Parameters of the p-Si/n- β -FeSi₂ devices defined using C - V and G/ω - V data at different frequencies.

f (kHz)	V_m (V)	$(G_m/\omega)_{max}$ (F)	C_m (F)	N_{ss} (eV ⁻¹ cm ⁻²)	R_s (at V_m) (Ω)
5	1.45	2.75×10^{-8}	3.22×10^{-9}	3.48×10^{12}	1142.35
6	1.45	2.29×10^{-8}	3.22×10^{-9}	2.92×10^{12}	1134.29
8	1.45	1.72×10^{-8}	3.21×10^{-9}	2.23×10^{12}	1114.79
10	1.45	1.37×10^{-8}	3.21×10^{-9}	1.80×10^{12}	1101.34
20	1.45	6.99×10^{-9}	3.12×10^{-9}	1.05×10^{12}	949.34
40	1.70	3.70×10^{-9}	2.94×10^{-9}	7.54×10^{11}	659.23
60	1.95	2.72×10^{-9}	2.68×10^{-9}	6.69×10^{11}	494.98
80	2.20	2.25×10^{-9}	2.45×10^{-9}	6.15×10^{11}	403.85
100	2.40	1.95×10^{-9}	2.26×10^{-9}	5.72×10^{11}	347.60
200	3.20	1.25×10^{-9}	1.73×10^{-9}	4.56×10^{11}	217.98
400	3.95	7.57×10^{-10}	1.37×10^{-9}	4.04×10^{11}	122.92
600	4.10	5.52×10^{-10}	1.23×10^{-9}	4.11×10^{11}	80.66
800	4.15	4.40×10^{-10}	1.16×10^{-9}	4.35×10^{11}	57.14
1,000	4.15	3.66×10^{-10}	1.11×10^{-9}	4.68×10^{11}	42.46

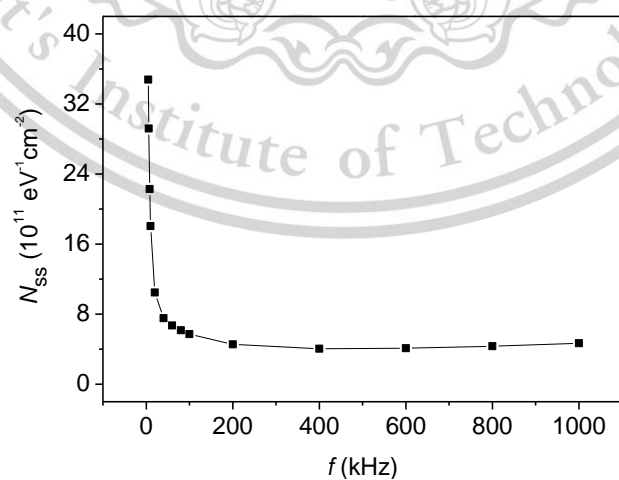


Figure 4.8 N_{ss} - f curve at room temperature for p-Si/n- β -FeSi₂ heterojunctions.

4.2 Results of the p-UNCD/n-Si devices constructed via PLD

4.2.1 Raman patterns

Figure 4.9 manifests the Raman spectra of undoped and 0.1 at.% B-doped UNCD/a-C:H films formed by PLD. Both Raman lines display two prominent broad peaks and a shoulder position. Two broad peaks around 1339 cm^{-1} and 1565 cm^{-1} tallied with D- and G-modes due to the disorder of amorphous carbon [98,99]. A shoulder position about 1160 cm^{-1} rose from either the UNCD or the existing tran-polyacetylene in the grain boundaries [98,99]. Raman line of B-doped UNCD/a-C:H films unveils the slight weakening in the intensity and broadening in the D and G peaks compared with that of the UNCD/a-C:H films [100,101]. This result shows a slightly weak bonding of the graphitic phase, which may originate in the doped boron atoms in the UNCD/a-C:H films disturbing the vibration of the a-C:H matrix. Also, the Raman peaks of undoped and B-doped UNCD/a-C:H films were centered at the same position. This showed that a small amount of boron doping did not affect the Raman shift.

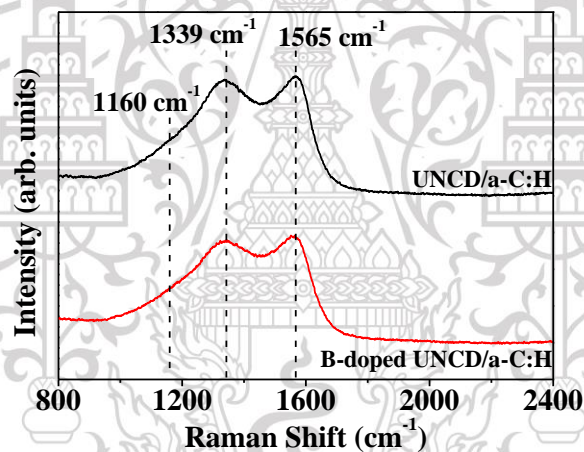


Figure 4.9 Raman lines for undoped and B-doped UNCD/a-C:H films created by PLD.

4.2.2 Surface and cross-sectional images

The surface image with 200,000x magnification and cross section with 50,000x magnification of the B-doped UNCD/a-C:H films coated on the Si substrates via PLD is displayed in Figure 4.10 (a) and (b), respectively. The surface image exposed the smoothness of the fabricated B-doped UNCD/a-C:H films without film cracking. The films also consisted of many B-doped UNCD grains (less than 10 nm) embedded in an a-C:H matrix. The cross-sectional photograph of the B-doped UNCD/a-C:H layer produced on Si wafer via PLD exhibited the uniformity of film layer without cracking or voids. Further, the interface between the layers of B-doped UNCD/a-C:H and Si was noticeable.

This material is reserved for educational use only, not allowed for commercial use.

Forbidden to modify the content, and cite the document when use.

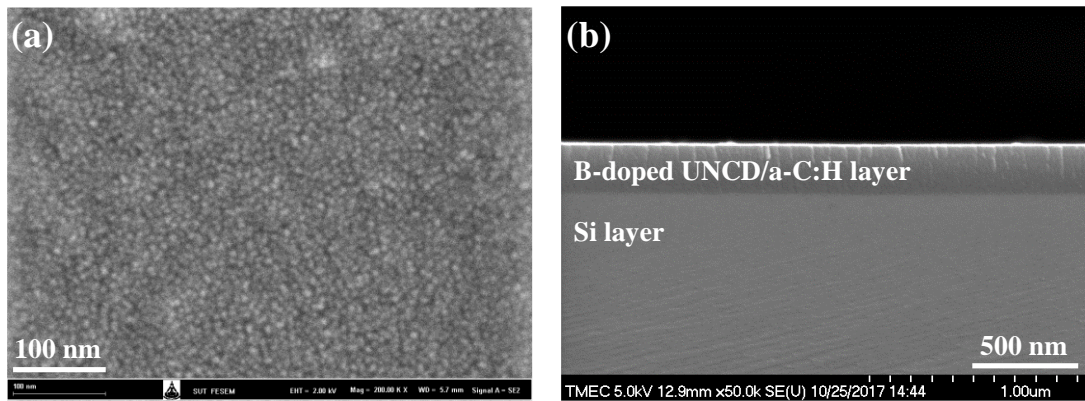


Figure 4.10 (a) Morphological and (b) cross-sectional images of the B-doped UNCD/a-C:H layer produced on Si wafer by PLD.

4.2.3 Dark and irradiated J - V profiles at room temperature

Figure 4.11 illustrates the J - V profiles of the p-UNCD/n-Si devices formed by PLD. The J - V data were recorded in a voltage range from -5 V to 5 V at room temperature in the dark and radiation of 254 nm and 2020 $\mu\text{W}/\text{cm}^2$ light. The J - V profiles exposed a rectifying behavior conforming to the normal p-n abrupt diodes. The rectification ratio of the created devices between -5 V and 5 V was around four orders of magnitude. The leakage current at -5 V of the p-UNCD/n-Si devices formed by PLD was 3.02×10^{-5} A cm^{-2} . This leakage current value was larger than that of the existing SiC photodiodes about five orders of magnitude [102]. A large leakage current and a small response to UV light might possibly be due to the interface states at the hetero-interface serving as a source of leakage current as well as a trap center of the photo-created carrier [21,96].

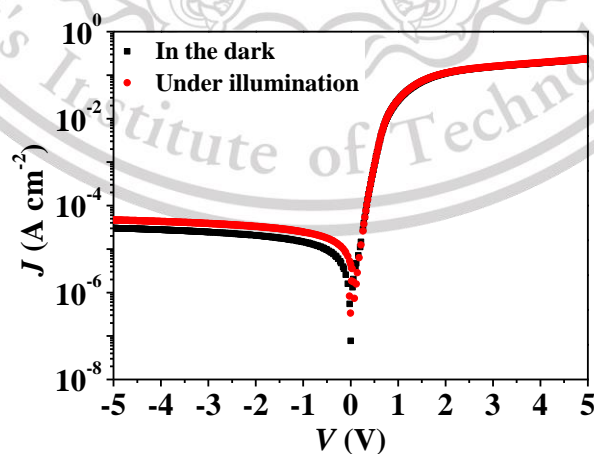


Figure 4.11 Dark and irradiated J - V profiles at room temperature for the p-UNCD/n-Si devices constructed by PLD.

This material is reserved for educational use only, not allowed for commercial use.

Forbidden to modify the content, and cite the document when use.

4.2.4 C-V and G/ω -V investigations under various frequencies

Figure 4.12 (a) and (b) depicts the C-V and G/ω -V profiles at various frequencies for the p-UNCD/n-Si devices built via PLD. These curves were measured in a voltage range between -5 V and 5 V, under the frequency variation ranging from 2 MHz to 40 kHz at room temperature. The frequency-dependent C-V and G/ω -V profiles exposed three areas of inversion, depletion, and accumulation [87]. The measured C and G/ω hinge on the voltage and frequency. C and G/ω barely varied in the inversion area, but they obviously changed in the depletion and accumulation areas [87]. By increasing voltage, the C value rose until it reached to an accumulation steady state [88,89]. The increment of C was found at lower frequencies. The C value conformed to the total of the interface and space charge C at low frequencies. Reinforcement of interface C to device C diminished when the frequency was biased to higher values [87]. For each frequency, the C-V profile provided a peak attributable to the reordering of N_{ss} and R_s , including the restructuring of molecules [89]. The C-V and G/ω -V peaks were diminished by reducing frequency. This confirms that the interface states can follow a signal of AC [91].

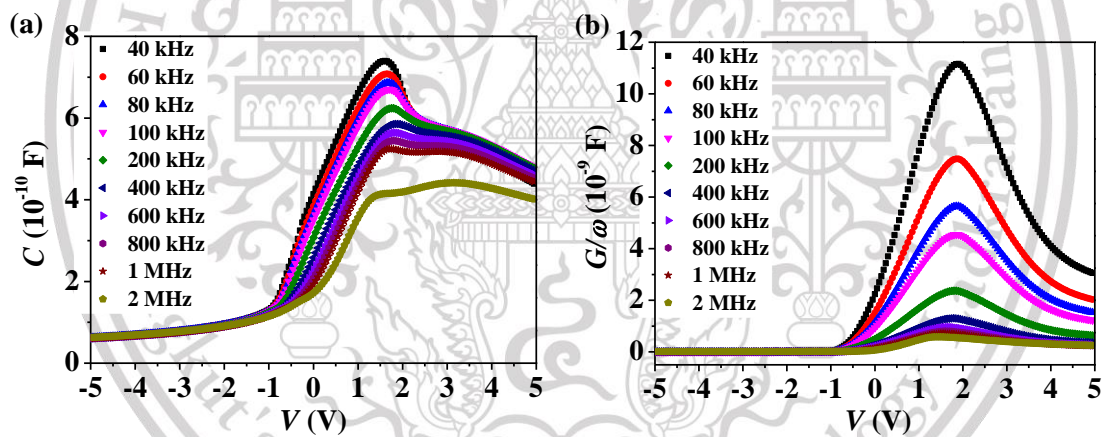


Figure 4.12 (a) C-V and (b) G/ω -V curves at different frequencies for the p-UNCD/n-Si devices manufactured via PLD.

4.2.5 Estimation and investigation of R_s and N_{ss} profiles

Figure 4.13 reveals the R_s curves plotted with voltage at various frequencies of the p-UNCD/n-Si devices produced via PLD. The R_s values were assessed by Nicollian-Brews approach. In the areas of inversion and accumulation, the observed R_s values were varied slightly. Each R_s -V profile indicated a peak, and the peak height of R_s diminished when the frequency was elevated. This indicated that the interface states were influential at low frequencies [88,91]. Also, the peak position shifted slightly to a higher forward voltage when frequency increased because of the especially dense. This material is reserved for educational use only, not allowed for commercial use.

Forbidden to modify the content, and cite the document when use.

distribution of interface states at the heterojunction interfaces, including reordering and restructuring under applied bias effect at various frequencies [88,91]. At sufficiently high frequencies, the R_s profiles under positive and negative bias are virtually unchanged. This intimates that the interface charges hold adequately high energy to flee from the trap levels [65]. Likewise, the charges at the interface states could not follow the signal of AC at high frequencies [61,103]. R_s values at zero bias were found to be $1.72 \text{ k}\Omega$ and $154.41 \text{ }\Omega$ at 40 kHz and 2 MHz in sequence. The presence of R_s in the heterojunctions may be attributable to the R_s of the junctions occurring in the neutral areas along with the metallic contact [18,68]. It is the current-limiting factor for the built heterojunction photodiodes in the current work [18,68]. Further, the R_s values at frequencies higher than 800 kHz conformed to R_s computed by Norde model [104].

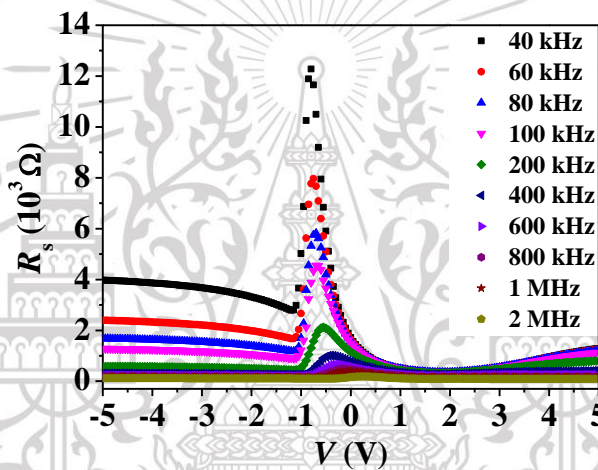


Figure 4.13 R_s - V plots for the p-UNCD/n-Si devices manufactured by PLD at different frequencies between 40 kHz and 2 MHz.

Table 4.2 shows the assorted variables for the p-UNCD/n-Si diodes formed by PLD, which were defined from the C - V and G/ω - V profiles at various frequencies. The acquired N_{ss} values for the built heterojunction diodes were assessed through Hill-Coleman and plotted as a function of frequency, as revealed in Figure 4.14. N_{ss} at low frequencies ($\leq 200 \text{ kHz}$) hinged strongly on the frequency value due to the rising of C in the built heterojunction photodiodes. At high frequencies ($> 200 \text{ kHz}$), N_{ss} disclosed the independence of frequency value. The high C at the frequency $\leq 200 \text{ kHz}$ can be ascribed to the excess C arising from N_{ss} in equilibrium with the semiconducting material. This indicated that N_{ss} can follow the signal of AC at low frequencies [65,93,94]. Furthermore, the interface states in equilibrium with the semiconducting material at a sufficient frequency do not conduce the contribution of C . Additionally, the charge at the interface states, in the case of frequency above 200 kHz, cannot follow the signal of AC [65,93,94]. The N_{ss} values were assessed to be $1.39 \times 10^{12} \text{ eV}^{-1}$.

cm^{-2} and $1.78 \times 10^{13} \text{ eV}^{-1} \text{ cm}^{-2}$ at 2 MHz and 40 kHz in sequence. The acquired result revealed the existence of interface states at the heterojunction interface. The interface states could serve as a leakage current source and trap hubs for photo-created carriers, leading to deterioration in the performance of the built heterojunction diodes [96].

These obtained N_{ss} values were also consistent with that of the heterojunction comprising Si and UNCD/a-C:H created by CAPD, which possessed N_{ss} value around $3 \times 10^{13} \text{ cm}^{-2} \text{ eV}^{-1}$ [105].

Table 4.2 Parameter values assessed from the C - V and G/ω - V curves at different frequencies of the p-UNCD/n-Si diodes formed by PLD.

f (kHz)	V_m (V)	$(G_m/\omega)_{\max}$ (F)	C_m (F)	N_{ss} ($\text{eV}^{-1} \text{ cm}^{-2}$)	R_s (at V_m) (Ω)
40	1.90	1.12×10^{-8}	7.00×10^{-10}	1.78×10^{13}	355.18
60	1.85	7.48×10^{-9}	6.93×10^{-10}	1.20×10^{13}	351.72
80	1.85	5.65×10^{-9}	6.76×10^{-10}	9.11×10^{12}	347.17
100	1.85	4.55×10^{-9}	6.63×10^{-10}	7.39×10^{12}	342.50
200	1.80	2.37×10^{-9}	6.24×10^{-10}	4.03×10^{12}	314.11
400	1.75	1.30×10^{-9}	5.84×10^{-10}	2.48×10^{12}	254.89
600	1.65	9.58×10^{-10}	5.57×10^{-10}	2.04×10^{12}	206.83
800	1.60	7.54×10^{-10}	5.29×10^{-10}	1.85×10^{12}	171.25
1,000	1.55	7.17×10^{-10}	5.17×10^{-10}	1.73×10^{12}	146.03
2,000	1.45	5.77×10^{-10}	4.12×10^{-10}	1.39×10^{12}	91.32

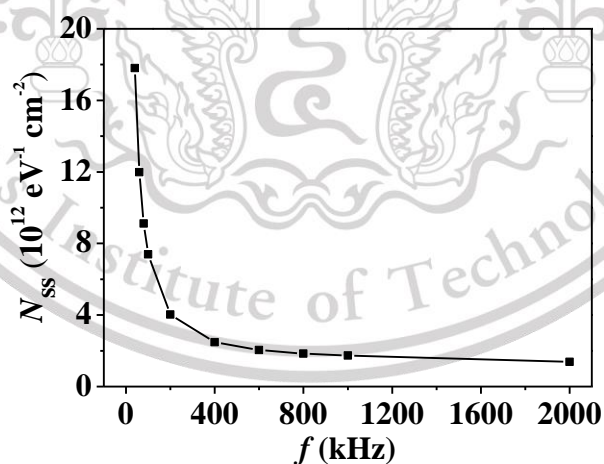


Figure 4.14 N_{ss} profile at various frequencies for p-UNCD/n-Si devices formed by PLD.

4.3 Results of the p-UNCD/n-Si devices manufactured via CAPD

4.3.1 Raman spectra

The measured Raman spectra of the pure and B-doped UNCD/a-C:H films are exposed in Figure 4.15. Both Raman profiles of the pure and B-doped UNCD/a-C:H films exposed two prominent broad peaks that the peak centers were located about 1345 cm^{-1} and 1585 cm^{-1} . A Raman peak centered around 1345 cm^{-1} related to a typical profile for diamond bonded of the coated films. This position shifted from 1333 cm^{-1} position of bulk diamond to 1345 cm^{-1} due to scattering in the nanosized grains [106,107]. A Raman peak with strong intensity at 1585 cm^{-1} can be determined as the G band of amorphous carbon matrices, which stemmed from the stretching bond of the carbon atoms in the sp^2 hybridization [106,107]. Further, Raman peaks for the pure and B-doped UNCD/a-C:H films were situated at the same position. This consequence might ascribe to the B element that was doped with low quantity [100,101]. However, Raman peaks of the B-doped UNCD/a-C:H films revealed the intensity decrement and peak expansion. The decrease in peak intensity might be relative to the subsidence of the graphitic bonding from the interference of the doped B atoms that affected the vibration process in the a-C:H matrices [100,101].

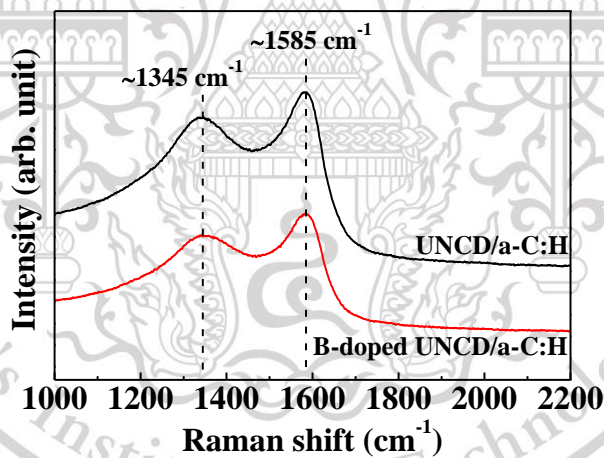


Figure 4.15 Raman profiles of the pure and B-doped UNCD/a-C:H films coated by CAPD.

4.3.2 Surface image and cross-sectional observation

Figure 4.16 (a) and (b) demonstrate the surface photograph and cross section of the B-doped UNCD/a-C:H films coated on the Si substrates via CAPD, respectively. A magnification of the surface image was 100,000 times. The surface morphology of the constructed films exhibits the agglomeration of B-doped UNCD grains. The agglomerated UNCD grains have diameters ranging from 30 nm to 80 nm. Figure 4.16 (b) reveals the cross-sectional observation with 30 kx magnification for the B-doped

This material is reserved for educational use only, not allowed for commercial use.

Forbidden to modify the content, and cite the document when use.

UNCD/a-C:H layer coated on the Si substrate. The cross-sectional photograph unveils the uniformity of B-doped UNCD/a-C:H layer. Between the B-doped UNCD/a-C:H and Si layers, the linear interface was visibly noticed with the nonexistence of film cracking. The thickness of film layer estimated from the cross section was about 750 nm, which the film thickness was also invariable.

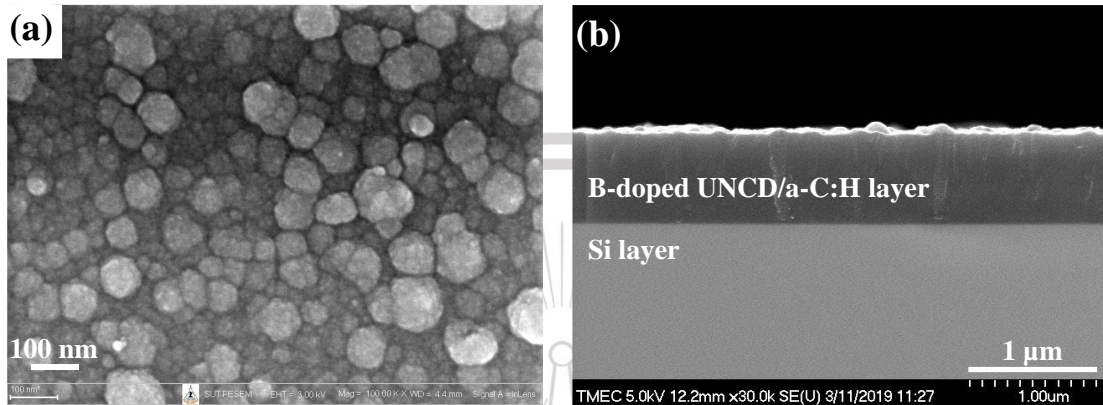


Figure 4.16 Captured FESEM images in (a) top and (b) cross-sectional views of the B-doped UNCD/a-C:H films coated via CAPD.

4.3.3 Dark J - V profiles and diode parameters at different temperatures

Figure 4.17 depicts the dark J - V profile of the p-UNCD/n-Si devices constructed through CAPD, which was tested at different temperatures under negative and positive bias circumstances in range from -3 V to 3 V. The temperature range was between 300 K to 150 K. The manufactured heterojunctions manifest a fine rectifying behavior corresponding to the ordinary p-n abrupt diodes. Under the room-temperature condition, the rectifying action ratio of the manufactured devices between -3 V and 3 V was observed to be over three orders of magnitude. For the p-UNCD/n-Si devices formed by CAPD, the leakage current at -3 V of was found at 5.39×10^{-5} A cm^{-2} , which was larger than that of the existing SiC photodiodes over five orders of magnitude [102]. A large leakage current at room temperature might result from the interface states occurring in the hetero-interface area that act as an origin of the leakage current [80,104]. After the temperature diminished to 150 K, the rectification ratio was enhanced to be over four orders of magnitude. Additionally, the leakage current at 150 K was diminished by over two orders of magnitude in comparison to that of room-temperature condition. The decrease in the leakage current might originate in the diminution of the carriers in the B-doped UNCD/a-C:H layer under the low-temperature condition [80,104].

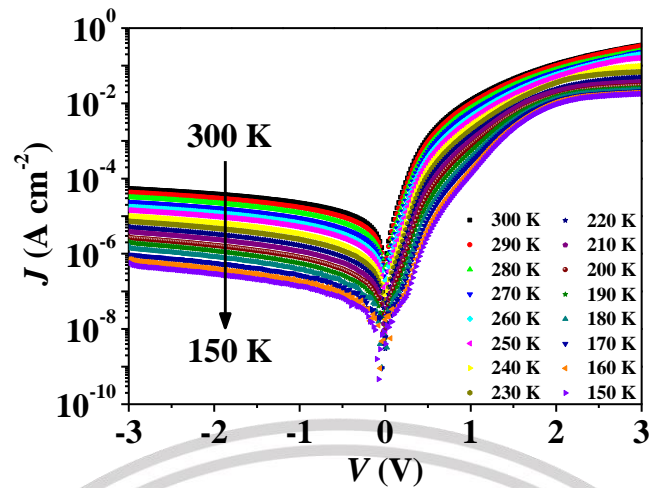


Figure 4.17 Dark J - V curves tested under various temperatures for the p-UNCD/n-Si devices constructed through CAPD.

The diode parameters such as n , ϕ_b , and R_s , including the conduction mechanism, were estimated using the dark J - V data. n and ϕ_b can use to express the carrier transport process and the barrier height at the junction interface of diodes. Based on TE theory, the current density was delineated by the following relation:

$$J = J_0 \left(\exp\left(\frac{qV}{nkT}\right) - 1 \right)$$

where J_0 and n are the saturation current density and ideality factor, respectively.

According to TE theory, in the case of voltage over $3kT/q$, the R_s value in the diodes was assumed to be insignificant. The appraisal of n value was manipulated using the slope in the linear regime of $\ln(J)$ - V plot through the relation indicated below:

$$n = \left(\frac{q}{kT} \right) \left(\frac{dV}{d(\ln J)} \right) = \left(\frac{q}{kT} \right) \left(\frac{1}{\text{slope}} \right)$$

J_0 was defined by drawing the straight-line to y-intercept of $\ln(J)$ - V plot. The assessment of ϕ_b value was managed using the equation expressed as follows:

$$J_0 = A^* T^2 \exp\left(\frac{-q\phi_b}{kT}\right)$$

where A^* and ϕ_b are Richardson's constant and the value of barrier height, respectively. This material is reserved for educational use only, not allowed for commercial use.

Forbidden to modify the content, and cite the document when use.

Figure 4.18 discloses the variation of n and ϕ_b assessed using TE theory for the p-UNCD/n-Si devices formed by CAPD. The left and right sides of y-axis are the n and ϕ_b axis, respectively. The trend of n is shown with black line. At 300 K, the estimated n was found to be 2.82, indicating that heavy recombination with the tunneling process might regulate the carrier transport [82,108]. The heavy recombination can occur at the junction interface and the p-UNCD/a-C:H film side [82,108]. After the temperature was reduced to 150 K, the n value rose to be 6.37, exposing that the carrier transport was dominated by the tunneling mechanism [20,104]. The rise in n value at low temperatures may originate in the imperfections of the contact behavior, the tunneling, including the non-homogeneity of the material barrier [20,104]. The blue line reveals the ϕ_b variation. The ϕ_b values were appraised to be 0.75 eV at 300 K and 0.43 eV at 150 K. Reduction of ϕ_b might occur from the non-uniformity of charge at the junction interface [109,110].

The computed n value at 300 K of p-UNCD/n-Si devices formed by CAPD was close to that of p-UNCD/n-Si devices created by PLD, which has the n value of 2.70 [104]. When the temperature decreased, the n value of both devices showed the increment of n . At 300 K, the ϕ_b value of 0.75 eV for p-UNCD/n-Si devices formed by CAPD was also conformed with that of devices produced by PLD, which owned the ϕ_b value of 0.78 eV [104]. Both devices also revealed the decrement trend of ϕ_b when the temperature diminished.

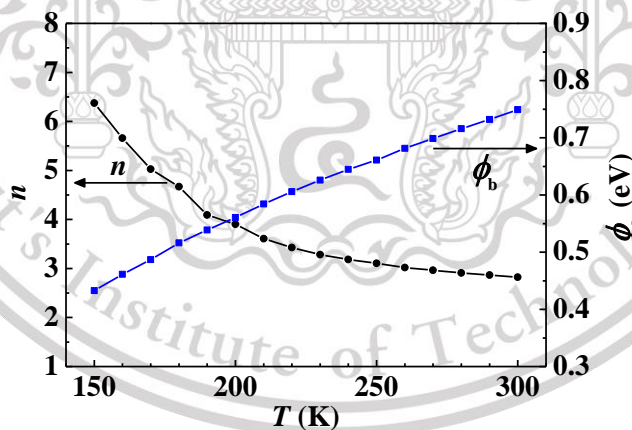


Figure 4.18 Variance of n (black plot) and ϕ_b (blue plot) in the temperature range between 150 K and 300 K.

Based on the J_0 values, E_a can be estimated by the following relation:

$$J_0 \propto \exp\left(\frac{\Delta E_a}{kT}\right)$$

This material is reserved for educational use only, not allowed for commercial use.

Forbidden to modify the content, and cite the document when use.

The logarithm of J_0 plotted versus the inverse of the temperature ($1000/T$) for the the p-UNCD/n-Si devices constructed through CAPD is demonstrated in Figure 4.19. According to the Arrhenius plot, two regimes of E_a value were revealed. For the first regime, the E_a value was around 0.22 eV in the temperature range of 300 K - 190 K. The second regime was observed between 190 K and 150 K, which the estimated E_a value was around 59.62 meV. This outcome can imply that the interface states occur at the hetero-interface area, including the localized states in the B-doped UNCD/a-C:H film layer [111].

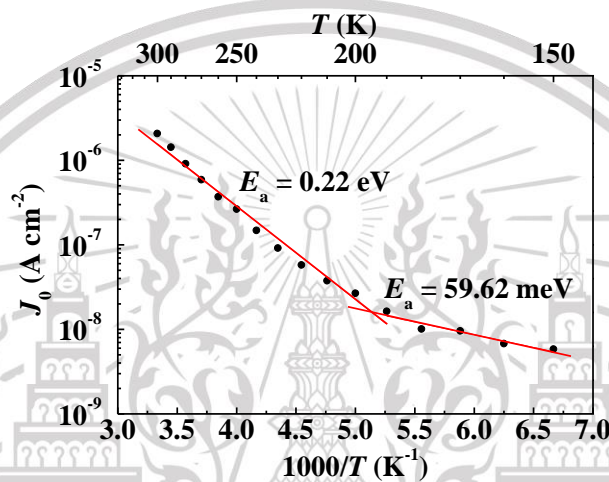


Figure 4.19 Arrhenius plot of J_0 against $1000/T$ for the p-UNCD/n-Si devices manufactured by CAPD.

Based on Norde approach, the ϕ_b and R_s values for the manufactured heterojunction diodes can be executed. Norde's function ($F(V)$) was estimated using the relation as follows:

$$F(V) = \frac{V}{\gamma} - \left(\frac{kT}{q} \right) \ln \left(\frac{J}{T^2 A^*} \right)$$

where V , T , J , and A^* express the bias voltage, temperature, current density, Richardson's constant, respectively. γ denotes the first integer more than the n value, and the n value, in this case, is acquired from TE theory.

The value of ϕ_b and R_s value can be estimated using the data of the minimum point of the $F(V)$ - V plot. The relation for assessment of ϕ_b is expressed below:

$$\phi_b = F(V_0) + \frac{V_0}{\gamma} - \frac{kT}{q}$$

where $F(V_0)$ and V_0 are the minimum point of $F(V)$ and the voltage corresponding to the $F(V_0)$ value, respectively. The R_s estimation was operated by the relation demonstrated as follows:

$$R_s = \frac{kT}{qAJ_{\min}}(\gamma - n)$$

where J_{\min} is the current density, which corresponded to the $F(V_0)$ value.

Figure 4.20 exhibits the $F(V)$ - V profiles of the p-UNCD/n-Si devices constructed through CAPD in which black and blue dots were at 300 K and 150 K, respectively. The ϕ_b values appraised by Norde approach were 0.80 eV at 300 K and 0.48 eV at 150 K, which these acquired ϕ_b values conformed to those evaluated by TE theory. Figure 4.21 illustrates the R_s profile plotted with temperature for the p-UNCD/n-Si devices produced by CAPD. The R_s value at 300 K was about 4.33 k Ω . When the temperature diminished to 150 K, the R_s value rose to 277.52 k Ω . Large R_s at low temperatures might occur from the rise in n value, as well as the lack of carrier mobility in the fabricated B-doped UNCD/a-C:H films [19,104,109]. The presence of R_s can engender the degradation of the UV detection of the fabricated heterojunction diodes. For this reason, the parameter of R_s should be kept as low as possible for the enhancement of the device performance.

At 300 K, R_s of the p-UNCD/n-Si devices created via CAPD was found that higher than that of p-UNCD/n-Si devices built via PLD [104]. This might be due to the agglomeration of UNCD grains.

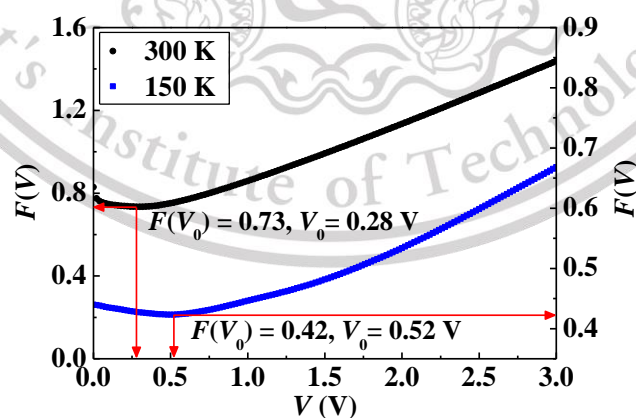


Figure 4.20 $F(V)$ - V profiles at 300 K and 150 K for the p-UNCD/n-Si devices constructed via CAPD.

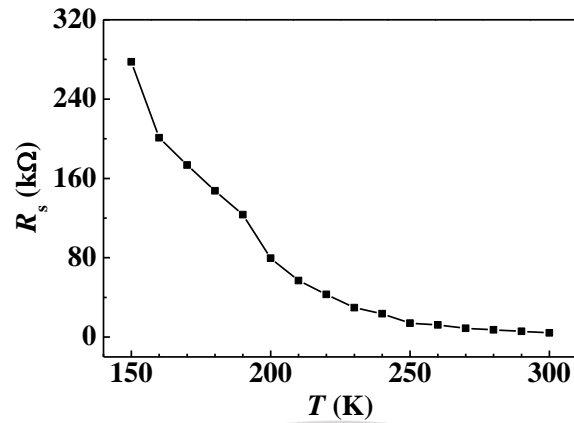


Figure 4.21 R_s variance plotted with temperature for the p-UNCD/n-Si devices constructed through CAPD.

Table 4.3 Significant diode parameters at different temperatures for the p-UNCD/n-Si devices created via CAPD.

T (K)	TE theory			Norde approach	
	n	J_0 (A cm $^{-2}$)	ϕ_b (eV)	ϕ_b (eV)	R_s (k Ω)
150	6.37	5.84×10^{-9}	0.43	0.48	277.52
160	5.66	6.79×10^{-9}	0.46	0.52	201.02
170	5.02	9.58×10^{-9}	0.49	0.54	173.48
180	4.67	1.01×10^{-8}	0.52	0.57	147.60
190	4.09	1.63×10^{-8}	0.54	0.59	123.45
200	3.90	2.67×10^{-8}	0.56	0.61	79.54
210	3.61	3.76×10^{-8}	0.58	0.65	56.94
220	3.43	5.78×10^{-8}	0.61	0.67	43.05
230	3.28	9.13×10^{-8}	0.63	0.69	29.63
240	3.18	1.48×10^{-7}	0.64	0.70	23.62
250	3.10	2.65×10^{-7}	0.66	0.72	14.02
260	3.02	3.71×10^{-7}	0.68	0.73	12.33
270	2.96	5.89×10^{-7}	0.70	0.74	8.82
280	2.91	9.11×10^{-7}	0.72	0.76	7.24
290	2.87	1.43×10^{-6}	0.73	0.78	5.84
300	2.82	2.08×10^{-6}	0.75	0.80	4.33

4.3.4 Dark and irradiated J - V profiles at different temperatures

Figure 4.22 discloses the J - V profiles for the p-UNCD/n-Si devices produced via CAPD, which were tested under darkness and irradiation by UV light with 254-nm wavelength at (a) 300 K and (b) 150 K. The created devices tested at 300 K showed the detection under the irradiation of UV light with a small photo-created current in the negative bias voltage. The response to UV light revealed that a large number of diamond grains allowed the photocarriers to be effectively created when the manufactured heterojunctions were irradiated by UV light [22,82]. Nevertheless, the small photo-created current might originate in the interface state appearing at the heterojunction interfaces [96,112,113]. This determinant would trap the photo-created carriers [96,112,113]. At 150 K, the photocurrent proportion to the dark current was enhanced over two orders of magnitude at the zero bias. This result might originate in the decrease in leakage current when the temperature was diminished [22].

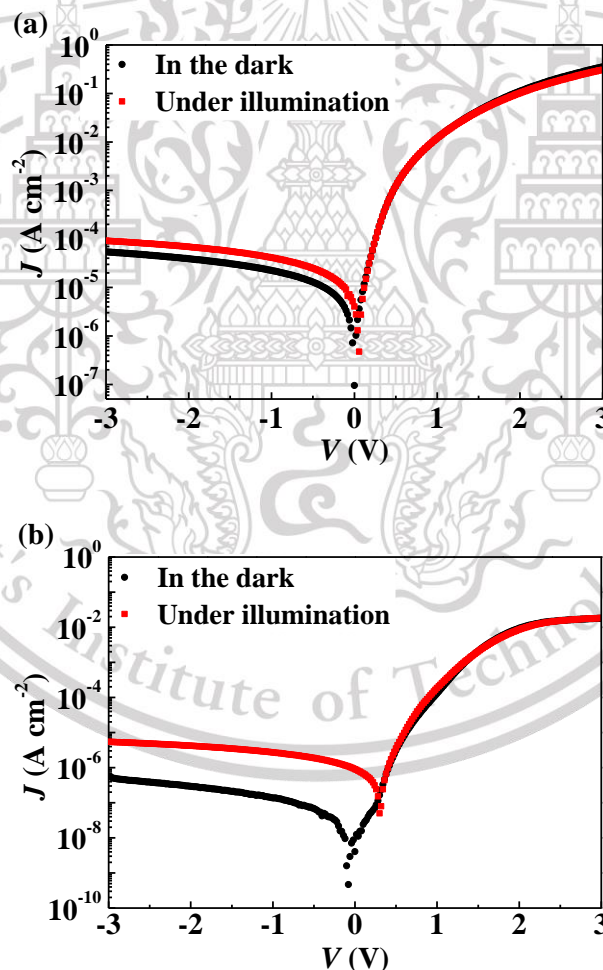


Figure 4.22 Dark and irradiated J - V characteristics at (a) 300 K and (b) 150 K for the p-UNCD/n-Si devices produced by CAPD.

4.3.5 Dynamic resistance and detectivity at different temperatures

Figure 4.23 reveals the dynamic resistance profiles at 300 K and 150 K, which were extracted from the dark J - V data of the p-UNCD/n-Si devices built via CAPD. The assessed dynamic resistance at 0 V (R_0) of the built devices was $3.10 \times 10^6 \Omega$ at 300 K and rose to $9.44 \times 10^8 \Omega$ at 150 K. Dynamic resistance is the factor that affected Johnson noises [22,114]. Thus, the rise in dynamic resistance at low temperatures can engender low Johnson noise [22,114]. The dynamic resistance area products at 0 V (AR_0) were found to be $2.43 \times 10^4 \Omega \text{ cm}^2$ at 300 K, and $7.41 \times 10^6 \Omega \text{ cm}^2$ at 150 K. AR_0 directly affected the device detectivity [22]. Namely, large photodetector area and high dynamic resistance were required to obtain high detectivity for photodetectors.

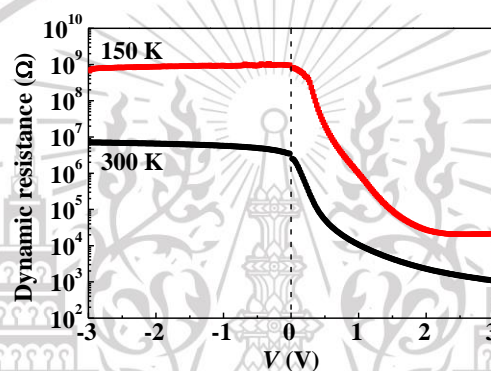


Figure 4.23 Dynamic resistance profiles plotted with voltage at 300 K and 150 K.

The photo detectivity is specified as the inverse of the noise-equivalent power. The larger detectivities are proper for detecting a small signal. Normally, the noise performance of the devices can be specified using the Johnson noise function in low background radiation. Johnson noise limited detectivity (D^*) value at 0 V can be elucidated by the following relation:

$$D^* \equiv R_\lambda \left(\frac{R_0 A}{4kT} \right)^{1/2}$$

where R_λ and R_0 convey the photocurrent responsivity and the dynamic resistance at zero bias, respectively. Further, A presents the device area, k demonstrates Boltzmann's constant, and T means the operating temperature in degrees Kelvin.

The D^* values at 0 V for the p-UNCD/n-Si devices created by CAPD were $2.37 \times 10^9 \text{ Hz}^{1/2} \text{ cm/W}$ at 300 K and $1.34 \times 10^{10} \text{ Hz}^{1/2} \text{ cm/W}$ at 150 K. High photo-detectivity at low temperatures might occur from the decrease in leakage current at low temperatures [81,96,111]. The diminution of leakage current might stem from the reduction of carrier density of p-UNCD/a-C:H films at low temperatures [80,104].

Further, the acquired D^* of the p-UNCD/n-Si devices created by CAPD can be compared to those of the existing GaN photodetectors, which held the D^* value around $1.24 \times 10^9 \text{ Hz}^{1/2} \text{ cm/W}$ at room temperature [15,114]. However, the D^* value of the manufactured devices is still lower than that of SiC photodetectors, which owned the D^* value around $3.60 \times 10^{15} \text{ Hz}^{1/2} \text{ cm/W}$ at room temperature [102].

4.3.6 Study on Z' - Z'' results and equivalent circuit for the heterojunction behavior at different voltages

The impedance data were collected at different voltages ranging from 0 V to 0.5 V at room temperature. Figure 4.24 (a) depicts the Z' - f profiles under various voltages of the p-UNCD/n-Si devices built by CAPD. The Z' - f profiles exhibited two flat areas at low and high frequencies. At low frequency, the Z' magnitude decreased with raising the voltage. At frequencies above 10 kHz, the Z' magnitude changed slightly, although the voltage increased. This might be relative to the space charge release in the material [115]. Z' might occur from two sorts of resistance from biasing the different frequencies [116,117]. At high frequencies, the Z' term might be relative to R_s from Ohmic contact, electrodes, and bulk resistance of the active layer [116,117]. At low frequencies, the Z' part might be due to R_p , regulated by charge transport [116,117].

The Z'' - f spectra as a function of voltage are disclosed in Figure 4.24 (b). At frequencies below 100 kHz, the Z'' - f curves showed the decrease in the Z'' magnitudes with increasing voltage. However, the increase of voltage at frequencies above 100 kHz barely impacted the Z'' value. All the Z'' - f profiles gave a peak for each voltage, which the peak shifted to higher frequencies with increasing voltage. This implied that the carrier relaxation time decreased as the rise in voltage [115,118]. Nonetheless, all Z'' - f profiles depict the amalgamation of Z'' at frequencies over 100 kHz. This might be due to the accumulation or space charge polarization at high frequencies [115,117].

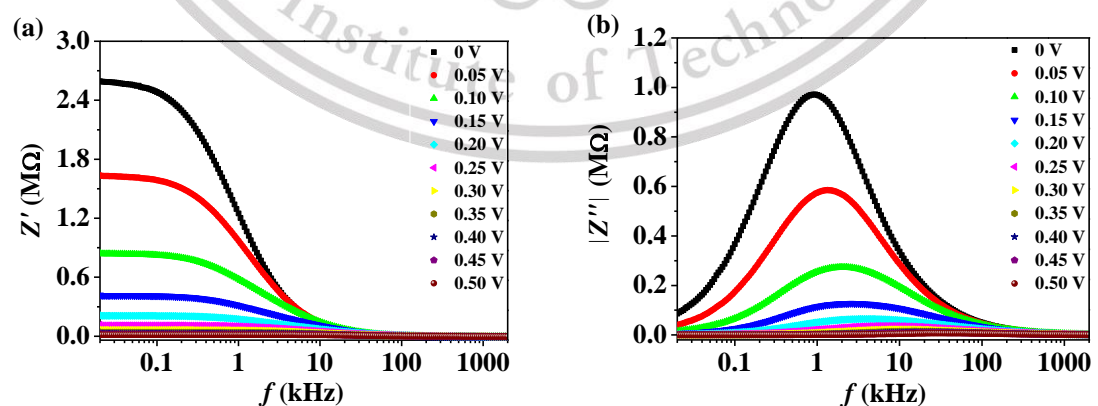


Figure 4.24 Characteristics of (a) Z' - f and (b) Z'' - f at different voltages for the p-UNCD/n-Si devices constructed through CAPD.

This material is reserved for educational use only, not allowed for commercial use.

Forbidden to modify the content, and cite the document when use.

Figure 4.25 depicts the Z'' - Z' curves of the p-UNCD/n-Si devices built via CAPD under various voltages at room temperature. Right and left sides of these curves were the minimum and maximum frequencies, respectively. All Z'' - Z' curves were reduced with raising the voltage. Each Z'' - Z' profile revealed one semicircle relative to one kind of relaxation process [116]. Further, all centers of Z'' - Z' curves were depressed. The Z'' - Z' results of the formed devices should conform to an equivalent circuit model comprised of R_s combined with the parallel combination of R_p and CPE, as illustrated in the inset of Figure 4.25 [67-69]. The existing R_s might originate in the resistance within neutral regions and the Ohmic contact [18,68]. R_p is defined by resistance from the charge transport mechanism [18,68]. CPE signifies the non-ideal behavior with an alterable parameter to compensate for non-homogeneity in the blocking interfaces due to the surface states or the porosity of the film surfaces [18,68].

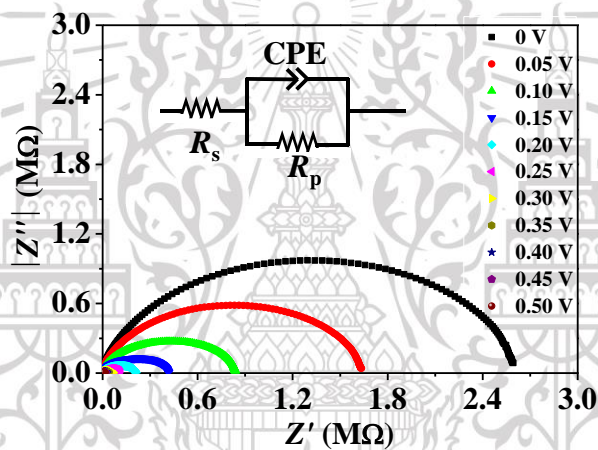


Figure 4.25 Z'' - Z' spectra at different voltages of the p-UNCD/n-Si devices built by CAPD. The inset is a circuit model related to heterojunction behavior.

Chapter 5

Conclusion and suggestions

5.1 Conclusion

5.1.1 Heterojunction devices of p-Si/n- β -FeSi₂ formed by FTS

The heterojunction devices consisting of p-Si substrates and n- β -FeSi₂ films were manufactured through FTS at a substrate temperature of 600 °C. The created devices revealed a large reverse leakage current, including a small response to NIR light. These might occur from the interface states existing at the junction interface and R_s of the devices. The $C-V$ and $G/\omega-V$ measurements were operated as a function of frequency ranging from 5 kHz to 1 MHz to estimate N_{ss} and R_s by the methods of Hill-Coleman and Nicollian-Brews, respectively. It was found that both R_s and N_{ss} values increased when the frequency value was decreased. The computed values of R_s at 0 V were 2.21 k Ω at 5 kHz and 13.66 Ω at 1 MHz. The values of N_{ss} were 3.48×10^{12} eV⁻¹ cm⁻² at 5 kHz and 4.68×10^{11} eV⁻¹ cm⁻² at 1 MHz. The obtained results proved the presence of interface states and R_s in the created p-Si/n- β -FeSi₂ devices constructed by FTS. These are the probable cause of the degraded device performances.

5.1.2 Heterojunction devices of p-UNCD/n-Si created by PLD

The p-UNCD/n-Si devices were constructed via PLD at a substrate temperature of 550 °C. The manufactured devices disclosed a large leakage current with a relatively weak response to UV light. These might be due to the interface states and R_s occurring in the created devices. The $C-V$ and $G/\omega-V$ characteristics were collected in a frequency range of 40 kHz - 2 MHz for extracting the N_{ss} and R_s values by Hill-Coleman and Nicollian-Brews models, respectively. The results exposed the increase in R_s and N_{ss} with reducing the frequency. R_s values at 0 V were 1.72 k Ω at 40 kHz and 154.41 Ω at 2 MHz. N_{ss} values were 1.78×10^{13} eV⁻¹ cm⁻² at 40 kHz and 1.39×10^{12} eV⁻¹ cm⁻² at 2 MHz. These outcomes disclosed the occurrence of R_s and interface states, which could cause the deterioration of diode performances.

5.1.3 Heterojunction devices of p-UNCD/n-Si produced via CAPD

The p-UNCD/n-Si devices were created by CAPD at a substrate temperature of 500 °C. The $J-V$ profiles were examined at different temperatures in a range between 150 K and 300 K. The formed diodes disclosed appropriate rectified $J-V$ characteristics and a quite large leakage current at 300 K. The decrease in leakage current was over two orders of magnitude after the temperature reduced to 150 K. From the dark $J-V$ results, the diode parameters, such as n , ϕ_b , and R_s were appraised through the TE

This material is reserved for educational use only, not allowed for commercial use.

Forbidden to modify the content, and cite the document when use.

theory and Norde approach. From the TE theory, the n value was 2.82 at 300 K, which indicated the dominant carrier mechanism of heavy recombination and tunneling. At 150 K, the n value increased to be 6.37, implying that the tunneling process regulated the carrier transport. The ϕ_b value estimated by TE theory was around 0.75 eV at 300 K and 0.43 at 150 K, which both values tallied with those of Norde method. The decrease in ϕ_b at low temperatures might be due to the non-uniformity of charge at the junction interface. The R_s values computed by Norde approach were 4.33 k Ω at 300 K and 277.52 k Ω at 150 K. The rise in R_s might occur from the increase in n and the lack of carrier mobility in the B-doped UNCD/a-C:H films at low temperatures.

At 300 K, the devices showed minimal UV response. At 150 K, the leakage current was significantly reduced. The ratio of photocurrent to dark current at 0 V was improved by over two orders of magnitude compared to that of 300 K. The D^* values at 0 V were 2.37×10^9 Hz^{1/2} cm/W at 300 K and 1.34×10^{10} Hz^{1/2} cm/W at 150 K. Both improvements in the ratio of photocurrent to dark current and the detectivity at low temperatures might occur from the decrease in leakage current. The D^* values of the p-UNCD/n-Si devices built by CAPD revealed the possibility for the practical application of UV detection.

Their $Z'-Z''$ characteristics of the built devices were measured at different voltages to anticipate the relaxation phenomenon and equivalent circuit model for the created devices. All diameter of $Z'-Z''$ curves decreased with an increase in voltage. All $Z'-Z''$ profiles presented single semicircles relative to one type of carrier relaxation process. Further, the center of each single semicircle was depressed. Therefore, the proper equivalent electrical circuit model for the heterojunction behavior was comprised of R_s combined with the parallel circuit of R_p and CPE.

5.2 Suggestions

To improve the device performance, future works should be carried out as the following list:

1. Reduce the N_{ss} value by adding a thin blocking layer between p and n layers.
2. Diminish the trap zone occurred from many grain boundaries and porosity by the improvement of β -FeSi₂ crystallinity
3. Decrease the contact resistance by optimizing the metal deposition rate.
4. Improve the n value close to 1 by decreasing the interface states.

References

- [1] Joyce, H.J., Gao, Q., Tan, H.H., Jagadish, C., Kim, Y., Zou, J., Smith, L.M., Jackson, H.E., Yarrison-Rice, J.M., Parkinson, P. and Johnston, M.B. 2011. "III-V semiconductor nanowires for optoelectronic device applications." *Progress in Quantum Electronics* 35(2-3) : 23-75.
- [2] Farag, A.A.M., Mansour, A.M., Ammar, A.H., Rafea, M.A. and Farid, A.M. 2012. "Electrical conductivity, dielectric properties and optical absorption of organic based nanocrystalline sodium copper chlorophyllin for photodiode application." *Journal of alloys and compounds* 513 : 404-413.
- [3] Ker, P.J., Tan, C.H. and David, J.P. 2013. "High speed low noise InAs electron avalanche photodiodes for telecommunication and infrared sensing applications." 78-80. in 2013 IEEE 4th International Conference on Photonics : IEEE.
- [4] Gullu, H.H., Yildiz, D.E., Kocyigit, A. and Yildirim, M. 2020. "Electrical properties of Al/PCBM:ZnO/p-Si heterojunction for photodiode application." *Journal of Alloys and Compounds* 827 : 154279.
- [5] Cohen, M.J. and Olsen, G.H. 1993. "Room-temperature InGaAs camera for NIR imaging." 1946 : 436-443. in *Infrared Detectors and Instrumentation : International Society for Optics and Photonics*.
- [6] Yakovlev, Y.P., Baranov, A.N., Imenkov, A.N. and Mikhailova, M.P. 1991. "Optoelectronic LED-photodiode pairs for moisture and gas sensors in the spectral range 1.8-4.8 μm ." 1510 : 170-177. in *Chemical and Medical Sensors : International Society for Optics and Photonics*.
- [7] Hansen, M.P. and Malchow, D.S. 2008. "Overview of SWIR detectors, cameras, and applications." 6939 : 69390I. in *Thermosense Xxx : International Society for Optics and Photonics*.
- [8] Hamamatsu. 2021. **InGaAs photodiodes.** [Online] Available: <https://www.hamamatsu.com/us/en/product/optical-sensors/photodiodes/ingaas-photodiode/index.html>.
- [9] Hamamatsu. 2021. **InAs photovoltaic detectors.** [Online] Available: <https://www.hamamatsu.com/jp/en/product/optical-sensors/infrared-detector/inas-photovoltaic-detector/index.html>.
- [10] Jewett, S.A., Yoder, J.A. and Ivanisevic, A. 2012. "Surface modifications on InAs decrease indium and arsenic leaching under physiological conditions." *Applied Surface Science* 261 : 842-850.
- [11] Chen, H., Liu, K., Hu, L., Al-Ghamdi, A.A. and Fang, X. 2015. "New concept ultraviolet photodetectors." *Materials Today* 18(9) : 493-502.

- [12] Hamamatsu. 2009. **Hamamatsu Photonics' commitment to Photonics Technology** [Online] Available: https://www.hamamatsu.com/sp/hpe/HamamatsuNews/HamamatsuNews_0109.pdf.
- [13] Guo, Z.X. 1998. "Towards cost effective manufacturing of Ti/SiC fibre composites and components." *Materials Science and Technology* 14 : 864-872.
- [14] Wright, N.G., Horsfall, A.B. and Vassilevski, K. 2008. "Prospects for SiC electronics and sensors." *Materials Today* 11(1-2) : 16-21.
- [15] Gundimeda, A., Krishna, S., Aggarwal, N., Sharma, A., Sharma, N.D., Maurya, K.K., Husale, S. and Gupta, G. 2017. "Fabrication of non-polar GaN based highly responsive and fast UV photodetector." *Applied Physics Letters* 110(10) : 103507.
- [16] Shaban, M., Nomoto, K., Nakashima, K. and Yoshitake, T. 2008. "Low-temperature annealing of n-type β -FeSi₂/p-type Si heterojunctions." *Japanese Journal of Applied Physics* 47 : 3444.
- [17] Sittimart, P., Nopparuchikun, A. and Promros, N. 2017. "Computation of heterojunction parameters at low temperatures in heterojunctions comprised of n-type β -FeSi₂ thin films and p-type Si (111) substrates grown by radio frequency magnetron sputtering." *Advances in Materials Science and Engineering* 2017 : 6590606.
- [18] Aouniti, A., Elmsellem, H., Tighadouini, S., Elazzouzi, M., Radi, S., Chetouani, A., Hammouti, B. and Zarrouk, A. 2016. "Schiff's base derived from 2-acetyl thiophene as corrosion inhibitor of steel in acidic medium." *Journal of Taibah University for Science* 10 : 774-785.
- [19] Farag, A.A.M., Yahia, I.S., Wojtowicz, T. and Karczewski, G. 2010. "Influence of temperature and illumination on the electrical properties of p-ZnTe/n-CdTe heterojunction grown by molecular beam epitaxy." *Journal of Physics D: Applied Physics* 43 : 215102.
- [20] Caglar, M. and Yakuphanoglu, F. 2009. "Fabrication and electrical characterization of flower-like CdO/p-Si heterojunction diode." *Journal of Physics D: Applied Physics* 42 : 045102.
- [21] Promros, N., Baba, R., Kishimoto, H., Sittimart, P., Hanada, T., Hanada, K., Zkria, A., Shaban, M. and Yoshitake, T. 2016. "Characterization of n-type nanocrystalline iron disilicide/intrinsic ultrananocrystalline diamond/amorphous carbon composite/p-type silicon heterojunctions at low temperatures." *Journal of Nanoelectronics and Optoelectronics* 11 : 579-584.

- [22] Zkria, A., Gima, H. and Yoshitake, T. 2017. "Application of nitrogen-doped ultrananocrystalline diamond/hydrogenated amorphous carbon composite films for ultraviolet detection." *Applied Physics A* 123 : 167.
- [23] Saran, R., Nordin, M.N. and Curry, R.J. 2013. "Facile fabrication of PbS Nanocrystal:C₆₀ fullerite broadband photodetectors with high detectivity." *Advanced Functional Materials* 23 : 4149-4155.
- [24] Ali, S., Chang, S., Imran, M., Shi, Q., Chen, Y. and Zhong, H. 2019. "Impedance spectroscopy: A versatile technique to understand solution-processed optoelectronic devices." *Physica Status Solidi (RRL)-Rapid Research Letters* 13 : 1800580.
- [25] Xu, L., Lee, Y. J. and Hsu, J. W. 2014. "Charge collection in bulk heterojunction organic photovoltaic devices: An impedance spectroscopy study." *Applied Physics Letters* 105 : 123904.
- [26] Yoshitake, T., Inokuchi, Y., Yuri, A. and Nagayama, K. 2006. "Direct epitaxial growth of semiconducting β -FeSi₂ thin films on Si (111) by facing targets direct-current sputtering." *Applied Physics Letters* 88 : 182104.
- [27] Izumi, S., Shaban, M., Promros, N., Nomoto, K. and Yoshitake, T. 2013. "Near-infrared photodetection of β -FeSi₂/Si heterojunction photodiodes at low temperatures." *Applied Physics Letters* 102 : 032107.
- [28] Promros, N., Sittimart, P. and Kaenrai, W. 2016. "Investigation of electrical transport properties in heterojunctions comprised of silicon substrate and nanocrystalline iron disilicide films." *International Journal of Nanotechnology* 13 : 903-912.
- [29] Mahan, J.E., Geib, K.M., Robinson, G.Y., Long, R.G., Xinghua, Y., Bai, G., Nicolet, M.-A. and Nathan, M. 1990. "Epitaxial films of semiconducting FeSi₂ on (001) silicon." *Applied Physics Letters* 56 : 2126-2128.
- [30] Leong, D.N., Harry, M.A., Reeson, K.J. and Homewood, K.P. 1996. "On the origin of the 1.5 μ m luminescence in ion beam synthesized β -FeSi₂." *Applied Physics Letters* 68 : 1649-1650.
- [31] Tanaka, M., Kumagai, Y., Suemasu, T. and Hasegawa, F. 1997. "Reactive deposition epitaxial growth of β -FeSi₂ layers on Si (001)." *Applied surface science* 117 : 303-307.
- [32] Takeda, K., Yoshitake, T., Nakagauchi, D., Ogawa, T., Hara, D., Itakura, M., Kuwano, N., Tomokiyo, Y., Kajiwara, T. and Nagayama, K. 2007. "Epitaxy in Fe₃Si/FeSi₂ superlattices prepared by facing target direct-current sputtering at room temperature." *Japanese Journal of Applied Physics* 46(12R) : 7846.

- [33] Liu, G., Wang, X., Han, G., Yu, J. and Zhao, H. 2020. "Earth abundant colloidal carbon quantum dots for luminescent solar concentrators." *Materials Advances* 1(2) : 119-138.
- [34] Ohmagari, S. and Yoshitake, T. 2012. "Deep-ultraviolet light detection of p-type ultrananocrystalline diamond/hydrogenated amorphous carbon composite films." *Applied Physics Express* 5 : 065202.
- [35] Yoshitake, T., Nagano, A., Itakura, M., Kuwano, N., Hara, T. and Nagayama, K. 2007. "Spectral absorption properties of ultrananocrystalline diamond/amorphous carbon composite thin films prepared by pulsed laser deposition." *Japanese Journal of Applied Physics* 46 : L936-L938.
- [36] Ohmagari, S., Al-Riyami, S. and Yoshitake, T. 2011. "Heterojunction diodes comprised of n-type silicon and p-type ultrananocrystalline diamond/hydrogenated amorphous carbon composite." *Japanese Journal of Applied Physics* 50 : 035101.
- [37] Katamune, Y., Takeichi, S., Ohtani, R., Koizumi, S., Ikenaga, E., Kamitani, K., Sugiyama, T. and Yoshitake, T. 2019. "Electrical properties of boron-incorporated ultrananocrystalline diamond/hydrogenated amorphous carbon composite films." *Applied Physics A* 125 : 295.
- [38] Naragino, H., Egiza, M., Tominaga, A., Murasawa, K., Gonda, H., Sakurai, M., & Yoshitake, T. 2016. "Hard coating of ultrananocrystalline diamond/nonhydrogenated amorphous carbon composite films on cemented tungsten carbide by coaxial arc plasma deposition." *Applied Physics A* 122 : 761.
- [39] Yoshitake, T., Shiraishi, G. and Nagayama, K. 2002. "Elimination of droplets using a vane velocity filter for pulsed laser ablation of FeSi₂." *Applied surface science* 197 : 379-383.
- [40] Kubaschewski, O. 1982. **Iron Binary Phase Diagram. 136.** New York: John Wiley and Sons.
- [41] Comrie, C.M., Falepin, A., Richard, O., Bender, H. and Vantomme, A. 2004. "Metastable iron silicide phase formation by pulsed laser annealing." *Journal of Applied Physics* 95(5) : 2365-2370.
- [42] Takarabe, K., Ikai, T., Mori, Y., Udono, H. and Kikuma, I. 2004. "Structural study of FeSi₂ under pressure." *Journal of Applied Physics* 96 (2004) 4903-4908.
- [43] Hattori, A.N., Hattori, K., Kataoka, K., Takematsu, E., Ishii, A., Komori, F. and Daimon, H. 2014. "Systematic study of surface magnetism in Si (111)-Fe system grown by solid phase epitaxy: In situ schematic magnetic phase diagram of Si (111)-Fe." *Journal of Magnetism and Magnetic Materials* 363 : 158-165.

This material is reserved for educational use only, not allowed for commercial use.

Forbidden to modify the content, and cite the document when use.

- [44] Mahan, J.E., Thanh, V.L., Chevrier, J., Berbezier, I., Derrien, J. and Long, R.G. 1993. "Surface electron-diffraction patterns of β -FeSi₂ films epitaxially grown on silicon." *Journal of Applied Physics* 74(3) : 1747-1761.
- [45] Christensen, N.E. 1990. "Electronic structure of β -FeSi₂." *Physical Review B* 42 : 7149-7150.
- [46] Zkria, A., Shaban, M., Hanada, T., Promros, N. and Yoshitake, T. 2016. "Current transport mechanisms in n-type ultrananocrystalline diamond/p-type Si heterojunctions." *Journal of Nanoscience and Nanotechnology* 16 : 12749-12753.
- [47] Yoshitake, T., Nakagawa, Y., Nagano, A., Ohtani, R., Setoyama, H., Kobayashi, E., Sumitani, K., Agawa, Y. and Nagayama, K. 2010. "Structural and physical characteristics of ultrananocrystalline diamond/hydrogenated amorphous carbon composite films deposited using a coaxial arc plasma gun." *Japanese Journal of Applied Physics* 49(1R) : 015503.
- [48] Baptista, A., Silva, F., Porteiro, J., Míguez, J. and Pinto, G. 2018. "Sputtering physical vapour deposition (PVD) coatings: A critical review on process improvement and market trend demands." *Coatings* 8 : 402.
- [49] Shaban, M. and Yoshitake, T. 2011. "n-Type β -FeSi₂/p-type Si near-infrared photodiodes prepared by facing-targets direct-current sputtering." *Advances in Photodiodes 2011* : 315.
- [50] Mitra, J., Abraham, G. J., Kesaria, M., Bahl, S., Gupta, A., Shivaprasad, S.M., Viswanadham, C.S., Kulkarni, U.D. and Dey, G. K. 2012. "Role of substrate temperature in the pulsed laser deposition of zirconium oxide thin film." *Materials Science Forum* 710 : 757-761.
- [51] Agawa, Y., Tanaka, H., Torisu, S., Endo, S., Tsujimoto, A., Gonohe, N., Malgras, V., Aldalbahi, A., Alshehri, S.M., Kamachi, Y., Li, C. and Yamauchi, Y. 2015. "Preparation of a platinum electrocatalyst by coaxial pulse arc plasma deposition." *Science and Technology of Advanced Materials* 16 : 024804.
- [52] F. Rana, 2016. **Semiconductor optoelectronics**. [Online] Available : <https://courses.cit.cornell.edu/ece533/Lectures/handout2.pdf>.
- [53] Sze, S.M. and Kwok, K.N. 2007. **Semiconductor Devices Physics and Technology**. New York: John Wiley and Sons.
- [54] Hamamatsu. 2021. **Photodiode Technical Information**. [Online] Available : http://users.monash.edu.au/~erict/Resources/sensors/photodiode_technical_information.pdf
- [55] Korkut, H., Yıldırım, N. and Turut, A. 2009. "Thermal annealing effects on *I-V-T* characteristics of sputtered Cr/n-GaAs diodes." *Physica B: Condensed Matter* 404(21) : 4039-4044.

- [56] Rhoderick, E.H. and Williams, R.H. 1988. **Metal-Semiconductor Contacts**. Oxford : Oxford University Press.
- [57] Nottingham, W.B., Good, R.H., Müller, E.W., Kollath, R., Weissler, G.L., Allis, W.P., Loeb, L.B., von Engel A. and Little, P.F. 1956. **Electron-Emission Gas Discharges I/Elektronen-Emission Gasentladungen I**. Berlin : Springer.
- [58] Norde, H. 1979. "A modified forward I - V plot for Schottky diodes with high series resistance." *Journal of Applied Physics* 50(7) : 5052-5053.
- [59] Sato K. and Yasumura, Y. 1985. "Study of forward I - V plot for Schottky diodes with high series resistance." *Journal of applied physics* 58(9) : 3655-3657.
- [60] Johnson, J.L., Samoska, L.A., Gossard, A.C., Merz, J.L., Jack, M.D., Chapman, G.R., Baumgratz, B.A., Kosai, K. and Johnson, S.M. 1996. "Electrical and optical properties of infrared photodiodes using the $\text{InAs}/\text{Ga}_{1-x}\text{In}_x\text{Sb}$ superlattice in heterojunctions with GaSb." *Journal of Applied Physics* 80 : 1116-1127.
- [61] Bülbül, M., Zeyrek, S., Altındal, Ş. and Yüzer, H. 2006. "On the profile of temperature dependent series resistance in $\text{Al}/\text{Si}_3\text{N}_4/\text{p-Si}$ (MIS) Schottky diodes." *Microelectronic Engineering* 83(3) : 577-581.
- [62] Nicollian, E.H. and Brews, J.R. 1982. **MOS (Metal Oxide Semiconductor) Physics and Technology. 176**. New York: John Wiley and Sons.
- [63] Nicollian, E.H. and Goetzberger, A. 1965. "MOS conductance technique for measuring surface state parameters." *Applied Physics Letters* 7 : 216.
- [64] Hill, W.A. and Coleman, C.C. 1980. "A single-frequency approximation for interface-state density determination." *Solid-State Electronics* 23(9) : 987-993.
- [65] Tataroglu, B., Altındal, S. and Tataroglu, A. 2006. "The C - V - f and G/ω - V - f characteristics of $\text{Al}/\text{SiO}_2/\text{p-Si}$ (MIS) structures." *Microelectronic Engineering* 83(10) : 2021-2026.
- [66] Kavasoglu, N., Tozlu, C., Pakma, O., Kavasoglu, A. S., Ozden, S., Metin, B., Birgi, O. and Oktik, S. 2009. "Room-temperature interface state analysis of Au/Poly (4-vinyl phenol)/ p-Si structure." *Synthetic metals* 159(17-18) : 1880-1884.
- [67] Friesen, G., Ozsar, M.E. and Dunlop, E.D. 2000. "Impedance model for CdTe solar cells exhibiting constant phase element behaviour." *Thin Solid Films* 361-362 : 303-308.
- [68] Arredondo, B., Martín-López, M. B., Romero, B., Vergaz, R., Romero-Gomez, P. and Martorell, J. 2016. "Monitoring degradation mechanisms in PTB7: PC71BM photovoltaic cells by means of impedance spectroscopy." *Solar Energy Materials and Solar Cells* 144 : 422-428.
- [69] Ebrahim, S. 2011. "Impedance spectroscopy and equivalent circuits of heterojunction solar cell based on n-Si/polyaniline base." *Polymer Science*

Series A 53 : 1217-1226.

- [70] Terzano, R., Denecke, M.A., Falkenberg, G., Miller, B., Paterson, D. and Janssens, K. 2019. "Recent advances in analysis of trace elements in environmental samples by X-ray based techniques (IUPAC Technical Report)." *Pure and Applied Chemistry* 91(6) : 1029-1063.
- [71] Akhtar, K., Khan, S.A., Khan, S.B., and Asiri, A.M. 2018. **Scanning electron microscopy: Principle and applications in nanomaterials characterization. 113-145.** Cham : Springer International Publishing AG.
- [72] Chen, W., Wang, J., Wan, F. and Wang, P. 2019. "Review of optical fibre sensors for electrical equipment characteristic state parameters detection." *High Voltage*, 4(4) : 271-281.
- [73] Sittimart, P. 2015. "Characterization of junction parameters in n-type FeSi_2 /p-type Si heterojunctions and wettability properties of FeSi_2 thin films." M.D. Thesis of King Mongkut's Institute of Technology Ladkrabang.
- [74] Krishnan, A. 2017. **Understanding current-voltage curves of non-linear devices** [Online] Available : <https://www.allaboutcircuits.com/technical-articles/understanding-i-v-curves-of-non-linear-devices/>.
- [75] Promros, N. 2012. "Application of Iron disilicides to photodiodes." Ph.D. Thesis of Kyushu University.
- [76] Goetzberger, A., Klausmann, E. and Schulz, M.J. 1976. "Interface states on semiconductor/insulator surfaces." *Critical Reviews in Solid State and Material Sciences* 6(1) : 1-43.
- [77] Jiang, J., Ling, C., Xu, T., Wang, W., Niu, X., Zafar, A., Yan, Z., Wang, X., You, Y., Sun, L., Lu, J., Wang, J. and Ni, Z. 2018. Defect engineering for modulating the trap states in two-dimensional photoconductor. arXiv preprint arXiv:1808.06093.
- [78] Shaban, M., Nakashima, K., Yokoyama, W. and Yoshitake, T. 2007. "Photovoltaic properties of n-type β - FeSi_2 /p-type Si heterojunctions" *Japanese Journal of Applied Physics* 46 : L667.
- [79] Shaban, M., Nomoto, K., Izumi, S. and Yoshitake, T. 2009. "Characterization of near-infrared n-type β - FeSi_2 /p-type Si heterojunction photodiodes at room temperature." *Applied Physics Letters* 94 : 222113.
- [80] Ohmagari, S., Hanada, T., Katamune, Y., Al-Riyami, S. and Yoshitake, T. 2014. "Carrier transport and photodetection in heterojunction photodiodes comprising n-type silicon and p-type ultrananocrystalline diamond/hydrogenated amorphous carbon composite films." *Japanese Journal of Applied Physics* 53(5) : 050307.
- [81] Hanada, T., Ohmagari, S., Zkria, A., Promros, N. and Yoshitake, T. 2017.

This material is reserved for educational use only, not allowed for commercial use.

Forbidden to modify the content, and cite the document when use.

- “Photodetection characteristics of heterojunctions comprising p-type ultrananocrystalline diamond films and n-type Si substrates at low temperatures.” *Journal of Nanoscience and Nanotechnology* 17(5) : 3348-3351.
- [82] Katamune, Y., Ohmagari, S., Al-Riyami, S., Takagi, S., Shaban, M. and Yoshitake, T. 2013. “Heterojunction diodes comprising p-type ultrananocrystalline diamond films prepared by coaxial arc plasma deposition and n-type silicon substrates.” *Japanese Journal of Applied Physics* 52(6R) : 065801.
- [83] Shaban, M., Izumi, S., Nomoto, K. and Yoshitake, T. 2009. “n-Type β -FeSi₂/intrinsic-Si/p-type Si heterojunction photodiodes for near-infrared light detection at room temperature.” *Applied Physics Letters* 95 : 162102.
- [84] Yoshitake, T., Nagamoto, T. and Nagayama, K. 2001. “Microstructure of β -FeSi₂ thin films prepared by pulsed laser deposition.” *Thin Solid Films* 381(2) : 236-243.
- [85] Giard, E., Taalat, R., Delmas, M., Rodriguez, J. B., Christol, P., Jaeck, J. and Ribet-Mohamed, I. 2014. “Comparison of the electro-optical performances of MWIR InAs/GaSb superlattice pin photodiode and FPA with asymmetrical designs.” 9070 : 90700W . in *Infrared Technology and Applications XL* : International Society for Optics and Photonics.
- [86] Promros, N., Baba, R., Takahara, M., Mostafa, T. M., Sittimart, P., Shaban, M. and Yoshitake, T. 2016. “Epitaxial growth of β -FeSi₂ thin films on Si (111) substrates by radio frequency magnetron sputtering and their application to near-infrared photodetection.” *Japanese Journal of Applied Physics* 55(6S2) : 06HC03.
- [87] Tuğluoğlu, N., Yüksel, Ö. F., Karadeniz, S. and Şafak, H. 2013. “Frequency dependent interface state properties of a Schottky device based on perylene-monoimide deposited on n-type silicon by spin coating technique.” *Materials Science in Semiconductor Processing* 16(3) : 786-791.
- [88] Zeyrek, S., Acaroğlu, E., Altındal, Ş., Birdoğan, S. and Bülbül, M.M. 2013. “The effect of series resistance and interface states on the frequency dependent C-V and G/ω-V characteristics of Al/perylene/p-Si MPS type Schottky barrier diodes.” *Current Applied Physics* 13(7) : 1225-1230.
- [89] Parlaktürk, F., Altındal, Ş., Tataroğlu, A., Parlak, M. and Agasiev, A. 2008. “On the profile of frequency dependent series resistance and surface states in Au/Bi₄Ti₃O₁₂/SiO₂/n-Si (MFIS) structures.” *Microelectronic engineering* 85(1) : 81-88.
- [90] Altındal, Ş., Kanbur, H., Tataroğlu, A. and Bülbül, M.M. 2007. “The barrier height distribution in identically prepared Al/p-Si Schottky diodes with the native

This material is reserved for educational use only, not allowed for commercial use.

Forbidden to modify the content, and cite the document when use.

- interfacial insulator layer (SiO₂)." *Physica B: Condensed Matter* 399(2) : 146-154.
- [91] Reddy, M.S.P., Lee, J.-H. and Jang, J.-S. 2013. "Frequency dependent series resistance and interface states in Au/bio-organic/n-GaN Schottky structures based on DNA biopolymer." *Synthetic Metals* 185-186 : 167-171.
- [92] Nopparuchikun, A., Promros, N., Teakchaicum, S., Onsee, P., Duangrawa, A. and Sittimart, P. 2017. "Carrier transportation properties and series resistance of n-type β -FeSi₂/p-type Si heterojunctions fabricated by RF magnetron sputtering." *Japanese Journal of Applied Physics* 56(6S2) : 06HE06.
- [93] Fouad, S.S., Sakr, G.B., Yahia, I.S., Abdel-Basset, D.M. and Yakuphanoglu, F. 2014. "Capacitance and conductance characterization of nano-ZnGa₂Te₄/n-Si diode." *Materials Research Bulletin* 49 : 369-383.
- [94] Karataş, Ş. and Türüt, A. 2010. "The frequency-dependent electrical characteristics of interfaces in the Sn/p-Si metal semiconductor structures." *Microelectronics Reliability* 50(3) : 351-355.
- [95] Zou, X. Y. 2017. "Simulation of n- β -FeSi₂/p-Si heterojunction solar cells based on AFORS-HET." *Modern Physics Letters B* 31(19-21) : 1740026.
- [96] Promros, N., Yamashita, K., Li, C., Kawai, K., Shaban, M., Okajima, T. and Yoshitake, T. 2012. "n-Type nanocrystalline FeSi₂/intrinsic Si/p-type Si heterojunction photodiodes fabricated by facing-target direct-current sputtering." *Japanese Journal of Applied Physics* 51(2R) : 021301.
- [97] Xu, Y., Jackson, R.L. and Marghitu, D.B. 2014. "Statistical model of nearly complete elastic rough surface contact." *International Journal of Solids and Structures* 51(5) : 1075-1088.
- [98] Nagano, A., Yoshitake, T., Hara, T. and Nagayama, K. 2008. "Optical properties of ultrananocrystalline diamond/amorphous carbon composite films prepared by pulsed laser deposition." *Carbon* 46(7-10) : 1199-1202.
- [99] Hara, T., Yoshitake, T., Fukugawa, T., Kubo, H., Itakura, M., Kuwano, N., Tomokiyo, Y. and Nagayama, K. 2006. "Ultrananocrystalline diamond prepared by pulsed laser deposition." *Diamond and Related Materials* 15(4-8) : 649-653.
- [100] Zeng, H., Konicek, A.R., Moldovan, N., Mangolini, F., Jacobs, T., Wylie, I., Arumugam, P.U., Siddiqui, S., Carpick, R.W. and Carlisle, J.A. 2015. "Boron-doped ultrananocrystalline diamond synthesized with an H-rich/Ar-lean gas system." *Carbon* 84 : 103-117.
- [101] Pu, J.-C., Wang, S.-F., Lin, C.-L. and Sung, J.C. 2010. "Characterization of boron-doped diamond-like carbon prepared by radio frequency sputtering." *Thin Solid Films* 519 : 521-526.

- [102] Yan, F., Xin, X., Aslam, S., Zhao, Y., Franz, D., Zhao, J. H. and Weiner, M. 2004. "4H-SiC UV photo detectors with large area and very high specific detectivity." *IEEE Journal of Quantum Electronics* 40(9) : 1315-1320.
- [103] Nicollian, E.H. and Goetzberger, A. 1967. "The Si-SiO₂ interface-electrical properties as determined by the metal-insulator-silicon conductance technique." *The Bell System Technical Journal* 46 : 1055-1033.
- [104] Chaleawpong, R., Promros, N., Charoenyuenyao, P., Hanada, T., Ohmagari, S., Zkria, A. and Yoshitake, T. 2019. "Diode parameters of heterojunctions comprising p-type ultrananocrystalline diamond films and n-type Si substrates." *Journal of Nanoscience and Nanotechnology* 19(3) : 1567-1573.
- [105] Shaban, M., Zkria, A. and Yoshitake, T. 2018. "Characterization and design optimization of heterojunction photodiodes comprising n-type ultrananocrystalline diamond/hydrogenated amorphous carbon composite and p-type Si." *Materials Science in Semiconductor Processing* 86 : 115-121
- [106] Katamune, Y., Ohmagari, S., Suzuki, I. and Yoshitake, T. 2012. "Effects of aluminum incorporation on diamond grain growth in ultrananocrystalline diamond/hydrogenated amorphous carbon composite films prepared by coaxial arc plasma deposition." *Japanese Journal of Applied Physics* 51(6R) : 068002.
- [107] Ali, A. M., Egiza, M., Murasawa, K., Fukui, Y., Gonda, H., Sakurai, M. and Yoshitake, T. 2019. "Negative bias effects on deposition and mechanical properties of ultrananocrystalline diamond/amorphous carbon composite films deposited on cemented carbide substrates by coaxial arc plasma." *Diamond and Related Materials* 96 : 67-73.
- [108] Al-Riyami, S., Ohmagari, S. and Yoshitake, T. 2010. "Nitrogen-doped ultrananocrystalline diamond/hydrogenated amorphous carbon composite films prepared by pulsed laser deposition." *Applied Physics Express* 3 : 115102.
- [109] Rodrigues, A.M. 2008. "Extraction of Schottky diode parameters from current-voltage data for a chemical-vapor-deposited diamond/silicon structure over a wide temperature range." *Journal of Applied Physics* 103 : 083708.
- [110] Song, Y.P., Van Meirhaeghe, R.L., Laflere, W.H., and Cardon, F. 1986. "On the difference in apparent barrier height as obtained from capacitance-voltage and current-voltage-temperature measurements on Al/p-InP Schottky barriers." *Solid-State Electronics* 29 : 633-638.
- [111] Promros, N., Chen, L. and Yoshitake, T. 2013. "Near-infrared photodetection in n-type nanocrystalline FeSi₂/p-type Si heterojunctions." *Journal of Nanoscience and Nanotechnology* 13 : 3577-3581.

- [112] Sittimart, P., Duangrawa, A., Onsee, P., Teakchaicum, S., Nopparuchikun, A. and Promros, N. 2018. "Interface state density and series resistance of n-type nanocrystalline FeSi₂/p-type Si heterojunctions formed by utilizing facing-target direct-current sputtering." *Journal of Nanoscience and Nanotechnology* 18(3) : 1841-1846.
- [113] Funasaki, S., Promros, N., Iwasaki, R., Takahara, M., Shaban, M. and Yoshitake, T. 2013. "Fabrication of mesa structural n-type nanocrystalline-FeSi₂/p-type Si heterojunction photodiodes by liftoff technique combined with photolithography." *Physica Status Solidi C* 10(12) : 1785-1788.
- [114] Walker, D., Saxler, A., Kung, P., Zhang, X., Hamilton, M., Diaz, J. and Razeghi, M. 1998. "Visible blind GaN pin photodiodes." *Applied Physics Letters* 72(25) : 3303-3305.
- [115] Dey, A., Dhar, J., Sil, S., Jana, R. and Ray, P.P. 2018. "Bias voltage-dependent impedance spectroscopy analysis of hydrothermally synthesized ZnS nanoparticles." *Journal of Materials Engineering and Performance* 27(6) : 2727-2733.
- [116] Zhang, Y., Li, L., Yuan, S., Li, G. and Zhang, W. 2013. "Electrical properties of the interfaces in bulk heterojunction organic solar cells investigated by electrochemical impedance spectroscopy." *Electrochimica Acta* 109 : 221-225.
- [117] Zkria, A., Abubakr, E., Sittimart, P. and Yoshitake, T. 2020. "Analysis of electrical characteristics of Pd/n-nanocarbon/p-Si heterojunction diodes: By $C-V-f$ and $G/\omega-V-f$." *Journal of Nanomaterials* 2020 : 4917946.
- [118] Zrida, H., Hriz, K., Jaballah, N., Hrichi, H., Kreher, D. and Majdoub, M. 2016. "New soluble anthracene-based polymer for opto-electronic applications." *Journal of materials science* 51(2) : 680-693.

Author Biography

Name Miss Rawiwan Chaleawpong
Date of Birth 22 May 1994
Address Department of Physics, School of Science,
King Mongkut's Institute of Technology Ladkrabang, Thailand
Education (2016) Bachelor of Science in Physics GPA 3.14
King Mongkut's Institute of Technology Ladkrabang
(2018) Master of Science in Physics GPA 3.62
King Mongkut's Institute of Technology Ladkrabang

Academic Publications

- [1] Nattakorn Borwornpornmetee, Peerasil Charoenyuenyao, **Rawiwan Chaleawpong**, Boonchoat Paosawatyanong, Rungrueng Phatthanakun, Phongsaphak Sittimart, Kazuki Aramaki, Takeru Hamasaki, Tsuyoshi Yoshitake, Nathaporn Promros, Physical Properties of Fe₃Si Films Coated through Facing Targets Sputtering after Microwave Plasma Treatment, Coatings 11 (2021) Article No. 923. (Impact factor 2.436) Indexed in Web of science.
- [2] **Rawiwan Chaleawpong**, Nathaporn Promros, Peerasil Charoenyuenyao, Phongsaphak Sittimart, Pattarapol Sittisart, Nattakorn Borwornpornmetee, Yuki Tanaka, Tsuyoshi Yoshitake, Photovoltaic, Capacitance-Voltage, Conductance-Voltage, and Electrical Impedance Characteristics of p-Type Silicon/Intrinsic-Silicon/n-Type Semiconducting Iron Disilicide Heterostructures Built via Facing Target Direct-Current Sputtering, Thin Solid Films, Vol. 709 (2020) Article No. 138229. (Impact factor 1.748) Indexed in Web of science.
- [3] **Rawiwan Chaleawpong**, Nathaporn Promros, Abdelrahman Zkria, Peerasil Charoenyuenyao, Eslam Abubakr, Tsuyoshi Yoshitake, Diode parameters and ultraviolet light detection characteristics of n-type silicon/p-type nanocrystalline diamond heterojunctions at different temperatures, Thin Solid Films, Vol. 709 (2020) Article No. 138222. (Impact factor 1.748) Indexed in Web of science.
- [4] Peerasil Charoenyuenyao, Nathaporn Promros, **Rawiwan Chaleawpong**, Nattakorn Borwornpornmetee, Pattarapol Sittisart, Yuki Tanaka, Tsuyoshi Yoshitake, Wettability, Morphological and Wetting Properties of Semiconducting Beta and Nanocrystalline Iron Disilicide Formed via Radio Frequency Magnetron Sputtering, Thin Solid Films, Vol. 709 (2020) Article No. 138248. (Impact factor 1.748) Indexed in Web of science.
- [5] **Rawiwan Chaleawpong**, Nathaporn Promros, Peerasil Charoenyuenyao,

The material is reserved for educational use only, not allowed for commercial use.

Forbidden to modify the content, and cite the document when use.

- Phongsaphak Sittimart, Satoshi Takeichi, Yuki Katamune, Abdelrahman Zkria, Eslam Abubakr, Mohamed Egiza, Ali M. Ali, and Tsuyoshi Yoshitake, Diode Parameters and Equivalent Electrical Circuit Model of n-Type Silicon/B-Doped p-Type Ultrananocrystalline Diamond Heterojunctions Manufactured Through Coaxial Arc Plasma Deposition, *Journal of Nanoscience and Nanotechnology*, Vol. 20 (2020) 4884-4891. (Impact factor 1.483) Indexed in Web of science.
- [6] Peerasil Charoenyuenyao, Nathaporn Promros, **Rawiwan Chaleawpong**, Pitoon Noymaliwan, Nattakorn Borwornpornmetee, Surachart Kamoldilok, Supanit Porntheeraphat, Bunpot Saekow, Tanapoj Chaikereee, Benjarong Samransuksamer, Peerapong Nuchuay, Chanunthorn Chananonnawathorn, Saksorn Limwichean, Mati Horprathum, Pitak Eiamchai, Viyapol Patthanasettakul, Influence of an Annealing Temperature in a Vacuum Atmosphere on the Physical Properties of Indium-Tin Oxide Nanorod Films, *Journal of Nanoscience and Nanotechnology*, Vol. 20 (2020) 5006-5013. (Impact factor 1.483) Indexed in Web of science.
- [7] Pattarapol Sittisart, Nathaporn Promros, **Rawiwan Chaleawpong**, Peerasil Charoenyuenyao, Nattakorn Borwornpornmetee, Yuki Tanaka, Tsuyoshi Yoshitake, Light Detection and Carrier Transportation Mechanism in p-Type Si/n-Type Nanocrystalline FeSi₂ Heterojunctions produced via Radio-Frequency Magnetron Sputtering, *Journal of Nanoscience and Nanotechnology*, Vol. 20 (2020) 5082-5088. (Impact factor 1.483) Indexed in Web of science.
- [8] Peerasil Charoenyuenyao, Nathaporn Promros, **Rawiwan Chaleawpong**, Nattakorn Borwornpornmetee, Pattarapol Sittisart, Yuki Tanaka, Tsuyoshi Yoshitake, Wettability, Surface Morphology and Structural Properties of β -FeSi₂ Films Manufactured through Usage of Radio-Frequency Magnetron Sputtering, *Journal of Nanoscience and Nanotechnology*, Vol. 20 (2020) 5075-5081. (Impact factor 1.483) Indexed in Web of science.
- [9] **Rawiwan Chaleawpong**, Nathaporn Promros, Peerasil Charoenyuenyao, Kenji Hanada, Li Chen, and Tsuyoshi Yoshitake, Extraction of *I-V*, *G-V-f* and *C-V-f* Characteristics for p-Type Silicon/Intrinsic Ultrananocrystalline Diamond/n-Type Nanocrystalline Iron Disilicide Heterojunction Photodiodes, *Journal of Nanoscience and Nanotechnology*, Vol. 20 (2020) 441-433 (Impact factor 1.483) Indexed in Web of science.
- [10] **Rawiwan Chaleawpong**, Nathaporn Promros, Peerasil Charoenyuenyao, Takanori Hanada, Shinya Ohmagari, and Tsuyoshi Yoshitake, Temperature Dependence of Alternating Current Impedance in n-Type Si/B-doped p-Type Ultrananocrystalline Diamond Heterojunctions produced through Pulsed Laser Deposition, *Journal of Nanoscience and Nanotechnology*, Vol. 20 (2020) 331-331

- .337(Impact factor 1.483) Indexed in Web of science.
- [11] Peerasil Charoenyuenyao, Nathaporn Promros, **Rawiwan Chaleawpong**, Bunpot Saekow, Supanit Porntheeraphat, and Tsuyoshi Yoshitake, Influence of Annealing Temperature on Mechanical and Wetting Properties of β -FeSi₂ Films Built Using Facing-Targets Direct-Current Sputtering, Journal of Nanoscience and Nanotechnology, Vol. .628-621 (2020) 20(Impact factor 1.483) Indexed in Web of science.
- [12] **Rawiwan Chaleawpong**, Nathaporn Promros, Peerasil Charoenyuenyao, Adison Nopparuchikun, Takanori Hanada, Shinya Ohmagari, and Tsuyoshi Yoshitake, *C-V-f*, *G-V-f* and *Z''-Z'* Characteristics of n-Type Si/B-Doped p-Type Ultrananocrystalline Diamond Heterojunctions Formed via Pulsed Laser Deposition, Journal of Nanoscience and Nanotechnology, Vol. -6812 (2019) 19 .6820 (Impact factor 1.483) Indexed in Web of science.
- [13] Peerasil Charoenyuenyao, Nathaporn Promros, **Rawiwan Chaleawpong**, Bunpot Saekow, Supanit Porntheeraphat, and Tsuyoshi Yoshitake, Effect of Annealing on Surface Morphology and Wettability of NC-FeSi₂ Films Produced via Facing-Target Direct-Current Sputtering, Journal of Nanoscience and Nanotechnology, Vol. .6840-6834 (2019) 19(Impact factor 1.483) Indexed in Web of science.
- [14] Nathaporn Promros, Pitoon Noymaliwan, Peerasil Charoenyuenyao, **Rawiwan Chaleawpong**, Supanit Porntheeraphat, Bunpot Saekow, Tanapoj Chaikereee, Benjarong Samransuksamer, Peerapong Nuchuay, Chanunthorn Chananonnawathorn, Saksorn Limwichean, Mati Horprathum, Pitak Eiamchai, and Viyapol Patthanasettakul, Study of Annealing Influence on Basic Properties of Indium Tin Oxide Nanorod Films Deposited Using Glancing Angle Ion-Assisted Electron Beam Evaporation, Journal of Nanoscience and Nanotechnology, Vol. 19 (2019) 1432-1438. (Impact factor 1.483) Indexed in Web of science.
- [15] **Rawiwan Chaleawpong**, Nathaporn Promros, Peerasil Charoenyuenyao, Takanori Hanada, Shinya Ohmagari, Abdelrahman Zkria, and Tsuyoshi Yoshitake, Junction parameters of boron-doped p-type ultrananocrystalline diamond/hydrogenated amorphous carbon composite/n-type silicon heterojunctions formed by pulsed laser deposition, Journal of Nanoscience and Nanotechnology, Journal of Nanoscience and Nanotechnology, Vol. 19 (2019) 1567-1573. (Impact factor 1.483) Indexed in Web of science.
- [16] Weerasaruth Kaenrai, Nathaporn Promros, Phongsaphak Sittimart, **Rawiwan Chaleawpong**, Peerasil Charoenyuenyao, Thanachai Changcharoen, Adison Nopparuchikun, Tomohiro Nogami, and Tsuyoshi Yoshitake, Photovoltaic Properties and Series Resistance of p-Type Si/Intrinsic Si/n-Type Nanocrystalline FeSi₂ Heterojunctions Created by Utilizing Facing-Targets Direct-Current

- Sputtering, Journal of Nanoscience and Nanotechnology, Journal of Nanoscience and Nanotechnology, Vol. 19 (2019) 1445-1450. (Impact factor 1.483) Indexed in Web of science.
- [17] **Rawiwan Chaleawpong**, Nathaporn Promros, Peerasil Charoenyuenyao, Adison Nopparuchikun, Phongsaphak Sittimart, Tomohiro Nogami, and Tsuyoshi Yoshitake, Production of p-Type Si/n-Type β -FeSi₂ Heterojunctions Using Facing-Targets Direct-Current Sputtering and Evaluation of Their Resistance and Interface State Density, Phys. Status Solidi A, Vol. 215 (2018) Article No. .1701022 (Impact factor 1.795) Indexed in Web of science.
- [18] Peerasil Charoenyuenyao, Nathaporn Promros, **Rawiwan Chaleawpong**, and Tsuyoshi Yoshitake, Surface Morphology and Wettability for Thin Films of Beta-Iron Disilicide Produced through Direct-Current Sputtering Utilizing a Pair of Facing Targets, MATEC Web of Conferences Vol. 192, (.01054 (2018) Indexed in SCOPUS.
- [19] Nathaporn Promros, Pitoon Noymaliwan, Peerasil Charoenyuenyao, **Rawiwan Chaleawpong**, Supanit Porntheeraphat, Bunpot Saekow, Tanapoj Chaikereee, Benjarong Samransuksamer, Peerapong Nuchuay, Chanunthorn Chananonnawathorn, Saksorn Limwichean, Mati Horprathum, Pitak Eiamchai, and Viyapol Patthanasettakul, Impact of Annealing Temperature on the Physical Properties of Indium Tin Oxide Nanorod Films Grown by Glancing-Angle Ion-Assisted Electron-Beam Evaporation, (1st MRS Thailand International Conference, (2017) 382-387.